Dissertation
submitted to the
Combined Faculties for the Natural Sciences and for Mathematics
of the Ruperto–Carola University of Heidelberg, Germany
for the degree of
Doctor of Natural Sciences

presented by

Diplom–Physiker Timo Paulus
born in Rockenhausen

Oral examination: 16th December, 2002

Soft diffractive high energy scattering and form factors in nonperturbative QCD

Referees: Prof. Dr. Otto Nachtmann
Prof. Dr. Karlheinz Meier

Weiche diffraktive Hochenergiestreuung und Formfaktoren in nichtperturbativer QCD

Zusammenfassung

In der vorliegenden Arbeit untersuchen wir weiche Hochenergie-Reaktionen im Rahmen nichtperturbativer Modelle. Dazu verwenden wir ein auf einem Funktionalintegral-Ansatz beruhendes Modell und leiten die Streuamplituden her, deren wesentlicher Bestandteil Erwartungswerte von lichtartigen Wegner-Wilson Schleifen und Linien sind, die dann im Modell des stochastischen Vakuums berechnet werden. Mesonen beschreiben wir in einem einfachen Quark-Antiquark Bild, für Baryonen nehmen wir eine Quark-Diquark Struktur an, als Hadron-Wellenfunktionen verwenden wir einen Wirbel-Stech-Bauer Ansatz. Aus den Streuamplituden berechnen wir integrierte und differentielle Wirkungsquerschnitte sowohl für elastische und diffraktive Proton-Proton als auch für Proton-Pion Streuung bei hohen Schwerpunktsenergien und kleinen Impulsüberträgen und vergleichen mit experimentellen Daten. Abhängig von der Symmetrie des jeweiligen Endzustandes erhalten wir entweder $C = P = +1$ (Pomeron) oder $C = P = -1$ (Odderon) Austausch. Des weiteren berechnen wir im Rahmen des Modells die Isovektor-Formfaktoren des Protons und des Pions bei raumartigen Impulsüberträgen. Im abschliessenden Kapitel verwenden wir einen Dispersionsrelations-Ansatz zur Berechnung des Pion Formfaktors bei zeitartigen Impulsüberträgen. Aus dem Vergleich mit experimentellen Daten bestimmen wir die Massen und Kopplungskonstanten der ρ- und ω-Mesonen.

Soft diffractive high energy scattering and form factors in nonperturbative QCD

Abstract

In this work we study soft high energy reactions in the framework of nonperturbative models. Using a functional integral approach we derive the scattering amplitudes, which are governed by expectation values of light-like Wegner-Wilson loops and lines, which then are then evaluated in the model of the stochastic vacuum. We describe mesons in a simple quark-antiquark picture, for baryons we assume a quark-diquark structure, as hadronic wave functions we apply a Wirbel-Stech-Bauer ansatz. In the following we calculate integrated and differential cross sections from the scattering amplitudes, as well for elastic and diffractive proton-proton as for proton-pion scattering at high centre of mass energies and small momentum transfers and compare to experimental data. Depending on the symmetry of the respective final state we get either $C = P = +1$ (pomeron) oder $C = P = -1$ (odderon) exchange. Furthermore we calculate the isovector form factors of the proton and the pion at space-like momentum transfers. In the final chapter we use a dispersion approach to calculate the pion form factor at time-like momentum transfers and determine the masses and coupling constants of the ρ- and ω-mesons from a comparison to experimental data.

Contents

1 Introduction **1**

2 Derivation of the scattering amplitudes **5**
2.1 Quark-quark scattering 6
2.1.1 The functional integral approach 6
2.1.2 The eikonal expansion 9
2.2 Description of antiquarks 11
2.3 Scattering of hadrons 13
2.3.1 Exclusive scattering 14
2.3.2 Semi-inclusive scattering 16

3 Evaluation of the scattering amplitudes **19**
3.1 The loop-loop correlation function in the MSV 19
3.1.1 Properties of the MSV 20
3.1.2 Application of the MSV to the correlation function 22
3.2 The hadronic wave functions 24
3.3 The hadronic scattering amplitudes 26
3.3.1 Elastic scattering 27
3.3.2 Single diffractive dissociation 28
3.3.3 Double diffractive excitation 29

4 Hadron-hadron cross sections **33**
4.1 Proton-proton scattering 35
4.1.1 Elastic scattering 35
4.1.2 Single diffractive dissociation 37
4.1.3 Double diffractive excitation 45
4.2 Proton-pion scattering 48
4.2.1 Elastic scattering 49
4.2.2 Single diffractive dissociation 50

5 Space-like form factors in the model **51**
5.1 The electromagnetic form factors of the proton 51
5.2 The electromagnetic form factor of the pion 54

6 The time-like pion form factor in a dispersion approach **57**
6.1 The dispersion approach 60
6.2 The $\rho - \omega$ mixing 64
6.3 The electromagnetic pion form factor with $\rho - \omega$ mixing 66
6.4 Numerical analysis 67
6.4.1 The electromagnetic pion form factor 67
6.4.2 The charged current pion form factor 70

7 Conclusions **73**

A Conventions **77**

B Connectors **79**

C Calculation of form factors in the model **81**

Bibliography **85**

List of Figures

2.1 Two light-like Wegner-Wilson loops in position space 15
2.2 The orientation and extension of the light-like Wegner-Wilson loops in a projection into transverse position space 16
2.3 The semi-inclusive scattering reaction $h_1 + h_2 \to h_1 + X$ 17

3.1 The integration surfaces for the evaluation of the loop-loop correlation function 23

4.1 The differential cross section for elastic pp-scattering 36
4.2 The integrated cross section for elastic pp-scattering as a function of $\sqrt{s}$ 37
4.3 The integrated cross section for single diffractive pp-scattering as a function of $\sqrt{s}$ 38
4.4 The differential cross section for single diffractive pp-scattering 40
4.5 The contributions of oscillator wave functions with fixed quantum numbers to the differential cross section for single diffractive pp-scattering 42
4.6 The mass spectrum for single diffractive pp-scattering 44
4.7 The differential cross section for double diffractive pp-scattering . . . 46
4.8 The contribution of $\mathcal{T}_+$ and $\mathcal{T}_-$ to the differential cross section for double diffractive pp-scattering 47
4.9 The differential cross section for elastic $p\pi$-scattering 49

5.1 The space-like isovector form factor of the proton 53
5.2 The space-like pion form factor 54

6.1 The contributions to the time-like pion form factor 61
6.2 The contributions to the $\rho - \omega$ mixing amplitude 65
6.3 The contributions to the pion form factor at first order of $g_{\omega\to\pi\pi}$ . . . 67
6.4 The phase and the modulus of the electromagnetic pion form factor . 69
6.5 The charged current pion form factor 70
6.6 Comparison of the electromagnetic and the charged current pion form factor 71

C.1 The two contributions to the matrix element of the isospin current . . 82

List of Tables

4.1 The parameters of the MSV for the matrix cumulant and the expansion method 33
4.2 The ratio of the single diffractive dissociation to the sum of the single diffractive dissociation and elastic cross sections 39

6.1 The masses, rates and decay constants for vector mesons from [11] . . 66
6.2 The ρ^0 parameters from a fit to the phase of the form factor 68
6.3 The ρ^0 and ω parameters from a fit to the modulus of the form factor 68
6.4 The ρ^- parameters from a fit to the charged current pion form factor 70
6.5 The masses and decay constants of the vector mesons and the mixing parameter as obtained by our analysis 71

Chapter 1

Introduction

Today it is common belief that Quantum Chromodynamics (QCD) is the theory describing the physics of the strong interaction. QCD is a Yang-Mills theory [1] with the gauge group SU(3). The Lagrangian of QCD is constructed from the basic degrees of freedom, the quarks and gluons, in terms of which we should be able to describe all strong processes. Due to the non-abelian structure of SU(3), both quarks and gluons carry colour-charge. But in the real world we observe neither quarks nor gluons as free particles. Instead, the particles we see in nature are hadrons, which are colourless objects, in which the quarks and gluons are confined. The problem now is to find a suitable transition from the level of quarks and gluons, whose transactions are described by the QCD Lagrangian, to the level of hadrons, which are seen in the real world processes. For certain circumstances we can solve this problem and derive results from first principles, starting from the Lagrangian.

One case where this is possible is the field of short-distance phenomena. There, all occurring momentum scales are much larger than the QCD scale parameter $\Lambda_{\mathrm{QCD}} \approx 200\,\mathrm{MeV}$. Due to asymptotic freedom [2], the QCD coupling parameter becomes small for large momentum scales and therefore we can use perturbative methods, which allow us for example to calculate the total cross section in electron-positron annihilation or the total hadronic decay rate of the Z-boson. Another example is the calculation of parton distribution functions for large Q^2 by means of the DGLAP equation [3], which has been derived from perturbative QCD.

For long-distance phenomena, i.e. when all occurring momentum scales are only of order Λ_{QCD} or smaller, the QCD coupling becomes too large and perturbation theory breaks down. This is the regime of nonperturbative QCD, where we have to use numerical methods to obtain results from first principles. One such numerical method is lattice QCD [4, 5]. Typical quantities that are calculated in this context are e.g. hadron masses.

The subject of this work are soft high energy reactions, which are neither pure short-distance, nor pure long-distance phenomena, because we deal with two momentum scales: the centre of mass (c.m.) energy is becoming large, $\sqrt{s} \gtrsim 10\,\mathrm{GeV}$, the momentum transfer stays finite, $\sqrt{|t|} \lesssim 1\,\mathrm{GeV}$. Therefore, neither perturbation

theory nor numerical methods such as lattice QCD can be applied directly and we have to revert to models.

Until today, of course a lot of models have been developed to describe high energy hadron-hadron scattering. Examples are the geometric model [6], the valon model [7], topological expansions and strings [8], perturbative field theoretical calculations [9] and the work of Cheng and Wu on the behaviour of high energy scattering amplitudes in quantum field theory based on perturbative calculations (see [10] and references therein).

The experimentally observed increase of total cross sections for hadronic reactions with the c.m. energy [11], starting at about $\sqrt{s} = 10$ GeV, has been described phenomenologically by Donnachie and Landshoff [12] in the context of Regge theory [13]. In this picture the pomeron behaves like a photon with $C = +1$ and couples to single quarks, the transition to the hadron level then leads to the additive quark rule [14]. The rise of the total hadronic cross sections can be described by a pomeron with an intercept slightly larger than one [11,12]. For inelastic diffraction, the pomeron-photon analogy was applied in [15] to relate the cross section of these reactions in a quantitative way to the structure functions of deep inelastic electron-proton scattering. For reviews on nonperturbative models we refer to [16–19].

A new nonperturbative description of soft hadronic high energy reactions, starting from a microscopic level, was developed in [20] where in the case of an abelian gluon model the pomeron properties were related to nonperturbative aspects of the vacuum like the gluon condensate introduced by Shifman, Vainshtein and Zakharov [21]. These methods were generalised to QCD in [22]. In this model the objects governing the scattering amplitudes are correlation functions of Wegner-Wilson lines and loops [23,24], which are then evaluated in the model of the stochastic vacuum [25] as formulated in Minkowski space in [23,24,26].

This method has been applied to various reactions, for example exclusive vector meson production [27–29], elastic hadron-hadron scattering [30], and photo- and electroproduction of pseudoscalar and tensor mesons [31,32]. In this work we will extend the model to the description of inelastic diffractive hadron-hadron scattering.

In chapter 2 we present the basic principles of our model. Progressing as in [22–24,26–30,33,34] we start from quark-quark scattering, where we apply a functional integral approach and use an eikonal expansion to derive an expression for the quark-quark scattering amplitudes at high energies and small momentum transfers. The transition to the hadron level is performed by folding with suitably defined wave functions. In this work, the constituent configuration of baryons is assumed to be of the quark-diquark type for the reasons given in [35,36]. Then baryons act as colour dipoles like mesons. Moreover we use two different models for the diffractive final state X when describing inelastic diffractive scattering processes. The soft high energy hadron-hadron scattering amplitudes for both elastic and inelastic diffractive scattering are given at the end of this chapter.

The evaluation of the scattering amplitudes is the topic of the next chapter. We first give a brief summery of the properties of the model of the stochastic vacuum and

then apply it in its Minkowskian formulation to calculate the correlation functions of the light-like Wegner-Wilson loops, where we use two approaches. Then we discuss the hadronic wave functions [37] for s- and p-wave states. Furthermore we define wave functions incorporating the eigenfunctions of a two-dimensional harmonic oscillator which we need for one of the methods describing the diffractive final state in inelastic diffractive scattering. Finally, we analyse symmetry properties of the scattering amplitudes after inserting the wave functions and the expressions which we obtain from the evaluation of the loop-loop correlation functions in the different approaches. Based on symmetry considerations we find that our model gives either $C = P = +1$, i.e. pomeron, exchange, or $C = P = -1$, i.e. odderon, exchange, depending on which reaction in particular we are studying. To be able to study odderon exchange in the framework of our model in a purely hadronic reaction, we have chosen a specific reaction which should have a clear experimental signature.

In chapter 4 we calculate integrated and differential cross sections from the scattering amplitudes derived in chapters 2 and 3. We concentrate on proton-proton and proton-pion scattering and compare our numerical results obtained from both approaches to experimental data. In the case of pp-scattering we briefly review previous results on the differential elastic cross section from [30]. We then turn to single diffractive dissociation $pp \to pX$. Most of the results shown in this context are the basis for the publication [38], where in addition to hadron-hadron scattering also photo- and electroproduction of ρ^0-mesons is discussed. Furthermore we study the double diffractive excitation of the proton $pp \to N(1535)N(1535)$ which is mediated by odderon exchange and give our predictions for the differential and integrated cross section for this reaction. For proton-pion scattering we also start with a review of the differential elastic cross section from [30] and then continue with the study of single diffractive dissociation of the pion $p\pi \to pX$.

The next chapter deals with the isovector proton and pion form factors at small space-like momentum transfers. In the region of interest to us here, $0 \leq -q^2 \leq 10\,\mathrm{GeV}^2$, the form factor is dominated by nonperturbative QCD effects [39], and can for example be described by a picture based on the concept of constituent quarks which effectively account for nonperturbative dynamics [40]. In this region all preconditions for the application of our nonperturbative model are fulfilled. Therefore we can calculate the proton and pion form factors in the framework of our model and extract the electromagnetic radii from fits to experimental data. However, we do not intend to perform a precision calculation of the form factors but apply the calculation mainly to extract parameters we need in the definition of our hadron wave functions. The results obtained here are also published in [38].

The aim of chapter 6 is to study the pion form factor for small time-like momentum transfers. In this region we can no longer apply the nonperturbative model which we have used so far. There are many approaches to describe the time-like pion form factor, including vector meson dominance [41], chiral perturbation theory [42] and the application of dispersion relations [43]. In the following we apply consistently a dispersion approach with $\rho\pi\pi$, ρKK, and gauge-invariant $\rho\gamma$ couplings.

The form factor is obtained by resummation of pion and kaon loops. For the loop diagrams we use a dispersion representation and analyse ambiguities related to subtraction constants. The resulting representation for the form factor is shown to have the form of the conventional vector meson dominance formula with one important distinction - the effective ρ-meson decay constant $f_\rho^{\rm eff}$ turns out to depend on the momentum transfer. For the electromagnetic pion form factor we include in addition the $\rho-\omega$ mixing effects. We apply the representations obtained to the analysis of the data on the pion form factors from e^+e^- annihilation and τ decay and extract the ρ^-, ρ^0 and ω masses and coupling constants. The work of this chapter has been published in [44].

Our conclusions and a summary are given in chapter 7.

Chapter 2

Derivation of the scattering amplitudes

The formalism we are going to use, as developed in [22], is based on the following general considerations. Imagine that we look at e.g. elastic hadron-hadron scattering

$$h_1(P_1) + h_2(P_2) \to h_1(P_3) + h_2(P_4) \tag{2.1}$$

at high energies and small momentum transfer through a "microscope". This microscope has to have an appropriate resolution, which allows us to see the essential features of the process but does not resolve the unimportant details of the internal structure of the hadrons, which would only complicate the description. In [22] the appropriate resolution has been estimated by a series of simple arguments based on the uncertainty relation. For a time interval of approximately $\tau_0 \approx 2\,\mathrm{fm}$ the following assumptions concerning the scattering process can be made:

- The parton state of the hadrons does not change qualitatively, i.e. parton annihilation and parton production processes are negligible.
- The partons are subject to soft elastic scattering.
- The partons move on essentially straight light-like worldlines.

To derive the scattering amplitudes for soft high energy hadron-hadron scattering, we progress as follows: first, we consider quark-quark scattering in the framework of the model. On this level, the essential features of the model will become apparent and we will see that the strong interaction between the quarks is mediated by the nonperturbative gluonic vacuum fluctuations. Then we discuss how to treat antiquarks in our formalism and give simple rules for the construction of scattering amplitudes for arbitrary systems of quarks and antiquarks in the framework of our model. With these ingredients we can progress to the level of hadrons, which we perform by folding the partonic scattering amplitudes by suitable hadronic wave functions. In the last step we construct the hadronic $\mathcal{T}$-matrix elements for the types of reactions we are interested in.

2.1 Quark-quark scattering

Consider the scattering of two quarks q_1 and q_2

$$q_1(p_1) + q_2(p_2) \to q_3(p_3) + q_4(p_4), \tag{2.2}$$

where p_i, $i = 1 \ldots 4$ are the four-momenta of the quarks and the momentum transfer is $q = p_1 - p_3$. The normalisation of the quark states is given by

$$\begin{aligned} &\langle q(p_j, s_j, A_j, f_j)|q(p_k, s_k, A_k, f_k)\rangle \\ &\qquad = \delta_{s_j,s_k}\delta_{A_j,A_k}\delta_{f_j,f_k}(2\pi)^2\sqrt{2p_j^0 2p_k^0}\,\delta^{(3)}(\mathbf{p}_j - \mathbf{p}_k) \\ &\qquad \equiv \delta(j,k). \end{aligned} \tag{2.3}$$

As an abbreviation we use $j(k)$ to denote the momentum $p_{j(k)}$ and the set of spin, colour and flavour index $s_{j(k)}$, $A_{j(k)}$ and $f_{j(k)}$ of the quark $q_{j(k)}$, respectively.

2.1.1 The functional integral approach

Applying the reduction formalism by Lehmann, Symanzik and Zimmermann to the $\mathcal{S}$-matrix element of reaction (2.2), we get an integral over the 4-point function of the quark fields

$$\begin{aligned} \mathcal{S}_{fi} &\equiv \langle q_3(p_3)q_4(p_4)|\mathcal{S}|q_1(p_1)q_2(p_2)\rangle \\ &= Z_\psi^{-2}\int \mathrm{d}^4x_1\mathrm{d}^4x_2\mathrm{d}^4x_3\mathrm{d}^4x_4\, e^{-i(p_1\cdot x_1 + p_2\cdot p_2 - p_3\cdot x_3 - p_4\cdot x_4)} \\ &\qquad \bar{u}_4(i\overrightarrow{\not\partial}_4 - m'_{q_4})\bar{u}_3(i\overrightarrow{\not\partial}_3 - m'_{q_3}) \\ &\qquad \langle 0|\mathrm{T}(q_4(x_4)q_3(x_3)\bar{q}_1(x_1)\bar{q}_2(x_2))|0\rangle \\ &\qquad (i\overleftarrow{\not\partial}_1 + m'_{q_1})u_1(i\overleftarrow{\not\partial}_2 + m'_{q_2})u_2. \end{aligned} \tag{2.4}$$

Here Z_ψ is the wave function renormalisation constant and m'_{q_j} are the renormalised quark masses, defined by the location of the pole of Fourier transform of the full Feynman propagator. The 4-point function can be calculated nonperturbatively using the functional integral of QCD

$$\begin{aligned} &\langle 0|\mathrm{T}(q_4(x_4)q_3(x_3)\bar{q}_1(x_1)\bar{q}_2(x_2))|0\rangle \\ &\quad = \mathcal{Z}^{-1}\int \mathcal{D}(G,q,\bar{q})\exp\left\{i\int \mathrm{d}x\,\mathcal{L}_{QCD}(x)\right\} q_4(x_4)q_3(x_3)\bar{q}_1(x_1)\bar{q}_2(x_2) \end{aligned} \tag{2.5}$$

with the partition function

$$\mathcal{Z} = \langle 0_{\mathrm{out}}|0_{\mathrm{in}}\rangle = \int \mathcal{D}(G,q,\bar{q})\exp\left\{i\int \mathrm{d}x\,\mathcal{L}_{QCD}(x)\right\}. \tag{2.6}$$

The QCD Lagrangian is given by

$$\mathcal{L}_{QCD} = -\frac{1}{2}\mathrm{Tr}(G_{\mu\nu}(x)G^{\mu\nu}(x)) + \sum_q \bar{q}(x)(i\not{D} - m_q)q(x). \tag{2.7}$$

Here $q(x)$ are the quark fields with masses m_q, $q = u, d, s, c, b, t$ counting the different quark flavours. In standard notation $G_\mu(x)$ denotes the matrix of the gluon potential, $G_{\mu\nu}(x)$ the matrix of the gluon field strength tensor.

$$\begin{aligned} G_\mu(x) &= G^a_\mu(x)\frac{\lambda_a}{2}, \\ G_{\mu\nu}(x) &= \partial_\mu G_\nu(x) - \partial_\nu G_\mu(x) + ig[G_\mu(x), G_\nu(x)] \end{aligned} \tag{2.8}$$

$\lambda_{a,\, a=1,\ldots,8}$ are the Gell-Mann matrices of SU(3) with colour index a, D_μ is the covariant derivative, defined by

$$D_\mu = \partial_\mu + igG_\mu. \tag{2.9}$$

As the Lagrangian is bilinear in the quark and antiquark fields we can directly perform the integration over the fermionic degrees of freedom by a generalised Gaussian integration and find

$$\begin{aligned} &\langle 0|\mathrm{T}(q_4(x_4)q_3(x_3)\bar{q}_1(x_1)\bar{q}_2(x_2))|0\rangle \\ &\quad = \mathcal{Z}^{-1}\int \mathcal{D}(G)\exp\left\{-\frac{i}{2}\int \mathrm{d}x\,\mathrm{Tr}(G_{\mu\nu}(x)G^{\mu\nu}(x))\right\} \\ &\qquad \prod_q \det\left[-i(i\not{D} - m_q + i\epsilon)\right] \\ &\qquad \left\{\delta_{f_3 f_1}\frac{1}{i}S_F(x_3, x_1; G)\delta_{f_4 f_2}\frac{1}{i}S_F(x_4, x_2; G) - (3 \leftrightarrow 4)\right\}. \end{aligned} \tag{2.10}$$

$S_F(x_j, x_k; G)$ is the unrenormalised Green's function for a quark in an external gluon field $G_\mu(x)$ for which we have

$$(i\not{D} - m_q)S_F(x_j, x_k; G) = -\delta^{(4)}(x_j - x_k). \tag{2.11}$$

The Lippmann-Schwinger equation

$$S_F(x_j, x_k; G) = S^0_F(x_j, x_k) - S^0_F(x_j, x_k)(g\not{G} - \delta m)S_F(x_j, x_k; G) \tag{2.12}$$

relates the unrenormalised Green's function to the free Green's function $S^0_F(x_j, x_k)$ with renormalised mass $m' = m + \delta m$. Using the shorthand notation

$$\begin{aligned} |j) &:= u_{s_j, A_j}(p_j)e^{-ip_j\cdot x_j}, \\ (j| &:= \bar{u}_{s_j, A_j}(p_j)e^{ip_j\cdot x_j}, \\ |\psi^F_{p_j}) &:= S_F(i\overleftarrow{\not{\partial}}_j + m'_{q_j})|j), \end{aligned} \tag{2.13}$$

where $|\psi^F_{p_j})$ are quark wave functions which satisfy the Dirac equation in an external gluon potential

$$(i\not{D}-m_{q_j})|\psi^F_{p_j}) = 0, \quad j = 1, 2, \tag{2.14}$$

and the Lippmann-Schwinger equation, we get from (2.4)

$$\mathcal{S}_{fi} = -Z_\psi^{-2}\Big\langle \delta_{f_3 f_1}\delta_{f_4 f_2}(3|(g\not{G}-\delta m_{q_1})|\psi^F_{p_1})(4|(g\not{G}-\delta m_{q_2})|\psi^F_{p_2}) - (3 \leftrightarrow 4)\Big\rangle_G. \tag{2.15}$$

In our notation we implicitly include the integrations over x_j, x_k, resulting from the LSZ reduction formalism, when we write expressions of the form $(k|\psi^F_{p_j})$. To clear up the notation further we have introduced the bracket symbol $\langle\,\rangle_G$ of a function $F(G)$ as

$$\begin{aligned}\langle F(G)\rangle_G \;&:=\; \mathcal{Z}^{-1}\int \mathcal{D}(G)\exp\left\{-\frac{i}{2}\int \mathrm{d}x\,\mathrm{Tr}(G_{\mu\nu}(x)G^{\mu\nu}(x))\right\}\\ &\qquad \prod_q \det\left[-i(i\not{D}-m_q+i\epsilon)\right]F(G).\end{aligned} \tag{2.16}$$

In (2.15) we have two contributions, the one that is written out explicitely corresponds to t-channel exchange, the one that we have written symbolically as $(3 \leftrightarrow 4)$, meaning that quark 3 has to be interchanged with quark 4, corresponds to an u-channel process. In high energy scattering with $\sqrt{s} \to \infty$ and small $\sqrt{-t}$ the u-channel contributions are suppressed by a factor s^{-1} at least and we therefore will neglect them in the following. With the definition of quark scattering amplitudes

$$\begin{aligned}\mathcal{M}^F_{kj}(G) \;&:=\; (k|(i\overrightarrow{\not{\partial}}_k - m'_{q_k})S_F(i\overleftarrow{\not{\partial}}_j + m'_{q_k})|j)\\ &=\; (k|(g\not{G}-\delta m_{q_j})|\psi^F_{p_j}), \quad (j=1,\,k=3), \quad (j=2,\,k=4),\end{aligned} \tag{2.17}$$

which have the correct form for a scattering amplitude, i.e. an incoming complete wave folded with the potential and an outgoing plane wave, we get from (2.15)

$$\mathcal{S}_{fi} = -Z_\psi^{-2}\,\delta_{f_3 f_1}\delta_{f_4 f_2}\langle \mathcal{M}^F_{31}(G)\mathcal{M}^F_{42}(G)\rangle_G. \tag{2.18}$$

This equation can be interpreted as follows: the incoming quarks are scattered independently on the gluon background fields. This is described by the quark scattering amplitudes $\mathcal{M}^F_{31}$, $\mathcal{M}^F_{42}$ which are evaluated independently. Then we have to average over all gluon field configurations by performing the functional integration $\langle\,\rangle_G$.

The up to now undetermined wave function renormalisation constant Z_ψ appears in (2.18). However, one of the assumptions of our model is that over the time interval considered by us, no parton creation or annihilation processes occur, meaning Z_ψ should be equal to 1. In [22] Z_ψ has been calculated in the framework of the model and one consistently finds $Z_\psi = 1$. In the following we therefore set the wave function renormalisation constant to 1.

Before we continue our programme and have to find a suitable high energy approximation that will allow us to calculate the quark scattering amplitudes $\mathcal{M}^F_{kj}(G)$, we note that the wave functions $|\psi^F_{p_j})$ do not satisfy the desired boundary conditions for $x^0 \to \pm\infty$. The transition from Feynman wave functions $|\psi^F_{p_j})$ to retarded wave functions $|\psi^r_{p_j})$ can be performed using the Lippmann-Schwinger equation (2.12). The wave functions possess the correct behaviour for $x^0 \to -\infty$, namely that of a incoming plain wave

$$|\psi^r_{p_j}) \overset{x^0 \to -\infty}{\longrightarrow} |j). \tag{2.19}$$

The replacement of $\mathcal{M}^F_{kj}$ with $\mathcal{M}^r_{kj}$ in (2.18), i.e. going from Feynman to retarded boundary conditions, is a non-trivial step. It has been shown in [22] that this replacement is valid in the high energy limit for gluon potentials G_μ with an upper bound for the frequency spectrum. This is in consistency with our model, where we assumed that the partons undergo soft, elastic scattering. Therefore the functional integral in (2.18) is dominated by gluons with a frequency that is sufficiently small and we can write

$$\mathcal{S}_{fi} = -\delta_{f_3 f_1}\delta_{f_4 f_2}\langle \mathcal{M}^r_{31}(G)\mathcal{M}^r_{42}(G)\rangle_G, \tag{2.20}$$

with

$$\mathcal{M}^r_{kj}(G) := (k|(g\not{G} - \delta m_{q_j})|\psi^r_{p_j}). \tag{2.21}$$

2.1.2 The eikonal expansion

As mentioned before now we have to calculate the quark scattering amplitudes which involves solving the Dirac equation for a quark in an external gluon potential

$$(i\not{D} - m_{q_j})|\psi^r_{p_j}) = (i\not{\partial} - g\not{G}(x) - m'_{q_j} + \delta m_{q_j})|\psi^r_{p_j}) = 0 \tag{2.22}$$

and respecting the boundary condition (2.19), which of course cannot be done exactly. However, since we are only interested in the high energy limit of (2.4) for small momentum transfers, the DeBroglie wavelength of the quarks propagating through the gluon potentials are sufficiently small compared to the fluctuations of the gluonic configurations governing the functional integral in (2.4) and we can use an eikonal approximation. For this purpose it is convenient to use light-cone variables which are defined by

$$x_\pm = x^0 \pm x^3 \tag{2.23}$$

for any 4-vector x and to choose the centre of mass system as reference frame. In the high energy limit the quark light-cone momenta then go to infinity and the transverse momenta stay finite.

In the eikonal approximation we can now solve the differential equation (2.22) and satisfy the boundary conditions (2.19). We proceed as explained in [22, 33] and

find as solutions for the quark wave functions in leading order

$$\begin{aligned}\psi^r_{p_1}(x) &= V_-(x_+,x_-,\mathbf{x}_T)\left(1+\mathcal{O}\Big(\frac{1}{p_{1+}}\Big)\right)e^{-ip_1\cdot x}u_1(p_1),\\ \psi^r_{p_2}(x) &= V_+(x_+,x_-,\mathbf{x}_T)\left(1+\mathcal{O}\Big(\frac{1}{p_{2-}}\Big)\right)e^{-ip_2\cdot x}u_2(p_2),\end{aligned}\tag{2.24}$$

with the eikonal phases

$$\begin{aligned}V_-(x_+,x_-,\mathbf{x}_T) &= \mathrm{P}\left\{\exp\left[-\frac{ig}{2}\int_{-\infty}^{x_+}\mathrm{d}x'_+\,G_-(x'_+,x_-,\mathbf{x}_T)\right]\right\},\\ V_+(x_+,x_-,\mathbf{x}_T) &= \mathrm{P}\left\{\exp\left[-\frac{ig}{2}\int_{-\infty}^{x_-}\mathrm{d}x'_-\,G_+(x_+,x'_-,\mathbf{x}_T)\right]\right\},\end{aligned}\tag{2.25}$$

which satisfy the following boundary conditions and differential equations:

$$\begin{aligned}&V_\pm(x_+,x_-,\mathbf{x}_T)\overset{x_\mp\to-\infty}{\longrightarrow}\mathbb{1},\\ &\partial_\mp V_\pm(x_+,x_-,\mathbf{x}_T)=-\frac{ig}{2}G_\pm(x_+,x_-,\mathbf{x}_T)\cdot V_\pm(x_+,x_-,\mathbf{x}_T).\end{aligned}\tag{2.26}$$

Inserting (2.24) into (2.21) and taking into account (2.26) and the relations

$$\begin{aligned}\bar u_3(p_3)\gamma^\mu u_1(p_1) &= \sqrt{p_{3+}p_{1+}}\,\delta_{s_3s_1}n^\mu_+,\\ \bar u_4(p_4)\gamma^\mu u_2(p_2) &= \sqrt{p_{4-}p_{2-}}\,\delta_{s_4s_2}n^\mu_-,\\ n^\mu_\pm &:= \begin{pmatrix}1\\0\\0\\\pm1\end{pmatrix},\end{aligned}\tag{2.27}$$

which are valid in the high energy limit $p_{1+},p_{3+},p_{2-},p_{4-}\approx\sqrt{s}$, $p_{1-},p_{3-},p_{2+},p_{4+}\approx 0$, $\sqrt{s}\to\infty$ we find for the quark scattering amplitudes

$$\begin{aligned}\mathcal{M}^r_{31}(G) &= i\sqrt{p_{3+}p_{1+}}\delta_{s_3s_1}\int\mathrm{d}x_-\,\mathrm{d}^2x_T\,e^{\frac{i}{2}(p_3-p_1)_+x_--i(\mathbf{p}_3-\mathbf{p}_1)_T\cdot\mathbf{x}_T}\\ &\qquad[V_-(\infty,x_-,\mathbf{x}_T)-\mathbb{1}]_{A_3A_1},\\ \mathcal{M}^r_{42}(G) &= i\sqrt{p_{4-}p_{2-}}\delta_{s_4s_2}\int\mathrm{d}y_+\,\mathrm{d}^2y_T\,e^{\frac{i}{2}(p_4-p_2)_-y_+-i(\mathbf{p}_4-\mathbf{p}_2)_T\cdot\mathbf{y}_T}\\ &\qquad[V_+(y_+,\infty,\mathbf{y}_T)-\mathbb{1}]_{A_4A_2}.\end{aligned}\tag{2.28}$$

Now we insert these expressions for the quark scattering amplitudes into (2.20) and make use of the translational invariance of the functional integral. With the definition of the impact parameter $\mathbf{b}_T:=\mathbf{x}_T-\mathbf{y}_T$ we obtain our final result for the quark-quark scattering amplitude

$$\begin{aligned}\mathcal{T}_{fi} &= -2is\,\delta_{s_3s_1}\delta_{s_4s_2}\int\mathrm{d}^2b_T\,e^{i\mathbf{q}_T\cdot\mathbf{b}_T}\\ &\qquad\left\langle\Big[V_-(\infty,0,\frac{\mathbf{b}_T}{2})-\mathbb{1}\Big]_{A_3A_1}\Big[V_+(0,\infty,-\frac{\mathbf{b}_T}{2})-\mathbb{1}\Big]_{A_4A_2}\right\rangle_G.\end{aligned}\tag{2.29}$$

The momentum transfer $q = q_1 - q_3$ is purely transverse in the high energy limit.

The underlying physical picture of this result is the following: The quarks move along straight light-like lines through the external gluon potential and accumulate non-abelian phase factors $V_\pm$, which are obtained by integration along their trajectories, correlating their phases, which leads to the interaction of the quarks. To obtain the scattering amplitude we finally have to perform a Fourier transform with respect to the impact parameter $\mathbf{b}_T$. In the high energy limit the quark helicities are conserved during the interaction.

2.2 Description of antiquarks

So far we have discussed the wave functions for outgoing quarks, if we want to describe arbitrary systems of partons we need the wave functions for incoming quarks and incoming and outgoing antiquarks as well. We do not give wave functions for gluons here, since in our simple ansatz for hadrons, which we will present in the next chapter, hadrons consist of quarks and antiquarks - or diquarks in the case of baryons - only and due to one of the assumptions of our model, no parton creation (nor annihilation) occurs over the time interval of the scattering process.

$$\begin{aligned} |\psi'^r_{p_j}) &:= S_r(i\overleftarrow{\not\partial}_j + m'_{q_j})|j'), \\ (\widetilde{\psi}^a_{p_j}| &:= (j|(-i\overrightarrow{\not\partial}_j + m'_{q_j})S_r, \\ (\widetilde{\psi}'^a_{p_j}| &:= (j'|(-i\overrightarrow{\not\partial}_j + m'_{q_j})S_r. \end{aligned} \tag{2.30}$$

Here a prime denotes that we are considering an antiquark and the index a stands for advanced wave functions, which have to be used for incoming partons and fulfil the advanced boundary conditions

$$(\widetilde{\psi}^a_{p_j}| \overset{x^0 \to +\infty}{\longrightarrow} (j|. \tag{2.31}$$

The antiquark spinors are given by

$$\begin{aligned} |j') &:= v_{s_j,A_j}(p_j)e^{ip_j\cdot x_j}, \\ (j'| &:= \bar{v}_{s_j,A_j}(p_j)e^{-ip_j\cdot x_j}. \end{aligned} \tag{2.32}$$

The advanced wave functions have to satisfy the Dirac equation

$$(\widetilde{\psi}^a_{p_j}|(i\overleftarrow{\not\partial}_j + g\not{\mathcal{A}} + m'_{q_j} - \delta m_{q_j}) = 0 \tag{2.33}$$

to which we find the solutions

$$\begin{aligned} \widetilde{\psi}^a_{p_1}(x) &= \widetilde{V}_-(x_+, x_-, \mathbf{x}_T)\left(1 + \mathcal{O}\Big(\frac{1}{p_{1_+}}\Big)\right)e^{-ip_1\cdot x}u_1(p_1), \\ \widetilde{\psi}^a_{p_2}(x) &= \widetilde{V}_+(x_+, x_-, \mathbf{x}_T)\left(1 + \mathcal{O}\Big(\frac{1}{p_{2_-}}\Big)\right)e^{-ip_2\cdot x}u_2(p_2), \end{aligned} \tag{2.34}$$

with the eikonal phases defined analogously to (2.25)

$$\begin{aligned}
\widetilde{V}_-(x_+,x_-,\mathbf{x}_T) &= \overline{\mathrm{P}}\left\{\exp\left[\frac{ig}{2}\int_{x_+}^{\infty}\mathrm{d}x'_+\,G_-(x'_+,x_-,\mathbf{x}_T)\right]\right\},\\
\widetilde{V}_+(x_+,x_-,\mathbf{x}_T) &= \overline{\mathrm{P}}\left\{\exp\left[\frac{ig}{2}\int_{x_-}^{\infty}\mathrm{d}x'_-\,G_+(x_+,x'_-,\mathbf{x}_T)\right]\right\}. \qquad (2.35)
\end{aligned}$$

Here $\overline{\mathrm{P}}$ denotes anti-path-ordering. For the phase factors analogue relations to (2.26) hold

$$\begin{aligned}
\widetilde{V}_\pm(x_+,x_-,\mathbf{x}_T) &\overset{x_\mp\to\infty}{\longrightarrow} \mathbb{1}\\
\partial_\mp\left[\widetilde{V}^\dagger_\pm(x_+,x_-,\mathbf{x}_T)V_\pm(x_+,x_-,\mathbf{x}_T)\right] &= 0\\
\widetilde{V}^\dagger_\pm(x_+,x_-,\mathbf{x}_T)V_\pm(x_+,x_-,\mathbf{x}_T) &= \begin{cases} V_+(x_+,\infty,\mathbf{x}_T)\\ V_-(\infty,x_-,\mathbf{x}_T)\end{cases}. \qquad (2.36)
\end{aligned}$$

To calculate the scattering amplitude $\mathcal{M}'^{r}_{k'j'}(G)$ of an antiquark $\bar{q}$ in an external gluon potential G_μ we note that this corresponds to the scattering of a quark q in the charge conjugated gluon potential G'_μ with

$$G'_\mu(x) = CG_\mu(x)C^\dagger = -G^*_\mu(x). \qquad (2.37)$$

Furthermore we note that replacing G_μ by G'_μ in $V_\pm$ corresponds to complex conjugating the eikonal phase factor, i.e. to the replacement $V_\pm \to V^*_\pm$. Defining

$$\mathcal{M}'^{r}_{k'j'}(G) := -(j'|(i\overrightarrow{\not\partial}_j - m'_{q_j})|\psi'^{r}_{p_k}). \qquad (2.38)$$

we then obtain for the antiquark scattering amplitude

$$\begin{aligned}
\mathcal{M}'^{r}_{3'1'}(G) &= i\sqrt{p'_{3+}p'_{1+}}\,\delta_{s'_3s'_1}\int \mathrm{d}x_-\,\mathrm{d}^2x_T\,e^{\frac{i}{2}(p'_3-p'_1)_+x_- - i(\mathbf{p}'_3-\mathbf{p}'_1)_T\cdot\mathbf{x}_T}\\
&\qquad \left[V^*_-(\infty,x_-,\mathbf{x}_T)-\mathbb{1}\right]_{A'_3A'_1},\\
\mathcal{M}'^{r}_{4'2'}(G) &= i\sqrt{p'_{4-}p'_{2-}}\,\delta_{s'_4s'_2}\int \mathrm{d}y_+\,\mathrm{d}^2y_T\,e^{\frac{i}{2}(p'_4-p'_2)_-y_+ - i(\mathbf{p}'_4-\mathbf{p}'_2)_T\cdot\mathbf{y}_T}\\
&\qquad \left[V^*_+(y_+,\infty,\mathbf{y}_T)-\mathbb{1}\right]_{A'_4A'_2}. \qquad (2.39)
\end{aligned}$$

When calculating $\mathcal{S}$-matrix elements for quarks and antiquarks we also have to take into account contributions from disconnected diagrams when applying the LSZ reduction formalism. These diagrams lead to delta functions $\delta(j,k)\,(\delta(j',k'))$ which cancel the $\mathbb{1}$ in the (anti-)quark scattering amplitudes $\mathcal{M}^r_{kj}\,(\mathcal{M}'^{r}_{k'j'})$. In the high energy limit in leading order in s we then find a simple rule for the $\mathcal{S}$-matrix element: for each quark or antiquark we write a certain factor which we obtain from the appropriate quark or antiquark scattering amplitude for fixed external gluon potential $G_\mu(x)$. Then we multiply all these factors and average over all gluon potentials by means of the functional integral (2.16).

The factors are

- for a quark flying in positive x^3 direction ($j \to k$)

$$\mathcal{S}_{q+}(k,j) = \sqrt{p_{k+}p_{j+}}\delta_{s_k s_j} \int \mathrm{d}x_- \, \mathrm{d}^2x_T \, e^{\frac{i}{2}(p_k-p_j)_+ x_- - i(\mathbf{p}_k-\mathbf{p}_j)_T\cdot\mathbf{x}_T} V_-(\infty, x_-, \mathbf{x}_T)_{A_k A_j}, \tag{2.40}$$

- for a quark flying in negative x^3 direction

$$\mathcal{S}_{q-}(k,j) = \sqrt{p_{k-}p_{j-}}\delta_{s_k s_j} \int \mathrm{d}x_+ \, \mathrm{d}^2x_T \, e^{\frac{i}{2}(p_k-p_j)_- x_+ - i(\mathbf{p}_k-\mathbf{p}_j)_T\cdot\mathbf{x}_T} V_-(x_+, \infty, \mathbf{x}_T)_{A_k A_j}, \tag{2.41}$$

- for an antiquark flying in positive x^3 direction ($j' \to k'$)

$$\mathcal{S}_{\bar{q}+}(k',j') = \sqrt{p'_{k+}p'_{j+}}\delta_{s'_k s'_j} \int \mathrm{d}x_- \, \mathrm{d}^2x_T \, e^{\frac{i}{2}(p'_k-p'_j)_+ x_- - i(\mathbf{p}'_k-\mathbf{p}'_j)_T\cdot\mathbf{x}_T} V_-^*(\infty, x_-, \mathbf{x}_T)_{A'_k A'_j} \tag{2.42}$$

- and for an antiquark flying in negative x^3 direction

$$\mathcal{S}_{\bar{q}-}(k',j') = \sqrt{p'_{k-}p'_{j-}}\delta_{s'_k s'_j} \int \mathrm{d}x_+ \, \mathrm{d}^2x_T \, e^{\frac{i}{2}(p'_k-p'_j)_- x_+ - i(\mathbf{p}'_k-\mathbf{p}'_j)_T\cdot\mathbf{x}_T} V_+^*(x_+, \infty, \mathbf{x}_T)_{A'_k A'_j}. \tag{2.43}$$

2.3 Scattering of hadrons

In this section we want to study hadron-hadron scattering. We are interested in two types of scattering reactions. We call the first one "exclusive" scattering, i.e. the final state consists of two definite hadrons which we describe by their according hadronic wave functions. Elastic scattering for example falls into this category,

$$h_1(P_1) + h_2(P_2) \to h_1(P_3) + h_2(P_4), \tag{2.44}$$

but we do not have to limit ourselves to elastic scattering. The diffractive scattering of the initial state hadrons h_1 and h_2 into e.g. excited states h'_1 and h'_2 is also covered by our approach. More generally we write

$$h_1(P_1) + h_2(P_2) \to h_3(P_3) + h_4(P_4), \tag{2.45}$$

where h_3 and h_4 can be any hadrons that are accessible by a soft diffractive process. The second type of reactions we want to study are "semi-inclusive" processes, where

one of the initial state hadrons stays intact and the other one diffractively dissociates into a final state X

$$h_1(P_1) + h_2(P_2) \to h_1(P_3) + X(P_4), \tag{2.46}$$

where X can be any diffractive excitation of h_2. In both cases we use the convention that the hadrons h_1, h_3 move in positive x^3 direction and h_2, h_4 or X, respectively, in negative x^3 direction, i.e. $P_{1+}, P_{3+}, P_{2-}, P_{4-} \to \infty$ in the high energy limit.

In our model we describe mesons as quark-antiquark pairs and the constituent quark configuration of baryons is assumed to be of the quark-diquark type for the reasons given in [35,36], where the point-like diquark is treated like an antiquark in this approach. The baryons then act as colour dipoles like mesons.

The diffractive final state X is modelled by a $q\bar{q}$-pair (or quark-diquark pair) in a colour singlet state. Then we use two approaches. In the first method we use free plane waves for the quark and antiquark and invoke quark-hadron duality. Integration over all allowed values in phase space and the closure relation then yield all possible diffractive final states X, where the case of elastic scattering also is included. The second ansatz, applied to confirm the results of the first method and to gain additional insight into the structure of the calculated differential cross sections, uses the wave functions of a two-dimensional harmonic oscillator where the ground state corresponds to hadron h_2 and the excited states to the diffractive excitations of h_2. Since these eigenfunctions form a basis, the contributions from different excited states are orthogonal to each other and the calculation of cross sections can be performed as follows: first the cross section for one specific excited state with definite quantum numbers n, m is calculated and then the sum over all excited states is taken to get the inelastic semi-inclusive diffractive cross section.

The momenta p of the quark and p' of the antiquark (or diquark, respectively) in a hadron (or the diffractive final state X) with momentum P are parametrised using light-cone variables by

$$\begin{aligned} p_\pm &= zP_\pm, & p'_\pm &= (1-z)P_\pm, \\ \mathbf{p}_T &= z\mathbf{P}_T + \boldsymbol{\Delta}_T, & \mathbf{p}'_T &= (1-z)\mathbf{P}_T - \boldsymbol{\Delta}_T. \end{aligned} \tag{2.47}$$

Here z is the longitudinal momentum fraction carried by the quark. The relative transverse momentum between the quark and the antiquark (diquark) is given by

$$\boldsymbol{\Delta}_T = \frac{\mathbf{p}_T - \mathbf{p}'_T}{2} + \left(\frac{1}{2} - z\right)\mathbf{P}_T. \tag{2.48}$$

Lorentz invariance requires z to appear also in the transverse momenta $\mathbf{p}_T$ and $\mathbf{p}'_T$ as defined above.

2.3.1 Exclusive scattering

The hadronic scattering amplitude is obtained by folding the underlying partonic $\mathcal{S}$-matrix element with suitable hadronic wave functions, where the hadrons will be

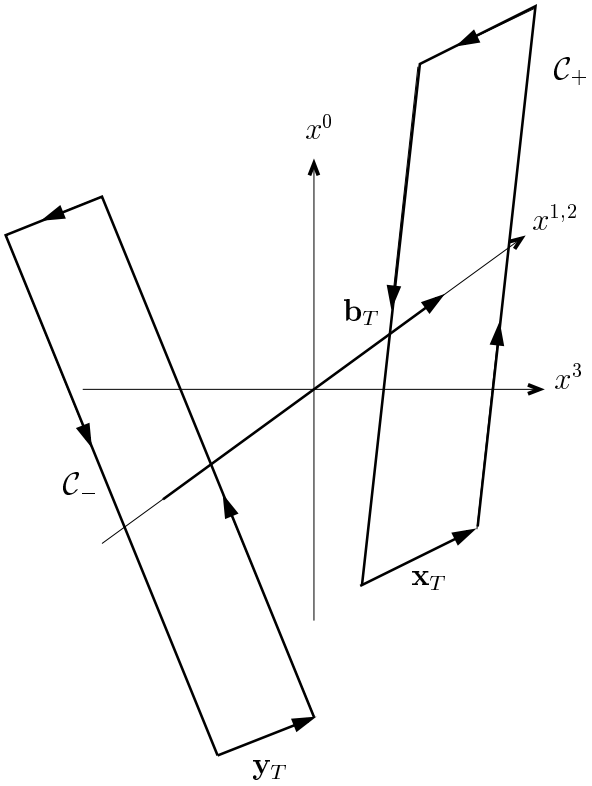

Figure 2.1: Two light-like Wegner-Wilson loops in position space

formed of parton wave packets as explained above. Proceeding as in [24, 33], i.e. applying the rules (2.40)-(2.43) and with (2.47),(2.48), we find

$$\begin{aligned} \mathcal{S}_{fi} &= \delta_{fi} + i(2\pi)^4\delta^{(4)}(P_3 + P_4 - P_1 - P_2)\mathcal{T}_{fi} \\ \mathcal{T}_{fi} &= 2is \int \mathrm{d}^2 b_T \, e^{i\mathbf{q}_T\cdot\mathbf{b}_T} \hat{J}_{\mathrm{excl}}(\mathbf{b}_T), \end{aligned} \tag{2.49}$$

with the exclusive profile function

$$\begin{aligned} \hat{J}_{\mathrm{excl}}(\mathbf{b}_T) &= -\int \mathrm{d}^2 x_T \, \mathrm{d}^2 y_T \int_0^1 \mathrm{d}z \, \mathrm{d}z' w_{31}(\mathbf{x}_T, z) w_{42}(\mathbf{y}_T, z') \\ &\quad \Big\langle \mathcal{W}_+(\frac{1}{2}\mathbf{b}_T + (\frac{1}{2} - z)\mathbf{x}_T, \mathbf{x}_T)\mathcal{W}_-(-\frac{1}{2}\mathbf{b}_T + (\frac{1}{2} - z')\mathbf{y}_T, \mathbf{y}_T) - \mathbb{1} \Big\rangle_G, \end{aligned} \tag{2.50}$$

as has been found for the case of elastic scattering in [30]. Here $\mathcal{W}_\pm$ are the light-like Wegner-Wilson loops

$$\mathcal{W}_\pm := \frac{1}{3}\,\mathrm{tr}\, V(C_\pm) = \frac{1}{3}\,\mathrm{tr}\ \mathrm{P}\exp\left(-ig\int_{C_\pm} \mathrm{d}x^\mu G^a_\mu(x)\frac{\lambda^a}{2}\right), \tag{2.51}$$

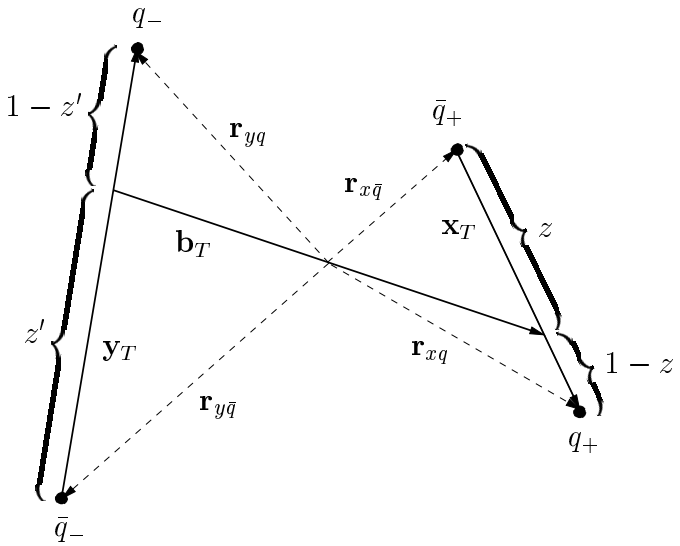

Figure 2.2: The orientation and extension of the light-like Wegner-Wilson loops in a projection into transverse position space

where P denotes path ordering and $C_\pm$ is the curve consisting of two light-like worldlines for the quark and the antiquark (or diquark, respectively) and connecting pieces at $\pm\infty$ (see Fig. 2.1), which ensure gauge invariance. $\mathbf{x}_T$ and $\mathbf{y}_T$ define the extension and orientation in transverse position space of the two loops representing the two hadrons h_1 and h_2 respectively, z (z') parametrises the fraction of the longitudinal momentum of hadron h_1 (h_2) carried by the quark (see (2.47)). The impact parameter is given by $\mathbf{b}_T$, the light-cone barycentres of the loops are located at $\frac{1}{2}\mathbf{b}_T + (\frac{1}{2} - z)\mathbf{x}_T$ and $-\frac{1}{2}\mathbf{b}_T + (\frac{1}{2} - z')\mathbf{y}_T$, respectively (see [27] and Fig. 2.2). As x-axis for the transverse vectors $\mathbf{x}_T$, $\mathbf{y}_T$ and $\mathbf{b}_T$ we choose $\mathbf{q}_T$.

The symbol $\langle \ldots \rangle_G$ denotes the functional integration which correlates the two loops. In (2.50) the loop-loop correlation function is multiplied with the functions $w_{31}(\mathbf{x}_T, z)$ and $w_{42}(\mathbf{y}_T, z')$. These functions $w_{kj}(\mathbf{x}_T, z)$ denote the overlap between initial state hadron h_j and final state hadron h_k for fixed transverse extension $\mathbf{x}_T$ and fixed longitudinal momentum fraction z. Then we have to integrate over all extensions and orientations $\mathbf{x}_T, \mathbf{y}_T$ of the loops in transverse space as well as over the longitudinal momentum fractions z, z' respectively. Finally a Fourier transform with respect to the impact parameter $\mathbf{b}_T$ has to be performed, as in the case of quark-quark scattering.

2.3.2 Semi-inclusive scattering

Except for the replacement $h_4(P_4) \to X(P_4)$ everything remains unchanged when we want to describe the inelastic diffractive dissociation reaction (2.46) and we find

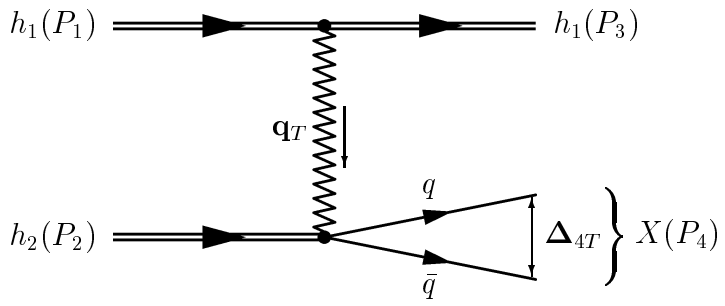

Figure 2.3: The semi-inclusive scattering reaction $h_1 + h_2 \to h_1 + X$

in analogy to (2.49)

$$\begin{aligned} \mathcal{S}_{fi} &= \delta_{fi} + i(2\pi)^4 \delta^{(4)}(P_3 + P_4 - P_1 - P_2)\mathcal{T}_{fi} \\ \mathcal{T}_{fi} &= 2is \int \mathrm{d}^2 b_T \, e^{i\mathbf{q}_T \cdot \mathbf{b}_T} \hat{J}_{\mathrm{diss}}, \end{aligned} \tag{2.52}$$

where we have to use the profile function $\hat{J}_{\mathrm{diss}}$ now. As stated before, we are going to use two different ansätze for X, leading to two expressions for the profile functions, depending on which description for the diffractive final state we use in the calculation.

For the plane wave description we obtain

$$\begin{aligned} \hat{J}^{\mathrm{p.wave}}_{\mathrm{diss}}(\mathbf{b}_T, z') = -\int \mathrm{d}^2 x_T \, \mathrm{d}^2 y_T \int_0^1 \mathrm{d}z \; w_{31}(\mathbf{x}_T, z) \\ \sqrt{2\pi}\sqrt{2z'(1-z')}\, e^{-i\mathbf{\Delta}_{4T}\cdot\mathbf{y}_T} \; \varphi_2(\mathbf{y}_T, z') \\ \Big\langle \mathcal{W}_+(\frac{1}{2}\mathbf{b}_T + (\frac{1}{2} - z)\mathbf{x}_T, \mathbf{x}_T)\mathcal{W}_-(-\frac{1}{2}\mathbf{b}_T + (\frac{1}{2} - z')\mathbf{y}_T, \mathbf{y}_T) - \mathbb{1} \Big\rangle_G, \end{aligned} \tag{2.53}$$

where $\mathbf{\Delta}_{4T}$ is the relative transverse momentum between the quark and the antiquark (or diquark) of X (see (2.48) and Fig. 2.3). Instead of the overlap function w_{42} occurring in (2.50) here we have got the product of the plane wave and the wave function φ_2 of the incoming hadron h_2.

For the oscillator description we obtain

$$\begin{aligned} \hat{J}^{\mathrm{2d\ osc}}_{\mathrm{diss}}(\mathbf{b}_T) = -\int \mathrm{d}^2 x_T \, \mathrm{d}^2 y_T \int_0^1 \mathrm{d}z \int_0^1 \mathrm{d}z' \; w_{31}(\mathbf{x}_T, z)\, X^{n,m}(\mathbf{y}_T, z')\, \varphi_2(\mathbf{y}_T, z') \\ \Big\langle \mathcal{W}_+(\frac{1}{2}\mathbf{b}_T + (\frac{1}{2} - z)\mathbf{x}_T, \mathbf{x}_T)\mathcal{W}_-(-\frac{1}{2}\mathbf{b}_T + (\frac{1}{2} - z')\mathbf{y}_T, \mathbf{y}_T) - \mathbb{1} \Big\rangle_G. \end{aligned} \tag{2.54}$$

Here $X^{n,m}(\mathbf{y}_T, z')$ stands for the two-dimensional harmonic oscillator wave function with quantum numbers n, m. Again, this function has to be multiplied by φ_2, describing the incoming hadron h_2. Inserting in (2.54) the ground state wave function

$X^{0,0}$ leads to the elastic scattering amplitude, which we also get from (2.49),(2.50) with $h_4 = h_2$, $h_3 = h_1$.

In the plane wave description z' is part of the specification of the final state and thus appears as argument of $\hat{J}^{\text{p.wave}}_{\text{diss}}(\mathbf{b}_T, z')$ in (2.53). The phase space integral then includes an integration over z'. When using the second method involving the two-dimensional oscillator functions to describe the diffractive final state, one has to insert the function $X^{n,m}$ on the r.h.s. of (2.54) and to integrate over z'. Thus $\hat{J}^{\text{2d osc}}_{\text{diss}}(\mathbf{b}_T)$ depends for given oscillator function $X^{n,m}$ on $\mathbf{b}_T$ only.

Chapter 3

Evaluation of the scattering amplitudes

The next step is to evaluate the scattering amplitude (2.49), where the main part will be to calculate the loop-loop correlation function appearing in (2.50), (2.53) and (2.54), respectively. For this task we will make use of the model of the stochastic vacuum (MSV), which has been introduced by Dosch and Simonov [25]. The model is based on a small number of physically well motivated assumptions and allows us to compute the relevant quantities we need for the description of high energy scattering, e.g. the expectation values of Wegner-Wilson lines and loops. Furthermore we have to specify suitable hadronic wave functions φ_j and to construct from them the overlap functions w_{kj} appearing in (2.50), (2.53) and (2.54). Once we know how to calculate the correlation function by applying the model of the stochastic vacuum and after defining the wave functions we can analyse the symmetry properties of the scattering amplitudes. These considerations will allow us to classify which quantum numbers can be exchanged in the different reactions we are studying.

3.1 The loop-loop correlation function in the model of the stochastic vacuum

According to present knowledge the vacuum has a highly nontrivial structure governed by chromoelectric and -magnetic background fields. It has been first noted by Savvidy [45] that the mean energy density of the vacuum can be lowered by adding a constant chromomagnetic background field to the perturbative vacuum. The minimal value of the energy density is obtained for a value of the chromomagnetic field strength $B \neq 0$, i.e. the vacuum spontaneously develops a chromomagnetic background field, analogous to the spontaneous magnetisation of ferromagnets below the Curie temperature.

Of course the QCD vacuum state must be relativistically invariant and must not have a preferred direction in ordinary and colour space. In analogy to Weiss

domains in a ferromagnet, states composed of domains with random orientation of the gluon field strength have been proposed. The vacuum state then is build of a linear superposition of such states with various domains, where the fields inside the domains are oriented in various directions. As well the boundaries of the domains as the orientation of the fields inside of them will fluctuate.

An important step in the investigations of the QCD vacuum structure was achieved by Shifman, Vainshtein and Zakharov [21] with the introduction of the QCD condensates. In this way, nonperturbative components entered the perturbative description of the QCD vacuum. With the introduction of nonlocal condensates one can go even one step further and study long-distance effects as for example confinement. Because QCD is a non-abelian theory, nonlocal condensates can a priori not be defined in a gauge-invariant way. To cure this problem we introduce so-called connectors as the non-abelian generalisation of the Schwinger string of QED, which allow us to define parallel-transported quantities such as the parallel-transported gluon field strength (see Appendix B). Then we can define gauge-invariant nonlocal condensates by shifting the occurring field strengths to a common reference point.

The model of the stochastic vacuum incorporates many of the above ideas. Its strongest assumption is that the nonperturbative behaviour of QCD can be approximated by a Gaussian process where the field strengths are the stochastic variables. This assumption already allows us to derive confinement in the framework of the model.

3.1.1 Properties of the model of the stochastic vacuum

In this section we will present the Minkowskian formulation of the model of the stochastic vacuum. A more detailed presentation of the model can be found in [23–26], where both the original formulation in Euclidian space-time and the analytic continuation to Minkowskian space-time are discussed.

The starting point for the model is the correlator of two gluon field strength tensors $G^a_{\mu\nu}$ at points x_1 and x_2, parallel-transported to a common reference point o along the two curves C_{x_1} and C_{x_2}:

$$\left\langle \frac{g^2}{4\pi^2}\hat{G}^a_{\mu\nu}(o,x_1;C_{x_1})\hat{G}^{\mu\nu b}(o,x_2;C_{x_2})\right\rangle_G \equiv \frac{1}{4}\delta^{ab}F_{\mu\nu\rho\sigma}(x_1,x_2,o;C_{x_1},C_{x_2}). \qquad (3.1)$$

The right hand side depends only on the points x_1, x_2 and the two curves C_{x_1}, C_{x_2}, the common reference point o can be freely shifted along the curve $C_{12} = C_{x_1} + \bar{C}_{x_2}$. Due to colour conservation, the correlation function is proportional to δ^{ab}. In the MSV the strong assumption is made that $F_{\mu\nu\rho\sigma}$ is independent of the choice of the connecting curve C_{12}:

Assumption I: $F_{\mu\nu\rho\sigma}$ is independent of o and C_{x_1}, C_{x_2}.

Then Poincaré and parity invariance require $F_{\mu\nu\rho\sigma}$ to be of the following form:

$$\begin{aligned} F_{\mu\nu\rho\sigma}(z) &= \frac{1}{24}G_2\Big\{(g_{\mu\rho}g_{\nu\sigma}-g_{\mu\sigma}g_{\nu\rho})\left[\kappa D(z^2)+(1-\kappa)D_1(z^2)\right] \\ &\quad +(z_\sigma z_\nu g_{\mu\rho}-z_\rho z_\nu g_{\mu\sigma}+z_\rho z_\mu g_{\nu\sigma}-z_\sigma z_\mu g_{\nu\rho})(1-\kappa)\frac{\mathrm{d}D_1(z^2)}{\mathrm{d}z^2}\Big\}, \quad (3.2) \\ G_2 &\equiv \frac{1}{4\pi^2}\langle g^2FF\rangle = \langle 0|\frac{g^2}{4\pi^2}G^a_{\mu\nu}(0)G^{a\mu\nu}(0)|0\rangle, \quad (3.3) \end{aligned}$$

where $z = x_1 - x_2$.
Here G_2 is proportional to the gluon condensate $\langle 0|G^a_{\mu\nu}(0)G^{a\mu\nu}(0)\,|0\rangle$, D and D_1 are invariant functions normalised to 1 at $z = 0$, $D(0) = D_1(0) = 1$, and κ is a parameter determining the non-abelian character of the correlator. The properties of the functions D and D_1 are further specified through the second assumption of the MSV:

Assumption II: For space-like separations the functions D, D_1 rapidly fall to zero on a scale given by the correlation length $a \approx 0.3$ fm.

The Fourier decomposition of those functions is given by

$$\begin{aligned} D(z^2) &= \int_{-\infty}^{\infty}\frac{\mathrm{d}^4k}{(2\pi)^4}e^{-ikz}\widetilde{D}(k^2), \\ D_1(z^2) &= \int_{-\infty}^{\infty}\frac{\mathrm{d}^4k}{(2\pi)^4}e^{-ikz}\widetilde{D}_1(k^2). \quad (3.4) \end{aligned}$$

A suitable ansatz for $\widetilde{D}$ and $\widetilde{D}_1$ is given in [24]:

$$\begin{aligned} \widetilde{D}(k^2) &= \frac{27(2\pi)^4}{(8a)^2}\frac{ik^2}{(k^2-\lambda^{-2}+i\epsilon)^4}, \\ \widetilde{D}_1(k^2) &= \frac{2}{3}\frac{27(2\pi)^4}{(8a)^2}\frac{i}{(k^2-\lambda^{-2}+i\epsilon)^3}, \quad (3.5) \end{aligned}$$

with the constant $\lambda = 8a/3\pi$. The functions of (3.4),(3.5) can be compared to lattice calculations [46, 47] for the Euclidian version of the correlator (3.1) and from a fit one can extract the following ranges for the parameters G_2, a, κ [47]:

$$\begin{aligned} \kappa G_2 a^4 &= 0.39 \ldots 0.41, \\ \kappa &= 0.80 \ldots 0.89, \\ a &= 0.33 \ldots 0.37 \text{ fm}. \quad (3.6) \end{aligned}$$

Assumption III: The vacuum fluctuations of the field strengths are determined by a Gaussian process.

This implies that correlators of more than two gluon field strengths factorise and thus the process is completely defined by the second moment of its distribution. The expectation value of one single parallel-transported gluon field strength tensor vanishes due to colour conservation and the fact that the QCD vacuum has no preferred direction in colour space:

$$\langle \hat{G}(i) \rangle_G = 0, \tag{3.7}$$

where we have used the abbreviation

$$\hat{G}(i) \equiv \hat{G}^{a_i}_{\mu_i \nu_i}(o, x_i; C_{x_i}). \tag{3.8}$$

Due to the assumption of a Gaussian process and colour conservation all n-point functions with odd n vanish as well and we are therefore left with

$$\langle \hat{G}(1) \dots \hat{G}(2n) \rangle_G = \sum_{\text{all pairings}} \langle \hat{G}(i_1)\hat{G}(i_2) \rangle_G \dots \langle \hat{G}(i_{2n-1})\hat{G}(i_{2n}) \rangle_G. \tag{3.9}$$

3.1.2 Application of the model of the stochastic vacuum to the correlation function

Now we will make a cumulant expansion [33] for the loop-loop correlation function

$$\left\langle \mathcal{W}_+ \mathcal{W}_- \right\rangle_G \equiv \left\langle \mathcal{W}_+(\frac{1}{2}\mathbf{b}_T + (\frac{1}{2} - z)\mathbf{x}_T, \mathbf{x}_T)\mathcal{W}_-(-\frac{1}{2}\mathbf{b}_T + (\frac{1}{2} - z')\mathbf{y}_T, \mathbf{y}_T) \right\rangle_G \tag{3.10}$$

in (2.50), or (2.53), (2.54), respectively, and then evaluate the result in the framework of the MSV.
To expand the correlation function, we proceed as explained in [30]. First the line integrals along the closed loops $C_\pm$ are transformed to surface integrals with the help of the non-abelian Stokes theorem where, following the authors of [24], we choose the mantle of a double pyramid as the integration surface. The basis surfaces $S_\pm$ of the two pyramids are enclosed by the two loops $C_\pm$ (see Fig. 3.1). The common reference point o is chosen to be the apex, where both pyramids touch, and P_+ and P_- are the mantle surfaces of the two pyramids, respectively. Following [30] we rewrite the two traces over 3×3 matrices occurring in (3.10) after inserting (2.51) as one trace (Tr_2) of a matrix acting in the 9-dimensional tensor product space. With the definition

$$\hat{G}_{t,\mu\nu}(o, x; C_x) := \begin{cases} \hat{G}^a_{\mu\nu}(o, x; C_x)(\frac{\lambda_a}{2} \otimes \mathbb{1}) & \text{for} \quad x \in P_+ \\ \hat{G}^a_{\mu\nu}(o, x; C_x)(\mathbb{1} \otimes \frac{\lambda_a}{2}) & \text{for} \quad x \in P_- \end{cases}, \tag{3.11}$$

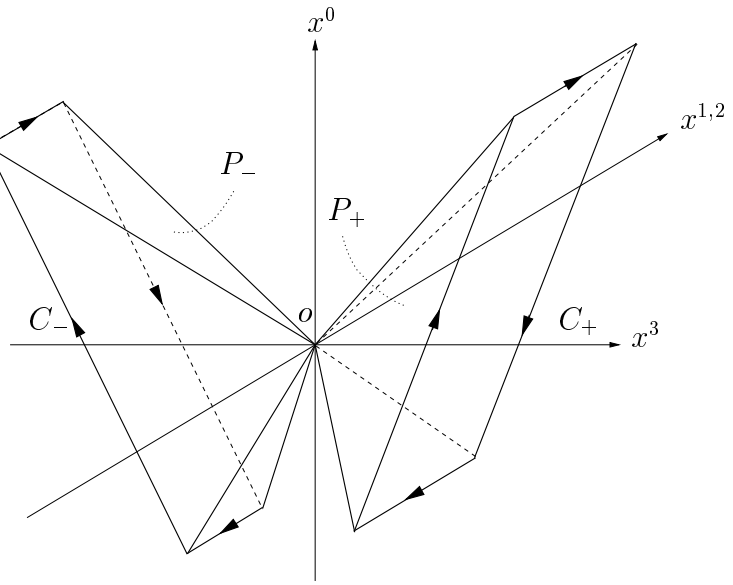

Figure 3.1: The integration surfaces for the evaluation of the loop-loop correlation function

we can write (3.10) as the expectation value of one ordered exponential in the product space, where the integration surface is given by the mantle $P = P_+ \cup P_-$ of the double pyramid:

$$\langle \mathcal{W}_+ \mathcal{W}_- \rangle_G = \frac{1}{9} \operatorname{Tr}_2 \left\langle \mathrm{P} \exp \left(-\frac{ig}{2} \int_P \mathrm{d}\sigma^{\mu\nu}(x)\, \hat{G}_{t,\mu\nu}(o, x; C_x) \right) \right\rangle_G . \tag{3.12}$$

The cumulant expansion of this expression up to the second term reads

$$\begin{aligned} &\Big\langle \mathcal{W}_+(\frac{1}{2}\mathbf{b}_T + (\frac{1}{2} - z)\mathbf{x}_T, \mathbf{x}_T) \mathcal{W}_-(-\frac{1}{2}\mathbf{b}_T + (\frac{1}{2} - z')\mathbf{y}_T, \mathbf{y}_T) \Big\rangle_G \\ &\quad = \frac{1}{9} \operatorname{Tr}_2 \exp \Big(-\frac{g^2}{8} \int_P \mathrm{d}\sigma^{\mu\nu}(x) \int_P \mathrm{d}\sigma^{\rho\sigma}(x') \\ &\qquad\qquad \Big\langle \mathrm{P}(\hat{G}_{t,\mu\nu}(o, x; C_x) \hat{G}_{t,\rho\sigma}(o, x'; C_{x'})) \Big\rangle_G \Big) \\ &\quad =: \frac{1}{9} \operatorname{Tr}_2 \exp C_2(\mathbf{b}_T, \mathbf{x}_T, \mathbf{y}_T, z, z'), \end{aligned} \tag{3.13}$$

where C_2 is a 9×9 matrix invariant unter SU(3) colour rotations. As shown in [30] this finally leads to

$$\langle \mathcal{W}_+ \mathcal{W}_- \rangle_G = \frac{2}{3} e^{-i\frac{1}{3}\chi} + \frac{1}{3} e^{i\frac{2}{3}\chi} \tag{3.14}$$

with

$$\begin{aligned}
\chi(\mathbf{b}_T,\mathbf{x}_T,\mathbf{y}_T,z,z') &= \frac{G_2\pi^2}{24}\left\{I(\mathbf{r}_{xq},\mathbf{r}_{yq})+I(\mathbf{r}_{x\bar{q}},\mathbf{r}_{y\bar{q}})-I(\mathbf{r}_{xq},\mathbf{r}_{y\bar{q}})-I(\mathbf{r}_{x\bar{q}},\mathbf{r}_{yq})\right\},\\
I(\mathbf{r}_x,\mathbf{r}_y) &= \kappa\frac{\pi}{2}\lambda^2\,\mathbf{r}_y\cdot\mathbf{r}_x\int_0^1 \mathrm{d}v\left\{\left(\frac{|v\mathbf{r}_y-\mathbf{r}_x|}{\lambda}\right)^2 K_2\left(\frac{|v\mathbf{r}_y-\mathbf{r}_x|}{\lambda}\right)\right.\\
&\qquad\left.+\left(\frac{|\mathbf{r}_y-v\mathbf{r}_x|}{\lambda}\right)^2 K_2\left(\frac{|\mathbf{r}_y-v\mathbf{r}_x|}{\lambda}\right)\right\}\\
&\quad+(1-\kappa)\pi\lambda^4\left(\frac{|\mathbf{r}_y-\mathbf{r}_x|}{\lambda}\right)^3 K_3\left(\frac{|\mathbf{r}_y-\mathbf{r}_x|}{\lambda}\right). \qquad (3.15)
\end{aligned}$$

Here G_2,λ,κ are as defined in (3.2),(3.5) and $K_{2,3}$ are the modified Bessel functions of second and third degree. The vectors $\mathbf{r}_{ij}$ with $i=x,y$ and $j=q,\bar{q}$ are those from the coordinate origin to the positions of the quarks and antiquarks (or diquarks) in transverse space as shown in Fig. 2.2. Separating the real and the imaginary part of the above expression (χ is a real function) we get

$$\begin{aligned}
&\left\langle \mathcal{W}_+(\frac{1}{2}\mathbf{b}_T+(\frac{1}{2}-z)\mathbf{x}_T,\mathbf{x}_T)\mathcal{W}_-(-\frac{1}{2}\mathbf{b}_T+(\frac{1}{2}-z')\mathbf{y}_T,\mathbf{y}_T)-\mathbb{1}\right\rangle_G\\
&\quad= \left\{\frac{2}{3}\cos\left(\frac{1}{3}\chi(\mathbf{b}_T,\mathbf{x}_T,\mathbf{y}_T,z,z')\right)+\frac{1}{3}\cos\left(\frac{2}{3}\chi(\mathbf{b}_T,\mathbf{x}_T,\mathbf{y}_T,z,z')\right)-1\right.\\
&\qquad\left.-i\frac{2}{3}\sin\left(\frac{1}{3}\chi(\mathbf{b}_T,\mathbf{x}_T,\mathbf{y}_T,z,z')\right)+i\frac{1}{3}\sin\left(\frac{2}{3}\chi(\mathbf{b}_T,\mathbf{x}_T,\mathbf{y}_T,z,z')\right)\right\}. \qquad (3.16)
\end{aligned}$$

This is the final result for the correlation function of two light-like Wegner-Wilson loops in the matrix cumulant method [30]. If we assume $|\chi|\ll 1$, (3.16) reduces to

$$\langle\mathcal{W}_+\mathcal{W}_--\mathbb{1}\rangle_G=\left\{-\frac{1}{9}\,\chi(\mathbf{b}_T,\mathbf{x}_T,\mathbf{y}_T,z,z')^2\right\}, \qquad (3.17)$$

neglecting terms of order χ^3 and higher. This is the result of the traditional expansion method [24]. When computing the numerical results for the cross sections we are interested in, we will use both (3.16) and (3.17) and compare with experimental data.

3.2 The hadronic wave functions

We now have to specify the hadronic wave functions and overlap functions occurring in (2.50), (2.53) and (2.54). As mentioned before we make a simple ansatz and

construct mesons as quark-antiquark and baryons as quark-diquark wave packets, where scalar diquarks should be favoured above vector diquarks due to dynamical reasons [48]. This means that in our model the spin of a baryon is carried by the quark.

In the following we will deal mainly with hadrons with angular momentum $L = 0$, in particular the proton and the pion. When studying the scattering of protons and pions we are only interested in unpolarised cross sections and due to helicity conservation on the parton level in our model we can therefore limit ourselves to the description of spinless s-wave states. For the corresponding wave functions we make a Wirbel-Stech-Bauer ansatz [37], which assumes a Gaussian-shaped distribution for both the longitudinal momentum fraction z carried by the quark in the hadron and the transverse spatial extension $\mathbf{x}_T$ of the hadron

$$\varphi_j(\mathbf{x}_T, z) = \sqrt{\frac{2z(1-z)}{2\pi S_{h_j}^2 I_{h_j}}}\, e^{-(z-\frac{1}{2})^2/4z_{h_j}^2}\, e^{-x_T^2/4S_{h_j}^2}. \tag{3.18}$$

where z_{h_j} and S_{h_j} are the parameters defining the widths of the longitudinal momentum and transverse extension distributions of hadron h_j, respectively. The normalisation constant I_{h_j} is given by

$$I_{h_j} = \int_0^1 \mathrm{d}z\, 2z(1-z)\, e^{-(z-\frac{1}{2})^2/2z_{h_j}^2}. \tag{3.19}$$

Only in our study of the double diffractive excitation of two protons into excited nucleon resonances, namely the $N(1535)$, which has the quantum numbers $I(J^P) = \frac{1}{2}(\frac{1}{2}^-)$ with $L = 1$ in the quark-diquark picture, we also need p-wave functions. To construct the $N(1535)$ wave function we have to couple a spin 1/2 state to a p-wave in such a way that the total angular momentum $J = 1/2$, taking into account the proper Clebsch-Gordan coefficients. This means that the spin of the quark, which carries the total spin of the hadron, because we use scalar diquarks as explained above, is antiparallel to the helicity of the p-wave. As our model conserves the helicities on the parton level and again we are calculating unpolarised cross sections only, the scattering of two protons into two excited resonances is reduced to the scattering of two spinless s-waves in the initial state into two spinless p-waves with fixed helicities in the final state. In the following we give only the $\lambda = \pm 1$ helicity states of the wave function, since due to the replacement of the Gaussian-shaped z-dependence of the Wirbel-Stech-Bauer ansatz by a delta function centred at $z = 1/2$ in the numerical analysis, the $\lambda = 0$ state does not contribute, because it contains a factor proportional to $z - (1 - z)$, which is identical to 0 when z is fixed to 1/2. As the contribution of the $\lambda = 0$ state is strongly suppressed compared to those of the $\lambda = \pm 1$ states as well in the formulation using the Gaussian-shaped z-distribution, which also is centred around $z = 1/2$, the replacement by the delta function has no substantial impact on the numerical results. The reason for this

approximation is discussed more detailed in chapter 4. To keep the expression for the wave function short, we make this simplification here as well and thus avoid the otherwise occurring $\lambda = 0$ term. For the spinless p-wave we extend the original Wirbel-Stech-Bauer ansatz to angular momentum $L = 1$ and obtain

$$\varphi_j^{\lambda}(\mathbf{x}_T, z) = \frac{x_T\, e^{-x_T^2/4S_{h_j}^2}}{\sqrt{6\pi S_{h_j}^4}}\, \lambda e^{i\lambda\theta_x}\, \delta(z - \tfrac{1}{2}), \qquad \lambda = \pm 1. \tag{3.20}$$

Here θ_x is the angle between $\mathbf{x}_T$ and $\mathbf{q}_T$.

As the overlap function $w_{kj}(\mathbf{x}_T, z)$ we define the overlap between hadron h_j in the initial and hadron h_k in the final state for fixed transverse extension $\mathbf{x}_T$ and fixed longitudinal momentum fraction z

$$w_{kj}^{(\lambda)}(\mathbf{x}_T, z) := (\varphi_k^{(\lambda)}(\mathbf{x}_T, z))^*\, \varphi_j(\mathbf{x}_T, z), \tag{3.21}$$

where the helicity index λ occurs only in case we deal with a p-wave in the final state.

For the description of the diffractive final state X in semi-inclusive scattering we use in our second ansatz the wave functions $X^{n,m}$, which consist of the eigenfunctions $\tilde{X}^{n,m}(\mathbf{y}_T, z')$ of a two-dimensional harmonic oscillator [49] for the $\mathbf{y}_T$-dependence and an additional part for the z'-dependence as in (3.18):

$$\begin{aligned}
X^{n,m}(\mathbf{y}_T, z') &= \sqrt{\frac{2z'(1-z')}{I_{h_j}}}\, e^{-(z'-\frac{1}{2})^2/4z_{h_j}^2}\, \tilde{X}^{n,m}(\mathbf{y}_T), \\
\tilde{X}^{n,m}(\mathbf{y}_T) &= \frac{1}{\sqrt{((n+m)/2)!\,((n-m)/2)!}} \left[\sqrt{\frac{S_{h_j}^2}{2}}\left(\frac{y_T}{2S_{h_j}^2} + \frac{m}{y_T} - \frac{\mathrm{d}}{\mathrm{d}y_T}\right)\right]^{\frac{n+m}{2}} \\
&\quad \left[\sqrt{\frac{S_{h_j}^2}{2}}\left(\frac{y_T}{2S_{h_j}^2} - \frac{m}{y_T} - \frac{\mathrm{d}}{\mathrm{d}y_T}\right)\right]^{\frac{n-m}{2}} \frac{e^{-y_T^2/4S_{h_j}^2}}{\sqrt{2\pi S_{h_j}^2}}\, e^{im\theta_y},
\end{aligned} \tag{3.22}$$

where θ_y is the angle between $\mathbf{y}_T$ and $\mathbf{q}_T$. Here of course, we also have angular momentum $L \neq 0$ except for the ground state wave function $X^{0,0}$.

3.3 The hadronic scattering amplitudes

In the following we will deal with three types of hadron-hadron reactions: the first one is elastic scattering, which falls into the category of the exclusive processes discussed in section 2.3.1. As a semi-inclusive process (see section 2.3.2) we will study single diffractive dissociation. Double diffractive excitation, which again is an exclusive process, is the third type of scattering reaction we are investigating.

After having evaluated the loop-loop correlation function in 3.1.2 and with the wave functions from the previous section, we give the expressions for the hadronic scattering amplitudes for these processes and analyse their respective symmetry properties.

3.3.1 Elastic scattering

We now put everything together, inserting the overlap functions (3.21) and the results (3.16) or (3.17) for the correlation function of the Wegner-Wilson loops, depending on which method is used in the evaluation, in (2.50), where we set $h_3 = h_1$, $h_4 = h_2$.

We can simplify the resulting expression by exploiting symmetry properties of the wave and correlation functions. The replacements $\mathbf{x}_T \to -\mathbf{x}_T$ and $z \to 1 - z$, which exchange the quark with the corresponding diquark (or antiquark in the case of mesons) in hadron h_1, lead to $\chi \to -\chi$ (see Fig. 2.2 and (3.15)). On the other hand these replacements leave the wave functions invariant and thus the integration over $\mathbf{x}_T$ and z averages out the $\sin\chi$-terms of (3.16) when inserted in (2.50). We can therefore replace (3.16) by

$$\langle \mathcal{W}_+ \mathcal{W}_- - \mathbb{1} \rangle_G \to \left\{ \frac{2}{3} \cos\left(\frac{1}{3}\chi\right) + \frac{1}{3} \cos\left(\frac{2}{3}\chi\right) - 1 \right\}. \tag{3.23}$$

In the expansion method $\langle \mathcal{W}_+ \mathcal{W}_- - \mathbb{1} \rangle_G$ in (3.17) is already even under $\chi \to -\chi$. In our model, therefore, the expression for the correlation function is purely real in (3.17) and only the real part of (3.16) contributes. The $\mathcal{T}$-matrix element is invariant under the exchange of hadron h_1 by its antihadron. Thus we get only $C = P = +1$ (pomeron) exchange and no $C = P = -1$ (odderon) exchange.

Furthermore it is useful to take advantage of global azimuthal invariance and define as new integration variables the relative angles between the impact parameter $\mathbf{b}_T$ and $\mathbf{x}_T$ and $\mathbf{y}_T$, respectively:

$$\theta'_x = \theta_x - \theta_b, \qquad \theta'_y = \theta_y - \theta_b. \tag{3.24}$$

With this choice of variables the elastic profile function becomes independent of θ_b and using the relation

$$\int_0^{2\pi} \mathrm{d}\theta_b \, e^{i\sqrt{-t}\, b_T} \, e^{in\theta_b} = 2\pi i^n J_n(\sqrt{-t}\, b_T), \tag{3.25}$$

where J_n is the Bessel function of n-th degree, we can perform the integral over the angle of the impact parameter in (2.49) analytically.

For elastic scattering our final result for the scattering amplitude then reads

$$\mathcal{T}_{fi} = 4\pi i s \int_0^\infty \mathrm{d}b_T \, b_T \, J_0(\sqrt{-t}\, b_T) \, \hat{J}_{\mathrm{el}}(\mathbf{b}_T), \tag{3.26}$$

with the elastic profile function

$$\begin{aligned}\hat{J}_{\rm el}(\mathbf{b}_T) &= -\int \mathrm{d}^2x_T\,\mathrm{d}^2y_T \int_0^1 \mathrm{d}z\,\mathrm{d}z' w_{11}(\mathbf{x}_T,z)w_{22}(\mathbf{y}_T,z') \\ &\quad \left\{\frac{2}{3}\cos\left(\frac{1}{3}\chi(\mathbf{b}_T,\mathbf{x}_T,\mathbf{y}_T,z,z')\right)+\frac{1}{3}\cos\left(\frac{2}{3}\chi(\mathbf{b}_T,\mathbf{x}_T,\mathbf{y}_T,z,z')\right)-1\right\}\end{aligned} \tag{3.27}$$

when using the matrix cumulant method and

$$\begin{aligned}\hat{J}_{\rm el}(\mathbf{b}_T) &= -\int \mathrm{d}^2x_T\,\mathrm{d}^2y_T \int_0^1 \mathrm{d}z\,\mathrm{d}z' w_{11}(\mathbf{x}_T,z)w_{22}(\mathbf{y}_T,z') \\ &\quad \left\{-\frac{1}{9}\,\chi(\mathbf{b}_T,\mathbf{x}_T,\mathbf{y}_T,z,z')^2\right\}\end{aligned} \tag{3.28}$$

when using the expansion method, respectively.

3.3.2 Single diffractive dissociation

In analogy to elastic scattering we insert the overlap function w_{11} and either (3.16) or (3.17) into $\hat{J}_{\rm diss}$, for which we have two expressions, (2.53) and (2.54), depending on the choice of the plane wave or the harmonic oscillator description of the diffractive final state X. If using the latter expression, we also have to input the excited state wave functions $X^{n,m}$ given by (3.22).

We note that it is sufficient that one overlap function, here $w_{11}(\mathbf{x}_T,z)$, has the symmetry properties discussed in the previous section, and thus the same arguments as in the case of elastic scattering can be applied. Therefore we can replace (3.16) by (3.23) for single diffractive dissociation as well.

The expression for the scattering amplitude is hence given by (2.52) with either the profile function (2.53) for the plane wave description or (2.54) for the oscillator description of X. In both cases the loop-loop correlation function evaluates to (3.23) for the matrix cumulant method or (3.17) for the expansion method.

Furthermore, when calculating cross sections with the description of X given by the oscillator method we can use analogous arguments. The simultaneous replacements $\mathbf{y}_T \to -\mathbf{y}_T$ and $z' \to 1-z'$ and subsequent integration over $\mathbf{y}_T$ and z' lead to the cancellation of contributions with odd m in (2.54) because of the existence of a factor $e^{im\theta_y}$ in $\tilde{X}^{n,m}(\mathbf{y}_T)$. Since for these functions odd m only occur for odd n, the sum over all excited states in the calculation of cross sections can be reduced to the sum over the wave functions with even n and the corresponding m's. Finally we point out that here the integration over the angle θ_b which we accomplish analogously to the case of elastic scattering by exploiting global azimuthal invariance leads to Bessel functions of m-th degree. This is due to the factor $e^{im\theta_y}$ in $X^{n,m}$ and relation (3.25).

3.3.3 Double diffractive excitation

We have seen in the previous sections that both in elastic and single diffractive dissociation we only get $C = P = +1$, i.e. pomeron, exchange and no $C = P = -1$, i.e. odderon, exchange in our model. This is, as we have seen, due to the symmetry of the hadron wave functions, where integration over all angles leads to a cancellation of those terms of the correlation function that are odd under C and P transformations. This result is not a unique feature of our model but is rather model independent. It relies on the fact that the quark-diquark density in a nucleon is nearly symmetric under a parity transformation if the diquark is sufficiently small, whereas the odderon coupling changes sign. To study odderon exchange in our model we have to find a reaction where the odderon contribution is not cancelled after integration due to the symmetry properties of the wave functions. This is possible in reactions, where initial state nucleons are transformed diffractively into excited negative parity states. In this case, even for point-like diquarks which we are using in our ansatz for the wave functions, the odderon couples to the nucleon without any restriction [36]. Three reactions which permit odderon exchange but exclude pomeron exchange have been suggested in high-energy photoproduction: exclusive neutral pseudoscalar meson production with nucleon break-up [31], $f_2(1270)$ and $a_2(1320)$ production with nucleon break-up [32], and the asymmetry in the fractional energy of charm versus anticharm jets, which is sensitive to odderon-pomeron interference [50].

Here we are going to study a hadronic reaction for which odderon exchange is allowed, namely

$$p + p \to N(1535) + N(1535). \tag{3.29}$$

In addition, the $N(1535)$ has a unique signature, being the only known baryon with a strong ηN decay [11]. One should note, however, that this decay provides some difficulty for standard models of baryon spectroscopy, including the quark-diquark model. It remains unclear why the $N(1535)$ decay has such a large branching ratio of about 30-55% into ηN whereas this decay is negligible for the $N(1520)$.

To construct the $\mathcal{T}$-matrix element of reaction (3.29) we start from (2.50), where the overlap functions w_{31}^{λ} and w_{42}^{λ} consist of one s-wave for the proton and one p-wave for the $N(1535)$ each. Now we are going to argue why it is sufficient to deal with spinless s- and p-waves as stated in section 3.2: as we are using scalar diquarks the spin of the proton and of the $N(1535)$ is carried by the quark in the according hadron. The spin conserving delta functions in (2.40)-(2.43) on the parton level then ensure that the spins of the proton and of the excited nucleon resonance are aligned parallel. As explained in section 3.2 we do not get any contributions from the states with helicity $\lambda = 0$ in our approximation. Since spin and angular momentum of the $N(1535)$ are antiparallel to each other in order to form a state with total angular momentum $J = 1/2$, we can infer directly that the helicity of the p-wave describing the $N(1535)$ is oriented antiparallel to the spin of the incoming proton. This means that from the originally 16 possible spin combinations of the 4 hadrons in initial and final state only 4 survive due to spin conservation on the parton level. For those we

immediately know which helicity state we have to assign to the $N(1535)$ in the final state. As we will calculate unpolarised cross sections in the following, i.e. we take the average over the initial state spins and sum over all final state spins, we have reduced the problem to the scattering of two initial state s-waves into two final state p-waves with fixed helicities, as already stated when discussing the wave functions. Moreover, looking at the expression for the p-wave (3.20), we note that on the level of cross sections the following relations hold

$$\begin{aligned} |\langle N_+(1535)\, N_+(1535)|\mathcal{T}|p\,p\rangle|^2 &= |\langle N_-(1535)\, N_-(1535)|\mathcal{T}|p\,p\rangle|^2\,, \\ |\langle N_+(1535)\, N_-(1535)|\mathcal{T}|p\,p\rangle|^2 &= |\langle N_-(1535)\, N_+(1535)|\mathcal{T}|p\,p\rangle|^2\,, \end{aligned} \tag{3.30}$$

where $\pm$ indicates the helicity $\lambda = \pm 1$ of the $N(1535)$. This means that only the relative orientation of the helicities of the two $N(1535)$ in the final state are of importance and thus we only have to calculate two scattering amplitudes, one where the helicities are aligned parallel, which we will call $\mathcal{T}_+$ and one where they are aligned antiparallel, which we will call $\mathcal{T}_-$.

Now we have to show that we indeed get $C = P = -1$ exchange for this type of reaction. The proof will rely on symmetry considerations, as in the case of elastic scattering and single diffractive dissociation before. To simplify our notation we define a reduced overlap function $\widetilde{w}_{kj}$ which does not contain any terms due to the angular dependence of the p-wave. Instead we explicitely write out this angular dependence in the following because it is crucial for our argumentation:

$$w^{\lambda}_{kj}(x_T, \theta_x, z) =: \lambda e^{i\lambda\theta_x}\, \widetilde{w}_{kj}(x_T, z). \tag{3.31}$$

With this definition and (3.24), (3.25) we obtain for the scattering amplitude

$$\mathcal{T}_\pm = 4\pi i s \int_0^\infty \mathrm{d}b_T\, b_T\, J_n(\sqrt{-t}\, b_T)\, \hat{J}_\pm(\mathbf{b}_T), \tag{3.32}$$

where $n = 2$ for $\mathcal{T}_+$ and $n = 0$ for $\mathcal{T}_-$. Here the profile function is given by

$$\hat{J}_\pm(\mathbf{b}_T) = \int \mathrm{d}^2x_T\, \mathrm{d}^2y_T\, \widetilde{w}_{31}(x_T, \tfrac{1}{2})\, \widetilde{w}_{42}(y_T, \tfrac{1}{2})\, \cos(\theta_x \pm \theta_y) \Big\{ \ldots \Big\}, \tag{3.33}$$

where $\{\ldots\}$ is an abbreviation for either (3.16) or (3.17). To obtain this result we have used the invariance of the correlation function under the simultaneous transformation of the variables $\theta_x \to -\theta_x$ and $\theta_y \to -\theta_y$. Now we consider the symmetry properties of the wave and correlation functions again. The argumentation is analogous to the case of elastic scattering with the crucial difference being the additional factor $\cos(\theta_x \pm \theta_y)$ here, which changes sign when we make the replacement $\mathbf{x}_T \to -\mathbf{x}_T$ or $\mathbf{y}_T \to -\mathbf{y}_T$, respectively. Due to this factor the integration over $\mathbf{x}_T$ or $\mathbf{y}_T$ now cancels the $\cos\chi$-terms of (3.16) instead of the $\sin\chi$-terms. Therefore, in the context of this scattering reaction, (3.16) reduces to

$$\langle \mathcal{W}_+ \mathcal{W}_- - \mathbb{1} \rangle_G \to i \left\{ -\frac{2}{3} \sin\left(\frac{1}{3}\chi\right) + \frac{1}{3} \sin\left(\frac{2}{3}\chi\right) \right\}. \tag{3.34}$$

On the other hand, the expression (3.17), which we get from the expansion method in the approximation up to $\mathcal{O}(\chi^2)$ discussed there, is even under $\chi \to -\chi$ and thus vanishes completely after integration over $\mathbf{x}_T$ or $\mathbf{y}_T$. To be able to use here as well a correlation function which has been evaluated in the expansion method, we have to include terms of higher order in χ. In [36, 51] the relevant term of order χ^3 has been calculated in the framework of the expansion method and the result is

$$\langle \mathcal{W}_+ \mathcal{W}_- - \mathbb{1} \rangle_G^{(3)} = i \left\{ -\frac{5}{4}\frac{1}{81}\, \chi(\mathbf{b}_T, \mathbf{x}_T, \mathbf{y}_T, z, z')^3 \right\}, \tag{3.35}$$

where we have attached an index (3) to denote that we are only discussing the third order term in χ here. Comparing this result with the $\mathcal{O}(\chi^3)$-term of the expansion of (3.16) we notice that the former is larger by a factor 5/4. This is a consequence of the truncation of the cumulant expansion at second order, due to which we neglect terms proportional to χ^3. Taking into account the 4- and 6-cumulant we recover (3.35) as the term of order χ^3 in an expansion [52].

To conclude, we note that for double diffractive excitation we have a purely imaginary contribution to the correlation function, either (3.34) for the matrix cumulant method or (3.35) for the expansion method, where we have to include the next, i.e. third, order in χ to get a non-zero contribution. Due to the symmetry of the wave and correlation functions we indeed get $C = P = -1$, i.e. odderon, exchange.

Finally we point out that also in the case of elastic scattering and single diffractive dissociation an imaginary part of the correlation function and $C = P = -1$ exchange terms both non-vanishing after integration with the overlap functions could arise from the inclusion of higher cumulant terms in (3.13). This could also be the case if we chose a more general description of the hadrons with different symmetries of the wave functions which are essential for the cancellations after integration. Of course, the analogue is true for double diffractive excitation, with the difference that these changes would lead to $C = P = +1$ exchange there.

Chapter 4

Hadron-hadron cross sections

The focus of this chapter will be on proton-proton scattering, where a lot of data is available in the energy range we are interested in, i.e. high centre of mass energy and small momentum transfer. First we will review elastic scattering, which has been calculated previously using the matrix cumulant method in [30]. Then the study will be extended to single diffractive dissociation. We will conclude the investigation of proton-proton scattering with the analysis of the reaction $pp \to N(1535)\,N(1535)$, i.e. double diffractive excitation of the proton. Then we will consider proton-pion scattering, i.e. we replace one of the incoming protons by a pion. In this context we are going to study elastic scattering and single diffractive dissociation of the pion.

To calculate cross sections for the reactions we are considering, we have to fix our free parameters, namely those of the MSV: G_2, a and κ; and those of the wave functions, the extension parameter S_{h_j} and the width of the longitudinal momentum distribution z_{h_j}. The set of MSV parameters used in this work has been established in [30] for the case of the matrix cumulant method giving (3.16). For the expansion method giving (3.17) the set of parameters depends on whether we discuss $C = P = +1$ exchange, for which we use the values given in [27], or $C = P = -1$ exchange. In order to obtain the latter contribution, a somewhat different approximation scheme was used in [36, 51] and therefore the resulting values are slightly modified. These three parameter sets are compiled in Table 4.1.

	matrix method	expansion method	
		$C = P = +1$	$C = P = -1$
G_2	$(529\ \text{MeV})^4$	$(501\ \text{MeV})^4$	$(525\ \text{MeV})^4$
a	0.32 fm	0.346 fm	0.31 fm
κ	0.74	0.74	0.74

Table 4.1: The parameters of the MSV for the matrix cumulant and the expansion method

The values given in Table 4.1 should be considered as effective values extracted from

fits to high energy scattering data using two different approximate formulae. Thus the differences between the values in the second and third (or fourth, respectively) column of the table can be taken as a theoretical error estimate. With fixed parameters the model gives energy independent cross sections. It has been shown in [24] that both the energy dependence of the cross section and of the slope parameter b of elastic scattering can be well described by energy dependent hadron extension parameters $S_{h_i}(s)$. In [30] it was found that in the framework of the matrix cumulant method energy dependent extension parameters can even describe the energy evolution of the whole differential elastic cross sections $\mathrm{d}\sigma/\mathrm{d}t$ up to $|t| \approx 1\,\mathrm{GeV}^2$. When using the matrix cumulant method we adopt the parametrisation from [30] for the extension parameter S_p of the proton

$$S_p(s) = 0.700 \left(\frac{s}{\mathrm{GeV}^2}\right)^{0.034} \text{ fm}. \tag{4.1}$$

This was obtained by fitting the total cross section as calculated from the optical theorem with the $\mathcal{T}$-matrix element calculated within the model

$$\sigma_{\mathrm{tot}} = \frac{1}{s}\mathrm{Im}(\mathcal{T}_{fi})\Big|_{t=0} \tag{4.2}$$

to the soft pomeron part of the Donnachie-Landshoff (DL) parametrisation for σ_{tot} [12]. For the expansion method we have established a similar connection between S_p and s:

$$S_p(s) = 0.624 \left(\frac{s}{\mathrm{GeV}^2}\right)^{0.028} \text{ fm}. \tag{4.3}$$

At $\sqrt{s} = 23.5$ GeV, for instance, we get $S_p = 0.868$ fm and $S_p = 0.745$ fm from (4.1) and (4.3), respectively. Since the MSV-parameters for $C = P = +1$ exchange in the expansion method are different from the ones used for the $C = P = -1$ exchange as stated above, of course the extension parameters differ as well. In the following we only need the extension parameter of the proton at $\sqrt{s} = 20$ GeV for the latter. To be consistent with the set of MSV-parameters, we use the value $S_p = 0.85\,\mathrm{fm}$ from [36, 51]. The width of the longitudinal momentum distribution of the proton has been chosen as $z_p = 0.4$ which gives a best fit to the isovector form factor of the proton calculated in the framework of our model (see chapter 5).

A different description of the energy dependence, motivated by the two pomeron picture has been suggested in [53]. In this approach the correlation function χ instead of the hadron extension parameters is assumed to depend on the energy. This is in line with other two component pictures as e.g. [54, 55]. Of course this leads to a different set of both MSV and wave function parameters. Since in this work also the correlation functions $\widetilde{D}, \widetilde{D}_1$ from (3.5) and the integration surface (see Fig. 3.1) are modified compared to our ansatz, we will not use this approach in the following.

After having fixed all parameters, the calculation of cross sections can be performed numerically. All phase space integrals and the integrals occurring in the

scattering amplitudes are evaluated using the Monte-Carlo integration subroutine VEGAS [56] in an adapted version [57].

4.1 Proton-proton scattering

From the experimental side a lot of data on proton-proton scattering exists over a wide range of energies. In particular the availability of data on soft diffractive scattering at high centre of mass energies makes proton-proton scattering an interesting field of application for our model.

4.1.1 Elastic scattering

Let us first consider elastic proton-proton scattering

$$p(P_1) + p(P_2) \to p(P_3) + p(P_4). \tag{4.4}$$

The differential cross section $\mathrm{d}\sigma_{\mathrm{el}}/\mathrm{d}t$ for this reaction has already been calculated using the functional integral approach and the matrix cumulant method in [30], however, as the results will be needed in the analysis of single diffractive dissociation, we give a short reminder of the results obtained there. Moreover we calculate the differential cross section using the expansion method and the integrated elastic cross section applying both methods and compare the results.

For $s \gg M_p^2$ the differential cross section is given by

$$\mathrm{d}\sigma_{\mathrm{el}} = \frac{1}{16\pi}\frac{1}{s^2}\left|\mathcal{T}_{fi}\right|^2 \mathrm{d}t, \tag{4.5}$$

where $\mathcal{T}_{fi}$ is our result (3.26) for the elastic scattering amplitude. Depending on which method for the evaluation of the correlation function is used, we insert (3.27) or (3.28), respectively.

In [27] it has been argued that the Gaussian shaped distribution of the longitudinal momentum fraction z (z') can be replaced by a delta-function centred at $z = 1/2$ ($z' = 1/2$), since the function χ (3.15), which determines the shape of the correlation function, depends only weakly on z (z'). A numerical investigation of the total cross section calculated from the optical theorem shows that the resulting difference for σ_{tot} is smaller than 1%. The profit one makes out of this simplification is a much shorter computation time in the numerical analysis, as each additional variable of integration means roughly a factor of 10 in the time needed to calculate the cross section. In the following we will make use of this simplification if not explicitly stated otherwise.

In Fig. 4.1 we compare the results from the matrix cumulant and expansion methods to experiment. The first method, i.e. using (3.23), gives a reasonable description of the data for $|t| \lesssim 1\,\mathrm{GeV}^2$ over many orders of magnitude but underestimates the

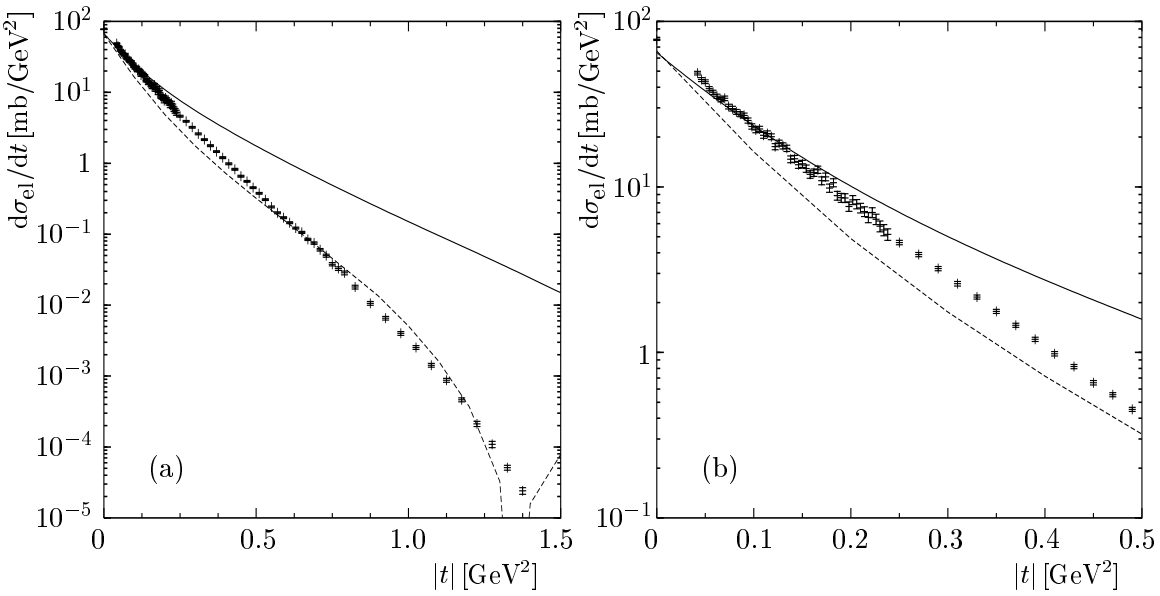

Figure 4.1: The differential elastic cross section $d\sigma_{el}/dt$ at $\sqrt{s} = 23.5$ GeV calculated using the matrix cumulant method (dashed line) and the expansion method (solid line) compared to the experimental data from [58]

data at small $|t|$. The expansion method, i.e. using (3.17), gives a better description of the data for $|t| \lesssim 0.2\,\mathrm{GeV}^2$ but overshoots the data by orders of magnitude for larger $|t|$. A fit of the form $d\sigma_{el}/dt = A \exp b\,t$ to the differential cross section gives $b = 13.8 \pm 0.4\,\mathrm{GeV}^{-2}$ for the matrix cumulant method and $b = 10.0 \pm 0.2\,\mathrm{GeV}^{-2}$ for the expansion method, respectively. From a fit to the experimental data [58] we obtain $b = 11.6 \pm 0.1\,\mathrm{GeV}^{-2}$. These fits have been performed within the range $0 \leq |t| \leq 0.2\,\mathrm{GeV}^2$, since the description of the data over a larger $|t|$-range would require an additional term $\propto t^2$ in the exponent of the fit. If we calculate the integrated elastic cross section at $\sqrt{s} = 23.5\,\mathrm{GeV}$, we obtain $\sigma_{el} = 5.0\,\mathrm{mb}$ in the matrix cumulant method and $\sigma_{el} = 7.3\,\mathrm{mb}$ in the expansion method compared to an experimental value of $\sigma_{el} = 6.81 \pm 0.19\,\mathrm{mb}$ [11]. The fact that the elastic cross section calculated by the expansion method is closer to the experimental value than the one from the matrix cumulant method is easily understood from Fig. 4.1b. In the integral over $d\sigma/dt$ only the region $|t| \lesssim 0.2\,\mathrm{GeV}^2$ contributes significantly and there the expansion method describes the data better. In the region $|t| \gtrsim 0.2\,\mathrm{GeV}^2$ the result from the expansion method is bigger than the experimental result, with the consequence that the resulting integrated cross section is too big.

In Fig. 4.2 we show σ_{el} for $10\ \mathrm{GeV} \leq \sqrt{s} \leq 10\ \mathrm{TeV}$. The data are as well from pp- as from $p\bar{p}$-experiments [11]. As our approach does not include, in Regge terminology, any non-leading trajectories, we cannot distinguish between these two reactions and they are described by the same scattering amplitude. The calculation agrees reasonably well with the experimental data. Due to the reasons discussed above, the integrated cross sections obtained from the matrix cumulant method are

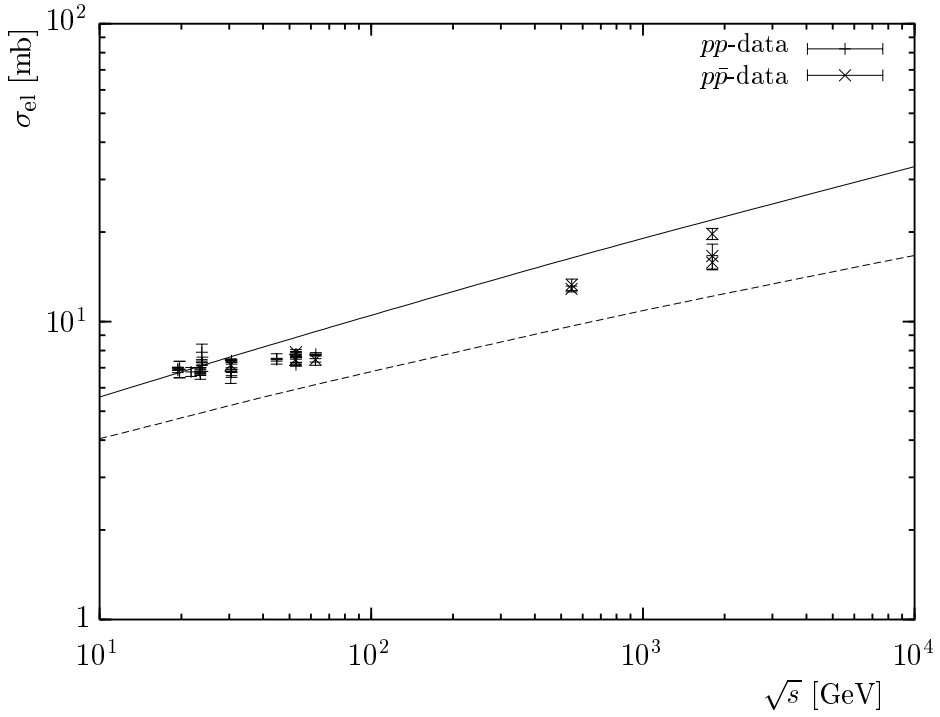

Figure 4.2: The integrated elastic cross section as a function of $\sqrt{s}$ calculated using the matrix cumulant method (dashed line) and the expansion method (solid line) compared to the experimental data from [11]

smaller than the experimental values. The difference we get from the two methods can thus be seen as a theoretical error estimate. The theoretical uncertainties have their origin in the different schemes which we use to evaluate the correlation function (3.10), which both of course make use of approximations, as has been discussed in section 3.1. In the case of the matrix cumulant expansion method the approximation is due to the truncation of the cumulant expansion after the second cumulant term, in the expansion method we expand directly in terms of the gluon field strengths. This means that both methods do not necessarily contain the same physical contributions when we compare the respective expressions order by order. We have already pointed out this fact when discussing the scattering amplitude for the $C = P = -1$ exchange in section 3.3.3, where we noted that we would have to include higher order cumulant contributions in the matrix cumulant method to obtain the same result in $\mathcal{O}(\chi^3)$ as in the expansion method.

4.1.2 Single diffractive dissociation

Now we turn to inelastic diffractive scattering

$$p(P_1) + p(P_2) \to p(P_3) + X(P_4). \tag{4.6}$$

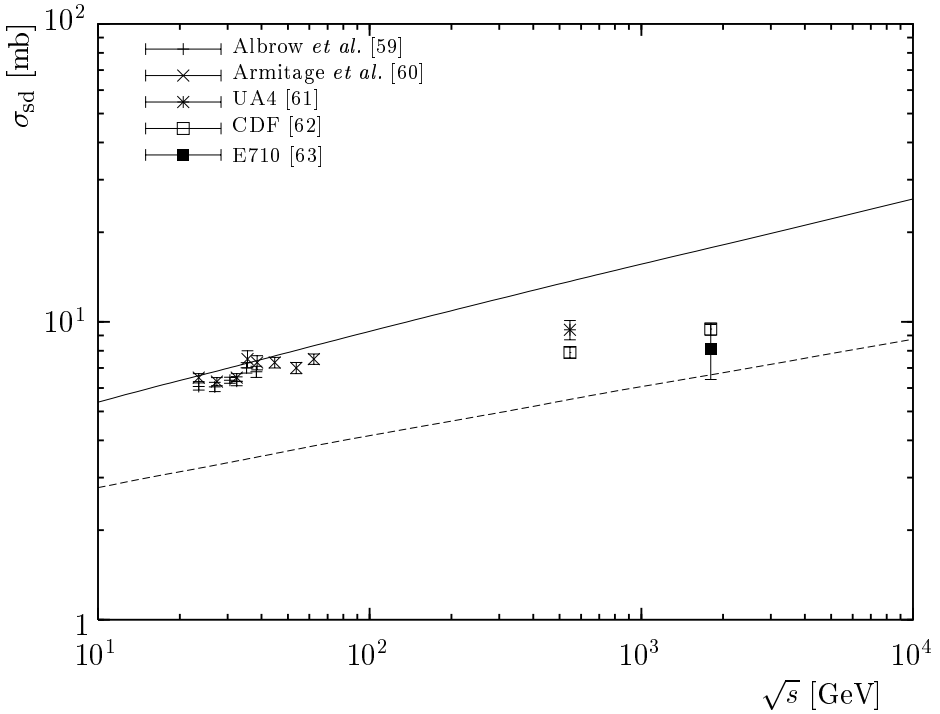

Figure 4.3: The integrated single diffractive dissociation cross section as a function of $\sqrt{s}$ calculated using the matrix cumulant method (dashed line) and the expansion method (solid line)

Using the plane wave method (2.52), (2.53) we calculate the differential diffractive cross section as

$$\mathrm{d}\sigma_{\rm diff} = (2\pi)^4 \frac{1}{2s} \left|\mathcal{T}_{fi}\right|^2 \mathrm{d}^5\mathcal{P}, \tag{4.7}$$

where

$$\mathrm{d}^5\mathcal{P} \;=\; \frac{1}{(2\pi)^9} \frac{1}{4sz'(1-z')} \mathrm{d}^2P_{4T} \mathrm{d}^2\Delta_{4T} \mathrm{d}z' \tag{4.8}$$

is the 5-dimensional phase space measure for the three particle final state formed by the first proton which remains intact and the quark and the diquark which describe the second, diffractively excited proton. As stated above the description of the diffractive final state X by a free quark-diquark pair also includes the case of elastic scattering. To obtain the cross section $\sigma_{\rm sd}$ for single diffractive dissociation, we have to subtract the elastic contribution and then multiply by 2 to account for the reaction where the first proton breaks up and the second stays intact. We find for the integrated single diffractive cross section as a function of $\sqrt{s}$ the result shown in Fig. 4.3. Comparing our results to experimental data, one has to keep in mind that the overall normalisation uncertainty of the experiments is of $\mathcal{O}(10\%)$. Furthermore the derivation of integrated cross sections from experimental data involves extrapolations of the measured data at given values of t and $\xi = M_X^2/s$ to

regions where no data exist. The extrapolations depend on assumptions on the shape of the t-distribution and the shape of the ξ-distribution. Different experiments make different assumptions and thus the resulting integrated cross sections differ from each other. The experimental values on the integrated single diffractive dissociation cross section quoted here use $\xi \leq 0.05$ as an upper bound in the mass distribution [59–61, 63], except for [62] where the range is extended to $\xi \leq 0.2$. In our calculation of $\sigma_{\rm sd}$ we integrate over all values of ξ. Because the mass spectrum obtained in our calculation decreases rapidly with increasing ξ (see Fig. 4.6), our numerical result of the integrated cross section is dominated by the low mass region and is not sensible to the integration range being $\xi \leq 0.05$ or $\xi \leq 0.2$. Again the difference between the cross sections obtained by the two methods can be understood as an estimation of the theoretical errors which arise due to the approximations made in the evaluation of the correlation function.

In Table 4.2 we give the ratio R of the single diffractive dissociation cross section to the sum of the single diffractive dissociation and the elastic cross sections from our model and from different experiments. For $\sqrt{s} = 546\,\text{GeV}$ and 1800 GeV we have used the values of $\sigma_{\rm el}$ and $\sigma_{\rm sd}$ as quoted by the UA4, CDF and E710 experiments. For the ISR energy range $20\,\text{GeV} \lesssim \sqrt{s} \lesssim 60\,\text{GeV}$ a lot of data exist. Since the cross sections do not vary much over this energy range, we have fitted both $\sigma_{\rm el}$ and $\sigma_{\rm sd}$ as being proportional to a small power of $\sqrt{s}$ and have then calculated R as a function of $\sqrt{s}$ using these fits. The quoted ISR R-value in Table 4.2 is evaluated at an intermediate energy of $\sqrt{s} = 38.5\,\text{GeV}$. As can be seen, our model, and

$\sqrt{s}$ [GeV]	$R = \sigma_{\rm sd}/(\sigma_{\rm el} + \sigma_{\rm sd})$				
	matrix	expansion	values calc. from exp.		
23.5	0.40	0.47			
38.5	0.39	0.47	0.49 ± 0.07	ISR	[59, 60]
62.3	0.39	0.46			
546	0.36	0.45	0.41 ± 0.02	UA4	[61]
			0.38 ± 0.01	CDF	[62]
1800	0.35	0.44	0.33 ± 0.05	E710	[63]
			0.32 ± 0.01	CDF	[62]

Table 4.2: The ratio R of the single diffractive dissociation to the sum of the single diffractive dissociation and elastic cross sections from the model and from experiments

more pronouncedly in the matrix cumulant method, predicts that the diffractive dissociation cross section grows more slowly with increasing energy than the elastic cross section. This is in qualitative agreement with experiment, where an even slower rise of $\sigma_{\rm sd}$ compared to $\sigma_{\rm el}$ is observed. The smaller R-values in the matrix cumulant

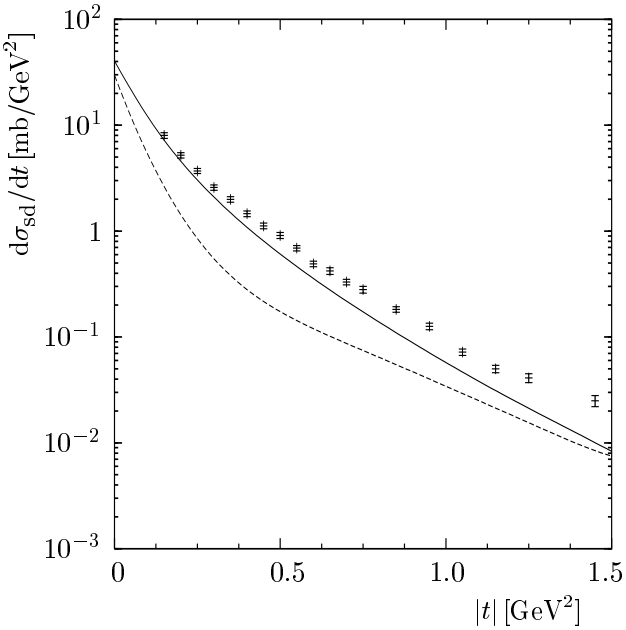

Figure 4.4: The differential diffractive cross section $d\sigma_{sd}/dt$ at $\sqrt{s} = 23.5$ GeV calculated using the matrix cumulant method (dashed line) and the expansion method (solid line) compared to the experimental data from [59]

method compared to the expansion method are mainly due to the relatively small integrated single diffractive dissociation cross sections in the former method.

The results for the differential cross section of the single diffractive dissociation are shown in Fig. 4.4. The curve calculated in the framework of the expansion method describes the slope of the diffractive reaction quite well even for larger values of $|t|$. Therefore the agreement with the experiment is reasonably good within the $|t|$-range considered here. This could however be partly accidental. In processes where the proton breaks up, the exchange of hard and semi-hard gluons will play an important role. This exchange is not described by our model which is an approximation for the infrared behaviour of QCD. We have seen in elastic scattering that the expansion method overestimates the cross section for values of $|t|$ larger than $0.2\,\mathrm{GeV}^2$, see Fig. 4.1, and this could simulate the expected contribution of hard or semi-hard gluon exchange in the diffractive dissociation reactions. We stress however that the fast decrease of the single diffractive dissociation cross section $d\sigma_{sd}/dt$ for $|t| \lesssim 0.2\,\mathrm{GeV}^2$ is a firm prediction of our model. Performing a fit over the range $0 \leq |t| \leq 0.2\,\mathrm{GeV}^2$ of the form $d\sigma_{sd}/dt = A \exp bt$ like in the case of elastic scattering we obtain $b = 12.6 \pm 0.2\,\mathrm{GeV}^{-2}$. For such small momentum transfer no experimental data on the differential diffractive cross section exist. To compare to experiment, we therefore apply the fit formula to both our result and the experimental data in the range $0.2\,\mathrm{GeV}^2 \leq |t| \leq 0.5\,\mathrm{GeV}^2$. For larger values of $|t|$ we would require an additional term $\propto t^2$ in the exponent of the fit. The

fits then give $b = 7.9 \pm 0.3\,\mathrm{GeV}^{-2}$ for our calculation in the expansion method and $b = 7.0 \pm 0.3\,\mathrm{GeV}^{-2}$ for the data from [59]. Integration of our result for the differential distribution over t leads to integrated single diffractive dissociation cross sections which are larger than the according experimental integrated cross sections.[1] Those are calculated from the experimental differential cross sections under the assumption of a linear extrapolation of the slope down to $t = 0\,\mathrm{GeV}^2$. Therefore it is the steep slope for $|t| \lesssim 0.2\,\mathrm{GeV}^2$ in our calculation that leads to larger integrated cross sections than experimentally observed even though in the whole range where experimental data on the differential t-distribution are available our calculation gives smaller values than the experiment [59]. Since our model predicts an increasingly steeper slope when we go to higher energies, this effect gets more pronounced for large values of $\sqrt{s}$. Therefore the agreement of our result for the integrated single diffractive dissociation cross sections is not as good for the Tevatron data as it is for the ISR data (see Fig. 4.3).

To check the validity of our description of the diffractive final state by a free quark-diquark pair using plane waves, now we apply the second method, which describes the diffractive final state X through a sum of wave functions of excited states of a two-dimensional harmonic oscillator, as explained above in section 2.3.2. In this description, the final state phase space is two-dimensional as in the case of elastic scattering and the differential cross section is given by

$$\frac{\mathrm{d}\sigma_{\mathrm{sd}}}{\mathrm{d}t} = \frac{1}{16\pi}\frac{1}{s^2}\sum_{(n,m)\neq(0,0)} |\mathcal{T}_{fi}|^2 \tag{4.9}$$

with $\mathcal{T}_{fi}$ from (2.54). The sum runs over all even n for the reasons given in section 3.3.2, the associated quantum number m runs over $m = -n, -(n-2), \ldots, n-2, n$. The numerical analysis shows that both calculations are in very good agreement to each other and that summing up the contributions from values of $n \leq 6$ already gives $\approx 98\%$ of the result using plane waves.

So far we have only discussed the result for the differential cross section which we obtain when we apply the expansion method. Fig. 4.4 also shows the result of our calculation in the framework of the matrix cumulant method. As already seen in elastic scattering, the result obtained from the matrix cumulant method is smaller than the one from the expansion method. The same fit we have used for the expansion method for the range $0 \leq |t| \leq 0.2\,\mathrm{GeV}^2$ here leads to $b = 19.1 \pm 0.9\,\mathrm{GeV}^{-2}$. This is in analogy to elastic scattering, where we have also found a steeper slope for very small momentum transfers when comparing matrix cumulant with expansion method. Repeating the fit in the range $0.2\,\mathrm{GeV}^2 \leq |t| \leq 0.5\,\mathrm{GeV}^2$ we obtain $b = 9.2 \pm 1.7\,\mathrm{GeV}^{-2}$. However, in the range $0.1\,\mathrm{GeV}^2 \lesssim |t| \lesssim 0.7\,\mathrm{GeV}^2$ the differential cross section develops a depression and in contrast to elastic scattering the

[1] Of course the physical region of t is bounded by t_{min}, which is a function of the mass of the diffractive final state and of $\sqrt{s}$, but in the kinematical region which we are studying we have $t_{\mathrm{min}} \lesssim 10^{-3}$ and thus t_{min} can be safely set to 0.

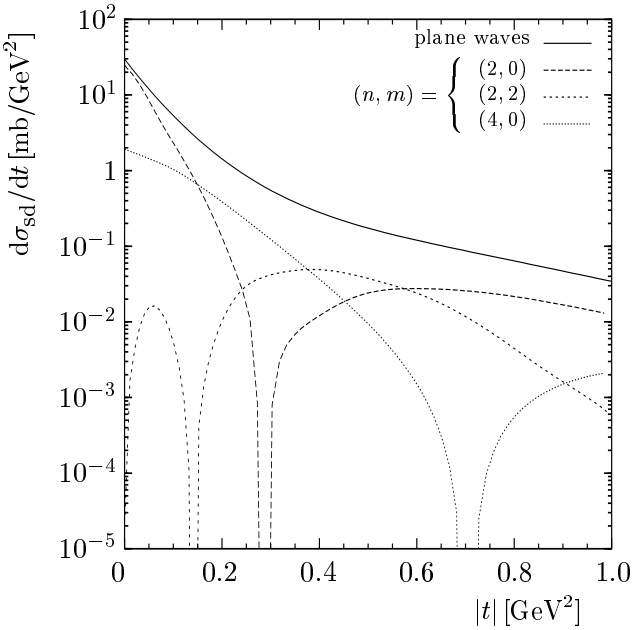

Figure 4.5: The contributions of harmonic oscillator wave functions with fixed quantum numbers n, m to the differential diffractive cross section $\mathrm{d}\sigma_{\mathrm{sd}}/\mathrm{d}t$ compared to the result obtained by the plane wave description (solid line) of the diffractive final state X

matrix cumulant method fails to describe the shape of the differential cross section. This depression is the reason why, after integration over t, the integrated single diffractive dissociation cross sections in the matrix cumulant method are noticeably smaller than the ones extracted from the expansion method and experimental data.

To understand where this depression comes from, we again apply the second method and describe the diffractive final state through the sum of the wave functions $X^{n,m}$. Progressing analogously to the above study of the expansion method we sum up all contributions with $n \leq 6$ and associated m's and find as well very good agreement to the plane wave description. This shows us that both descriptions of X indeed are equivalent to each other. Now we take a closer look at the contributions to the differential diffractive cross section from excited state wave functions $X^{n,m}$ with definite values of n and m. The reason why we can compare the contributions from wave functions with definite quantum numbers directly to each other and to the plane wave description is that due to orthogonality they add up on the level of the cross section and not on the level of the scattering amplitudes. We have already used this fact in (4.9). Therefore we can calculate differential diffractive cross sections with the sum over n, m replaced by just one term with fixed quantum numbers. Some of these contributions to the differential cross section are shown in Fig. 4.5, where we have also included the result obtained by the plane wave description for comparison. We see that, like for elastic scattering as discussed in [30],

various contributions to the differential cross sections develop a "dip"-structure, in particular those with $m = 0$. The location of these dips is given by the $|t|$-value at which the real part of the correlation function changes sign. At which exact value for $t < 0$ this happens is governed by the details of the interplay of the Bessel function J_m that occurs in the scattering amplitude (see (3.25) and section 3.3.2), the wave function $X^{n,m}$ and the correlation function. We note that for increasing quantum number n the position of the dip moves to larger values of $|t|$. As the imaginary part of the correlation function is cancelled after integration over the wave functions as discussed above, the scattering amplitude is zero at these positions and therefore we get an infinitely deep dip. As can be seen from Fig. 4.5 several dips develop in the region $0.1\,\mathrm{GeV}^2 \leq |t| \leq 0.7\,\mathrm{GeV}^2$ for wave functions with $n \leq 6$. In particular the contribution with the quantum numbers $n = 2, m = 0$ which accounts for the main part in the sum has a dip at $|t| \approx 0.3\,\mathrm{GeV}^2$. Performing the sum over n, m then leads to the formation of the depression for this region of $|t|$. We expect the dips - and in consequence the depression - to be at least partly filled up when we include higher cumulant terms, which could lead to an imaginary part of the correlation function non-vanishing after integration with the wave functions as discussed in more detail in section 3.3. Also the description of the proton by a more general quark configuration than the simple quark-diquark picture we have used here changes the symmetries of the wave functions which are essential for the cancellation of the imaginary part of the correlation function. The result would be a refined description of the differential diffractive cross section in the matrix cumulant method and therefore, after integration over t, also a larger integrated single diffractive dissociation cross sections which would be in better accord with experiment.

In the following we will consider the mass spectrum $\mathrm{d}^2\sigma_{\mathrm{sd}}/(\mathrm{d}\xi \mathrm{d}t)$ of the single diffractive dissociation reaction at $\sqrt{s} = 23.5$ GeV for $t = -0.0525\ \mathrm{GeV}^2$, where ξ is the squared mass of the diffractive final state divided by s. In our ansatz with plane wave final states, ξ then is given by

$$\xi := \frac{M_X^2}{s} = \frac{\boldsymbol{\Delta}_{4T}^2 + (1-z')m_q^2 + z' m_{\bar{q}}^2}{z'(1-z')s}. \tag{4.10}$$

Here m_q and $m_{\bar{q}}$ are the masses of the quark and the diquark which describe the excited proton state. To take thresholds into account the mass for the quark has been chosen to be 330 MeV and for the diquark 660 MeV so that the sum roughly gives the proton mass. Going back to (2.53) we recognise that now we can no longer replace the Gaussian shaped longitudinal momentum distribution in the wave function (3.18) for the hadron h_2, which breaks up, by a delta function centred around 1/2, as we have done in the calculations before, because z' determines the value of ξ in (4.10). This was different for the calculation of $\mathrm{d}\sigma_{\mathrm{sd}}/\mathrm{d}t$, where we performed an integration over the full range of $\boldsymbol{\Delta}_{4T}$ in phase space and were not interested in any particular value of ξ. As a consequence of the introduction of quark masses the integration over z' now does not run from 0 to 1, but the integration

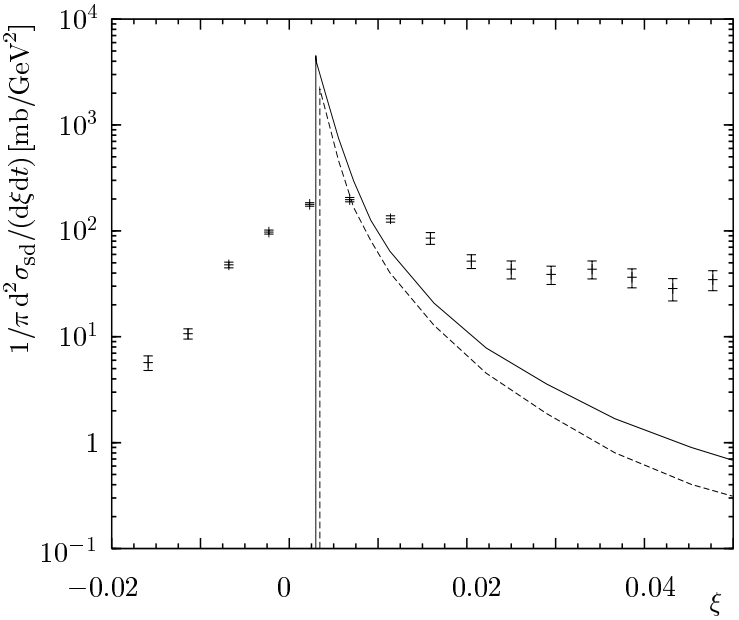

Figure 4.6: The diffractive mass spectrum $\mathrm{d}^2\sigma_{\mathrm{sd}}/(\mathrm{d}\xi \mathrm{d}t)$ for $t = -0.0525$ GeV^2 at $\sqrt{s} = 23.5$ GeV calculated using the matrix cumulant method (dashed line) and the expansion method (solid line) together with the data from [60]

limits are given by

$$z'_{0/1} = \frac{1}{2} - \frac{m_q^2 - m_{\bar{q}}^2}{2\xi s} \mp \sqrt{\frac{1}{4} - \frac{m_q^2 + m_{\bar{q}}^2}{2\xi s} + \left(\frac{m_q^2 - m_{\bar{q}}^2}{2\xi s}\right)^2}\,. \tag{4.11}$$

This ensures that the mass spectrum starts at $M_X^2 = M_p^2$ where M_p is the proton mass. Our plane wave description of the diffractive final state of course also includes elastic scattering. To compare with experimental results on diffractive dissociation we have to subtract the elastic contribution. To do so we argue as follows: to obtain the elastic contribution, we integrate $\mathrm{d}^2\sigma_{\mathrm{sd}}/(\mathrm{d}\xi \mathrm{d}t)$ over ξ from $\xi_0 = M_p^2/s$ up to ξ_1. We determine ξ_1 in such a way that the integral gives the value of the elastic differential cross section $\mathrm{d}\sigma_{\mathrm{el}}/\mathrm{d}t$. Now we interprete the mass spectrum as consisting of the elastic part, which lies between ξ_0 and ξ_1 and the dissociation part, which starts at ξ_1. This procedure allows us to separate the elastic and the dissociation contributions.

The result of the calculation is shown in Fig. 4.6 for $t = -0.0525\,\mathrm{GeV}^2$ and the c.m. energy $\sqrt{s} = 23.5$ GeV together with the data points from [60]. For the matrix cumulant method we determine $\xi_1 = 1.90\,\mathrm{GeV}^2/s \approx 3.44 \cdot 10^{-3}$, for the expansion method $\xi_1 = 1.63\,\mathrm{GeV}^2/s \approx 2.95 \cdot 10^{-3}$. Again the differential distribution obtained by our calculation in the matrix cumulant method is smaller than the one corresponding to the expansion method and starts for slightly larger ξ_1. This is

not surprising because integrating $\mathrm{d}^2\sigma_{\mathrm{sd}}/(\mathrm{d}\xi \mathrm{d}t)$ over ξ from ξ_1 to $\xi_2 = \infty$, following the argumentation from above, we have to find the value for the differential single dissociative cross section $\mathrm{d}\sigma_{\mathrm{sd}}/\mathrm{d}t$ at $t = -0.0525\,\mathrm{GeV}^2$. [2] As we have seen above, this differential cross section is smaller for all values of t in the matrix cumulant method than in the expansion method and therefore the double differential cross section also has to be smaller when calculated by means of the former method. The comparison with the experimental data proves difficult, as the experimental values are smeared out over a certain range of values for ξ because of the detector mass resolution function. This explains also the data for the unphysical negative ξ-values. As a consequence the large peak of the diffractive mass spectrum is much more pronounced in our calculation and the experimental distribution is flatter around that peak. To compare directly with the experiment, we would have to fold our results with the mass resolution function of the detector used in the experiments [60], but unfortunately, this resolution function can no longer be reconstructed [64]. We note that our model should give reliable results for small ξ. Indeed, for large values of ξ the model seems to underestimate the data considerably. But for this ξ region we expect, for instance, that our purely nonperturbative treatment of the scattering must be supplemented by hard gluon radiation which should lead to high invariant masses for the diffractively excited state. Furthermore our calculation treats the final state as a quark-diquark pair and therefore no confinement effects are included here.

4.1.3 Double diffractive excitation

Now we will study the double diffractive excitation of the proton

$$p(P_1) + p(P_2) \to N(1535)(P_3) + N(1535)(P_4), \tag{4.12}$$

where the $N(1535)$ is an excited nucleon resonance with mass $M_* = 1535\,\mathrm{MeV}$ and the quantum numbers $I(J^P) = \frac{1}{2}(\frac{1}{2}^-)$. In the quark-diquark picture it has angular momentum $L = 1$. The differential cross section is given by

$$\mathrm{d}\sigma_{\mathrm{dd}} = \frac{1}{32\pi}\frac{1}{s^2}\left(|\mathcal{T}_+|^2 + |\mathcal{T}_-|^2\right)\mathrm{d}t, \tag{4.13}$$

with $\mathcal{T}_\pm$ from (3.32). The scattering amplitudes contain the double diffractive profile function $\hat{J}_\pm$, which depends explicitely on the relative orientation of the helicities of the two excited nucleon resonances (see (3.33)). Depending on which method we want to use, we use either (3.34) or (3.35) to evaluate the correlation function.

Unfortunately no experimental data exist on this reaction so far, so we can only give predictions for future experiments. RHIC for example meets all the requirements to investigate this reaction. As we mentioned in section 3.3.3 this reaction

[2] In practice it is sufficient to perform the integral for a finite value of $\xi_2 \approx 25\,\mathrm{GeV}^2/s$ because of the fast decrease of the calculated differential distribution for large values of ξ.

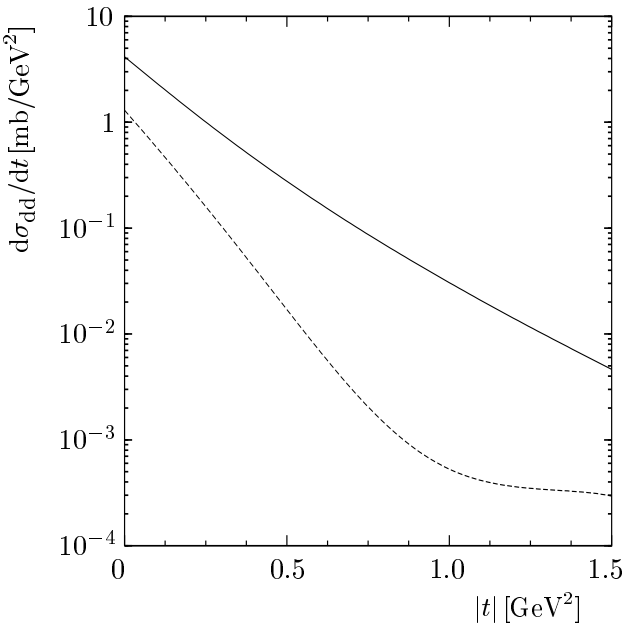

Figure 4.7: The differential diffractive cross section $d\sigma_{dd}/dt$ at $\sqrt{s} = 20$ GeV calculated using the matrix cumulant method (dashed line) and the expansion method (solid line)

has an unique signature since the $N(1535)$ is the only known baryon with a strong ηN decay. A clear signal in the detector for this reaction thus would be a final state composed of 2 η's and 2 nucleons. However, there is also the question open why the $N(1535)$ has a strong decay mode into ηN whereas the $N(1520)$, which has the same quantum numbers apart from $J = \frac{3}{2}$ instead of $J = \frac{1}{2}$, has not [11]. Standard models of baryon spectroscopy, including the quark-diquark model we use here, have difficulties explaining this experimentally well founded fact. We have to keep this in mind as a possible source of theoretical uncertainties in our model when discussing our results.

The differential cross section $d\sigma_{dd}/dt$ calculated in the framework of both methods is shown in Fig. 4.7. These distributions exhibit some qualitative features that we have already discussed in section 4.1.2 when investigating single diffractive dissociation. One similarity is that again the result obtained by the matrix cumulant method is smaller compared to the one calculated with the expansion method. Going back to the discussion following (3.35) we recall that the two methods rely on different approximation schemes that do not necessarily include the same contributions at every order of χ. We have seen for example that the term of $\mathcal{O}(\chi^3)$ in the expression for the correlation function is larger by a factor $\frac{5}{4}$ in the expansion method compared to the matrix cumulant method with truncation after the second cumulant. To see where the difference between the methods comes from we expand (3.34) to order χ^3 giving $-i\frac{1}{81}\chi^3$ and calculate the differential cross section.

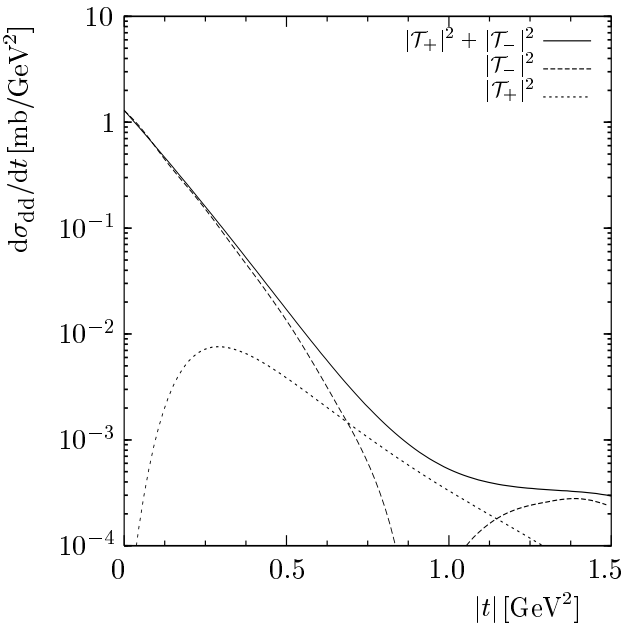

Figure 4.8: The contribution of $\mathcal{T}_+$ and $\mathcal{T}_-$ to the differential cross section $\mathrm{d}\sigma_{\mathrm{dd}}/\mathrm{d}t$ compared to the full result (solid line)

Naively we would expect the distribution obtained that way to be smaller by a factor $(\frac{4}{5})^2$ than the expansion method result for the reason given above. However, we have to remember that the MSV parameters are different for the two methods and in fact the distribution calculated with the expanded matrix cumulant result and the original matrix cumulant parameters (second column of Table 4.1) is slightly larger than the one calculated with the expansion method and the according parameters (fourth column of Table 4.1). This is mainly due to the fact that the correlation length enters the cross section to power a^{24}. Including step by step higher orders in χ we finally get back to the result for the matrix cumulant method shown in Fig. 4.7. By this argument we see that the contributions from higher orders in χ have an essential influence on both the normalisation and the shape of the differential cross section. For elastic scattering and for single diffractive dissociation, where we have $C = P = +1$ exchange instead of the $C = P = -1$ exchange we are discussing here, these arguments also hold true. In all cases we start from (3.16) for the matrix cumulant method and depending on the symmetries of the wave and correlation functions we keep either (3.23) or (3.34) after integration with the overlap functions. Expanding these expressions and calculating the contributions from increasingly higher orders in χ we see that also for $C = P = +1$ exchange they are crucial for the normalisation and the shape of the cross section. In particular the position of the the dip structure seen in the differential distribution of elastic scattering and the depression in the differential cross section of single diffractive dissociation depend on how many orders in χ we take into account.

Another agreement with single diffractive dissociation is the development of a depression in the differential distribution calculated with the matrix cumulant method (compare Figs. 4.4 and 4.7). In analogy to section 4.1.2, where we have analysed the origin of the depression by studying contributions of single oscillator functions to the cross section, we now calculate the cross section from either $\mathcal{T}_+$ or $\mathcal{T}_-$ alone instead of immediately summing up both contributions. The respective results are shown in Fig. 4.8. Again we find that the reason for the depression is the location of a dip at $|t| \approx 1.0\,\mathrm{GeV}^2$ in the leading term of the sum, namely the one we get from $\mathcal{T}_-$.[3] As already mentioned in section 4.1.2, the inclusion of higher cumulants and a refined model for both the proton and the excited nucleon state could lead to an improved description of the differential cross section.

Compared to elastic scattering or single diffractive dissociation we note that the differential distribution for small values of $|t|$ is relatively flat. A fit to $\mathrm{d}\sigma_{\mathrm{dd}}/\mathrm{d}t = A \exp b\,t$ gives $b = 8.2 \pm 0.1\,\mathrm{GeV}^{-2}$ for the matrix cumulant and $b = 5.7 \pm 0.1\,\mathrm{GeV}^{-2}$ for the expansion method. Our predictions for the integrated cross section for the reaction $pp \to N(1535)N(1535)$ are $\sigma_{dd} = 0.2\,\mathrm{mb}$ when applying the matrix cumulant and $\sigma_{dd} = 0.7\,\mathrm{mb}$ when applying the expansion method. These cross sections are solely due to $C = P = -1$, i.e. odderon, exchange. In the approximation we use here, an a priori possible contribution through pomeron exchange is strictly zero. This is in agreement with the Gribov-Morrison rule [65], but as neither this rule nor our model are exact the possibility cannot be ruled out entirely. However, this can be tested experimentally. As the odderon is known to couple at most very weakly to the nucleon it will not contribute significantly to the reaction $p\,p \to p\,N(1535)$. So if this reaction is observed at high energy, the natural interpretation is that it is due to pomeron exchange and, using reggeon factorisation together with pp elastic scattering, allows the pomeron contribution to $p\,p \to N(1535)\,N(1535)$ to be obtained.

To conclude this section we note that a possible check of our results could be obtained by calculating the electromagnetic $p - N(1535)$ transition form factor. However, in the formulation of the model used here, in particular due to the application of the quark-diquark picture with scalar diquarks, this calculation is not feasible. We will come back to this point when discussing the calculation of form factors in the framework of our model.

4.2 Proton-pion scattering

We present calculations for the reaction $p\,\pi^{\pm} \to p\,\pi$ and $p\,\pi^{\pm} \to p\,X$, respectively. Of course, the vacuum parameters G_2, a, κ stay the same but we still have to fix the pion extension parameters S_π and z_π in (3.18). Proceeding as in the case of proton-proton scattering we find for the parameters $S_\pi = 0.60\,\mathrm{fm}$ for the matrix cumulant

[3] Of course it is not the leading term in the region of the dip, where its contribution tends to zero.

and $S_\pi = 0.55\,\mathrm{fm}$ for the expansion method, respectively, at $\sqrt{s} = 19.5$ GeV. In both methods we obtain the same value $z_\pi = 0.5$ for the width of the longitudinal momentum distribution.

4.2.1 Elastic scattering

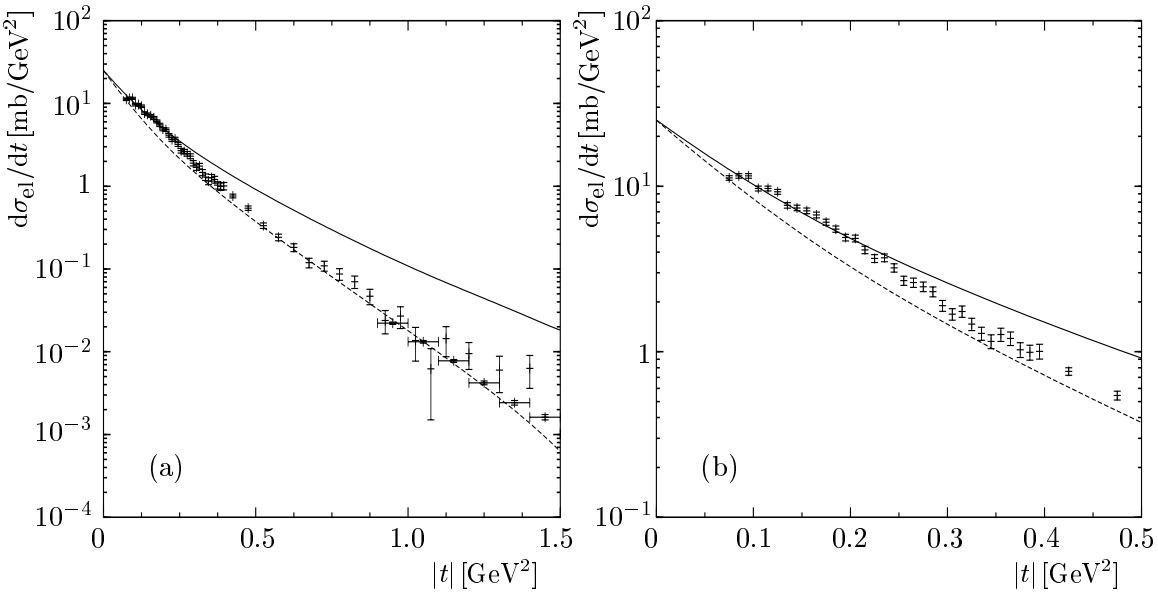

Figure 4.9: The differential elastic cross section $d\sigma_{el}/dt$ at $\sqrt{s} = 19.5$ GeV calculated using the matrix cumulant method (dashed line) and the expansion method (solid line) compared to the experimental data from [67]

Again we will first take a look at elastic scattering. For a c.m. energy of $\sqrt{s} = 19.5$ GeV we find for the integrated elastic cross sections $\sigma_{el} = 2.4\,\mathrm{mb}$ with the matrix cumulant and $\sigma_{el} = 3.1\,\mathrm{mb}$ with the expansion method, compared to an experimental value of $\sigma_{el} = 3.30 \pm 0.11\,\mathrm{mb}$ [66]. The differential elastic cross section is shown in Fig. 4.9. The matrix cumulant method describes the differential distribution reasonably well over many orders of magnitude and underestimates the data for small $|t|$. This is the reason why the integrated cross section comes out too small when applying the matrix cumulant method. The expansion method gives a better description of the data for $|t| \lesssim 0.2\,\mathrm{GeV}^2$ but overestimates the data for larger values of $|t|$, and therefore the integrated cross section as well. All this is in complete analogy to elastic proton-proton scattering. Fitting our result for the differential cross section by $d\sigma_{el}/dt = A \exp b\,t$ we find $b = 10.9 \pm 0.3\,\mathrm{GeV}^2$ for the matrix cumulant method and $b = 8.7 \pm 0.3\,\mathrm{GeV}^{-2}$ for the expansion method. The experimentally measured values are $b = 7.9 \pm 0.2\,\mathrm{GeV}^{-2}$ for π^+p- and $b = 8.4 \pm 0.1\,\mathrm{GeV}^{-2}$ for π^-p-scattering, respectively [67]. We cannot distinguish between these two reactions and describe them by the same scattering amplitude because our model does not include, in Regge terminology, any non-leading trajectories.

4.2.2 Single diffractive dissociation

Moving on to the reaction where the pion breaks up diffractively, we calculate σ_{sd} and the R-value, which we define as in the case of proton-proton scattering. For the matrix cumulant method we find $\sigma_{\mathrm{sd}} = 1.1\,\mathrm{mb}$ and $R = 0.32$, for the expansion method $\sigma_{\mathrm{sd}} = 2.0\,\mathrm{mb}$ and $R = 0.39$. The according experimental values are $\sigma_{\mathrm{sd}} = 1.90 \pm 0.2\,\mathrm{mb}$ and $R = 0.37 \pm 0.03$ [68] which is in quite good agreement to the results obtained from the expansion method. Differential cross section for proton-pion scattering with diffractive break up of the pion are unfortunately not available at c.m. energies which are high enough for our model to be applicable.

Chapter 5

Space-like form factors in the model

In this chapter we will study form factors within our model. We do not intend to perform a precision calculation of form factors but we will apply the calculation to extract values for the width of the longitudinal momentum distributions of the proton and the pion, z_p and z_π, respectively, by fitting our results to experimental data.

5.1 The electromagnetic form factors of the proton

The coupling of the electromagnetic current to the proton can be described by

$$\langle p(P',s')|j^\mu(0)|p(P,s)\rangle = e\,\bar{u}_{s'}(P')\left[\gamma^\mu F_{1p}(Q^2) + \frac{i\sigma^{\mu\nu}q_\nu}{2M_p}F_{2p}(Q^2)\right]u_s(P), \qquad (5.1)$$

where the momentum transfer is $q = P' - P$, $Q^2 = -q^2$, M_p is the proton mass, $e = \sqrt{4\pi\alpha_{\text{e.m.}}}$ and F_{1p}, F_{2p} are the Dirac and Pauli form factor of the proton, respectively. Now we choose such a coordinate system so that q is purely transverse:

$$\begin{aligned}
P^\mu &= \frac{1}{2}P_+ n_+^\mu + \frac{1}{2}P_- n_-^\mu - \frac{1}{2}q^\mu, \\
P'^\mu &= \frac{1}{2}P_+ n_+^\mu + \frac{1}{2}P_- n_-^\mu + \frac{1}{2}q^\mu, \\
q &= \begin{pmatrix} 0 \\ \mathbf{q}_T \\ 0 \end{pmatrix}, \qquad n_\pm = \begin{pmatrix} 1 \\ 0 \\ 0 \\ \pm 1 \end{pmatrix}, \\
P_- &= (\frac{1}{4}\mathbf{q}_T^2 + M_p^2)/P_+. \qquad (5.2)
\end{aligned}$$

In the high energy limit, $P_+ \to \infty$, we get for the matrix element (5.1) (see [69])

$$\langle p(P',s')|j^\mu(0)|p(P,s)\rangle = e\,P_+ n_+^\mu\,\chi_{s'}^\dagger\left[F_{1p}(Q^2) - \frac{\sigma^3 \mathbf{q}_T\cdot\boldsymbol{\sigma}}{2M_p}F_{2p}(Q^2)\right]\chi_s + \mathcal{O}(1), \quad (5.3)$$

where $\chi_s, \chi_{s'}$ are the Pauli two-component spinors. F_{1p} multiplies the spin-non-flip part, F_{2p} the spin-flip part of the matrix element. Calculating the spin average of this expression leads to

$$\frac{1}{2}\sum_s \langle p(P',s)|j^\mu(x)|p(P,s)\rangle = e\,P_+ n_+^\mu F_{1p}(Q^2) + \mathcal{O}(1). \quad (5.4)$$

We describe the calculation of the Dirac form factor of the proton in the framework of our model in appendix C. In the following we consider the matrix element of the third component of the isospin current j_3^μ. Its matrix element between proton states is as in (5.1),(5.3), with F_{ip} replaced by F_{iv}, related to the form factors of proton and neutron by

$$F_{iv} = \frac{1}{2}\left(F_{ip}(Q^2) - F_{in}(Q^2)\right) \qquad (i=1,2). \quad (5.5)$$

With the wave functions (3.18) we obtain

$$F_{1v}(Q^2) \;=\; \frac{1}{2I_p}\int_0^1 \mathrm{d}z\, 2z(1-z)\, e^{-(z-\frac{1}{2})^2/2z_p^2}\, e^{-\frac{z^2}{2}S_p^2Q^2}, \quad (5.6)$$

where I_p is the normalisation factor (3.19). For this calculation we need only the expectation value of one Wegner-Wilson loop. A straightforward calculation shows that the expectation value over one single loop is 1 in both the matrix cumulant method and the expansion method. Thus, in our model the form factor is just the Fourier transform of the squared wave function.

We will now use (5.6) to determine z_p and S_p. It turns out that in the range $0 \le Q \le 0.5\,\mathrm{GeV}$ the form factor depends sensitively on S_p but only weakly on z_p. From a fit to experiment in this region we obtain $S_p = 0.77\,\mathrm{fm}$. With S_p fixed to this value we show in Fig. 5.1 our result (5.6) for F_{1v} for different values of z_p. The experimental values have been calculated from the experimental data for G_{Ep} and G_{Mp} from [70, 71] and a fit of the experimental data on G_{En} and G_{Mn} [72] according to (5.5) and the relation between the Dirac ($F_{1p,n}$) and the electric ($G_{Ep,n}$) and magnetic ($G_{Mp,n}$) form factor of the proton and neutron, respectively:

$$F_{1N}(Q^2) = \frac{G_{EN}(Q^2) + \tau G_{MN}(Q^2)}{1+\tau}, \qquad \tau = \frac{Q^2}{4M_N^2} \qquad (N = p,n). \quad (5.7)$$

The best fit is found for $z_p = 0.4$. As can be seen from Fig. 5.1, z_p, which fixes the width of the longitudinal momentum distribution of the constituents, plays no important role for $Q \lesssim 0.5\,\mathrm{GeV}$. For larger values of Q however, our fit is

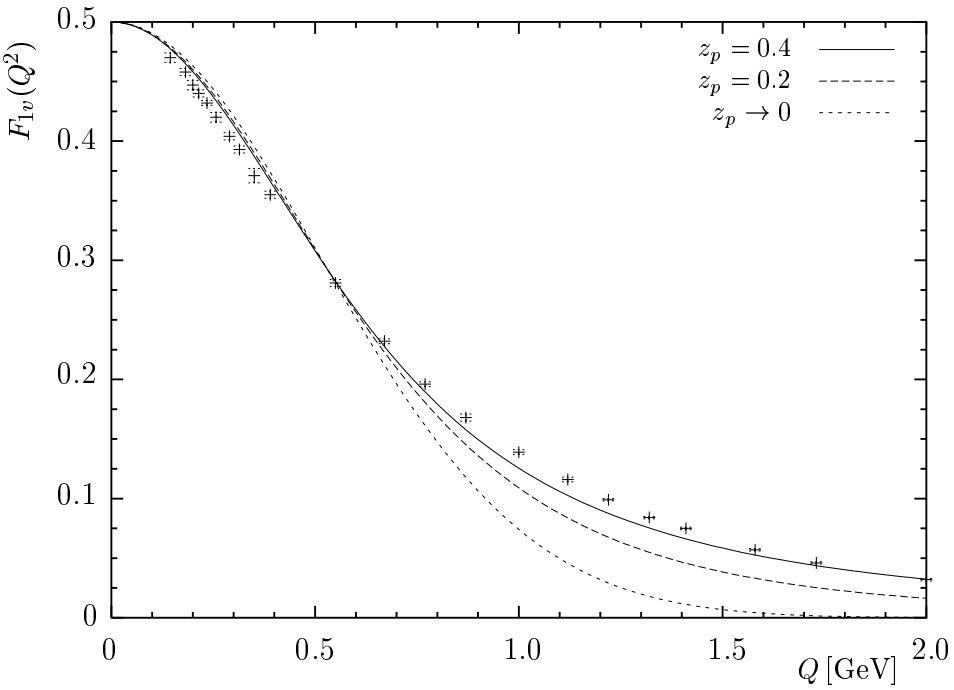

Figure 5.1: The isovector form factor of the proton for $S_p = 0.77\,\mathrm{fm}$ and different values of z_p compared to the experimental data from [70–72]

substantially improved when using a Gaussian shaped z-dependence instead of a delta-function centred around $z = 1/2$, which is equivalent to $z_p \to 0$.

It has to be noted that the proton extension parameter S_p obtained from (5.6) is not, and need not be, the same as the one used in the hadronic scattering processes in the previous chapters. Whereas the hadronic extension parameter has been allowed to be energy dependent (see (4.1),(4.3)) to account for the rise of σ_{tot} with $\sqrt{s}$, the extension parameter connected with the form factor has a fixed value for all energies as the form factor itself is energy independent and is related to the electromagnetic radius of the proton as follows. Using the definitions

$$\begin{aligned} \langle r^2 \rangle^p &= -6\, \frac{\mathrm{d}G_{Ep}(Q^2)}{\mathrm{d}Q^2}\bigg|_{Q^2=0}, \\ r^p_{\mathrm{em}} &= \sqrt{\langle r^2 \rangle^p}, \end{aligned} \tag{5.8}$$

relations (5.5),(5.7) and the experimental value

$$\frac{\mathrm{d}G_{En}(Q^2)}{\mathrm{d}Q^2}\bigg|_{Q^2=0} = 0.019\,\mathrm{fm}^2 \tag{5.9}$$

from thermal-neutron-electron scattering [73], we get from our model

$$r^p_{\mathrm{em}} = 0.81\,\mathrm{fm}. \tag{5.10}$$

This coincides with the value one obtains for the proton electromagnetic radius when describing the electric form factor of the proton by the dipole parametrisation [70], which also results in $r^p_{\rm em} = 0.81\,\text{fm}$. From scattering experiments one finds $r^p_{\rm em} = 0.88 \pm 0.03\,\text{fm}$ or $r^p_{\rm em} = 0.92 \pm 0.03\,\text{fm}$, depending on which fit is used for the experimental data on $G_{Ep}(Q^2)$ for small Q^2 [70]. The Lamb shift measurements [74] give $r^p_{\rm em} = 0.890 \pm 0.014\,\text{fm}$. Thus our result (5.10), as well as the one calculated from the dipole parametrisation, is smaller than the experimental value for $r^p_{\rm em}$. Our calculation as well as the dipole fit describe the data [71] for G_{Ep} rather well for $Q \gtrsim 0.4\,\text{GeV}$. But for smaller Q the data [70] indicate a rapid change in the slope $\mathrm{d}G_{Ep}(Q^2)/\mathrm{d}Q^2$ which is described neither by our model nor by the dipole parametrisation. Such an "anomalous" behaviour of G_{Ep} and G_{En} for small Q^2 has been related to QCD vacuum effects in [75].

5.2 The electromagnetic form factor of the pion

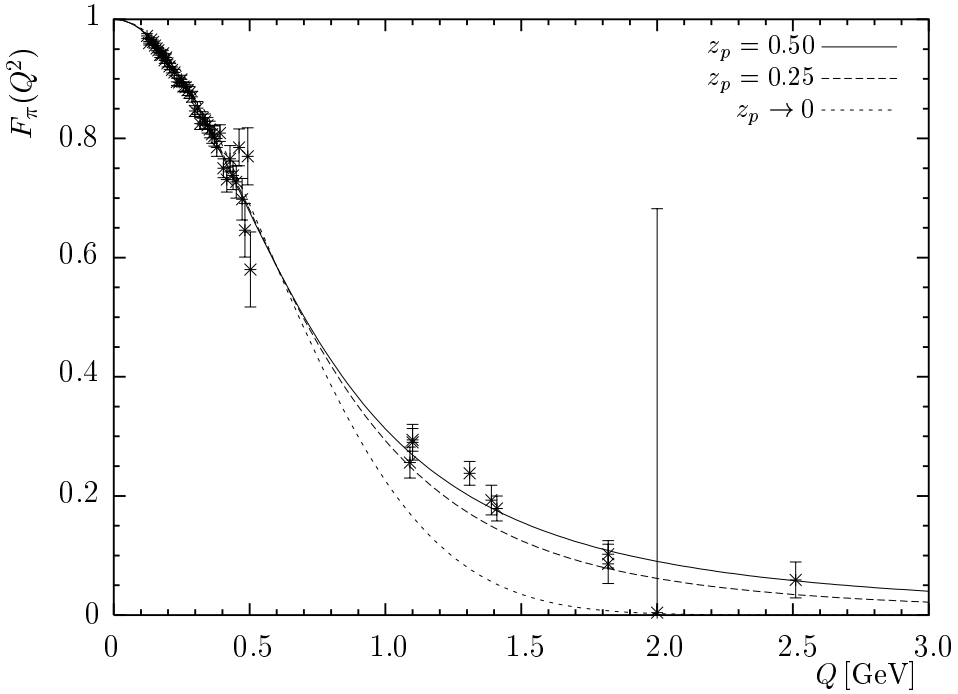

Figure 5.2: The pion form factor for $S_\pi = 0.68\,\text{fm}$ and different values of z_π compared to the experimental data from [76]

For the charged pions $\pi^\pm$ the matrix element of the electromagnetic and the third component of the isospin current are equal. Choosing again the coordinate system as in (5.2) with M_p replaced by m_π we get

$$\langle \pi^+(P')|j^\mu(0)|\pi^+(P)\rangle = e\,(P_+ n_+^\mu + P_- n_-^\mu) F_\pi(Q^2). \tag{5.11}$$

Here the matrix element can be expressed by one form factor F_π only. The calculation of this matrix element in our model leads to

$$F_\pi(Q^2) = \frac{1}{I_\pi} \int_0^1 \mathrm{d}z \, 2z(1-z) \, e^{-(z-\frac{1}{2})^2/2z_\pi^2} \, e^{-\frac{z^2}{2} S_\pi^2 Q^2}. \tag{5.12}$$

We compare (5.12) to experimental data for F_π from [76] in Fig. 5.2. As for the proton the transverse extension parameter S_π can be fitted in the range $0 \leq Q \leq 0.5\,\mathrm{GeV}$ with the result $S_\pi = 0.68\,\mathrm{fm}$. Using the analogue of relation (5.8) for the pion, this value gives an electromagnetic radius $r_{\mathrm{em}}^\pi = 0.64\,\mathrm{fm}$, which is consistent with the experimental value $r_{\mathrm{em}}^\pi = 0.663 \pm 0.006\,\mathrm{fm}$ [76]. For values $Q \gtrsim 0.5\,\mathrm{GeV}$ our fit becomes sensitive to the width of the longitudinal momentum distribution of the constituents. For the pion, the best fit for the width of this distribution is given by $z_\pi = 0.5$. The broader distribution compared to the proton is related to the smaller mass of the pion, which is in agreement with the parametrisation of the hadron wave functions in [37].

Chapter 6

The time-like pion form factor in a dispersion approach

Our aim in this chapter is to develop a dedicated model of the time-like pion form factor. In contrast to the previous chapter, where our main interest lay in the extraction of the parameters z_p, z_π, here we want to give a detailed description of the behaviour of the form factor. First we will give an overview of some models and the regions in which they are applicable. Then we will present our approach and calculate the phase and the modulus of the electromagnetic and charged current form factor. From fits to experimental data we will obtain the masses and decay constants of the neutral and charged ρ-mesons and the ω-meson.

We recall the definition of the electromagnetic form factor of the pion by the matrix element of the electromagnetic current

$$\langle \pi^+(P')|j^\mu(0)|\pi^+(P)\rangle = e(P+P')^\mu F_\pi(q^2), \tag{6.1}$$

where the momentum transfer is $q = P' - P$. The form factor is normalised as $F_\pi(0) = 1$. As function of the complex variable $s = q^2$, the form factor $F_\pi(s)$ has a cut in the complex s-plane starting at the two-pion threshold $s = 4m_\pi^2$ which corresponds to two-pion intermediate states. There are also cuts related to $K\bar{K}$ intermediate states and multi-meson states (4π, etc). The form factor in the time-like region ($s > 0$) is

$$F_\pi(s + i\epsilon) = |F_\pi(s)|e^{i\delta(s)}, \tag{6.2}$$

where $\delta(s)$ is the phase. For the theoretical description of the form factor in different regions of momentum transfers different theoretical approaches are used.

At large space-like momentum transfers, $-q^2 \to \infty$, perturbative QCD (pQCD) gives rigorous predictions for the asymptotic behaviour of the form factor [77]

$$F_\pi(q^2) \sim \frac{8\pi f_\pi \alpha_s(-q^2)}{-q^2}, \tag{6.3}$$

where α_s is the QCD coupling parameter and $f_\pi = 130.7 \pm 0.4\,\mathrm{MeV}$ is the pion decay constant defined by the relation

$$\langle 0|\bar{d}\gamma^\mu\gamma_5 u|\pi^+(P)\rangle = iP^\mu f_\pi. \tag{6.4}$$

As the space-like momentum transfer becomes smaller, the form factor turns out to be the result of the interplay of perturbative and nonperturbative QCD effects, with a strong evidence that nonperturbative QCD effects dominate in the region $0 \leq -q^2 \leq 10\,\mathrm{GeV}^2$ [39]. The picture based on the concept of constituent quarks which effectively account for nonperturbative dynamics has proven to be efficient for the description of the form factor in this region (see for instance [40]). In chapter 5, we also have calculated F_π for small space-like momentum transfers in the framework of our nonperturbative model. This calculation is not intended as a precise determination of the form factor, since our model, in the formulation we use here, was not developed with the attention on the calculation of form factors, but rather on the description of soft high energy hadron-hadron scattering. However, our model has allowed us to give a reasonable description of the experimental data. The agreement could be improved by using a refined model, in particular when using more sophisticated wave functions and more general quark configurations to describe the proton and the pion. Moving on to large time-like momentum transfers, $s \gtrsim 10\,\mathrm{GeV}^2$, $F_\pi(s)$ can be obtained from the analytic continuation of the pQCD formula (6.3). At small time-like momentum transfers the situation is more complicated since there dynamical details of the confinement mechanism are crucial. Quarks and gluons are no longer the degrees of freedom of QCD leading to a simple description of the form factor. At time-like momentum transfers we are essentially in the region of hadronic singularities and typically one relies on methods based on hadronic degrees of freedom. In the region of interest to us here, $0 \leq q^2 \leq 1.5\,\mathrm{GeV}^2$, the lightest pseudoscalar mesons are most important.

There are many approaches to understand the behaviour of the pion form factor at time-like momentum transfers from 0 to 1.5 GeV^2. A time honoured approach is based on the vector meson dominance (VMD) model [41]. In the simplest version of VMD one assumes just the ρ-meson dominance, which leads to

$$F_\pi(s) = \frac{M_\rho^2}{M_\rho^2 - s}, \tag{6.5}$$

where M_ρ is the mass of the ρ-meson. This simple formula works with a good accuracy both for small space-like momentum transfers and time-like momentum transfers below the $\pi\pi$ threshold: $-1\,\mathrm{GeV}^2 \leq s \leq 4m_\pi^2$. For s near the $\pi\pi$ threshold one should take into account effects of the virtual pions. In this region momenta of the intermediate pions are small and a consistent description of the form factor is provided by chiral perturbation theory (ChPT) [42], the effective theory for QCD at low energies.

For higher s, in the region of ρ and ω resonances, a similar rigorous treatment of the form factor is still lacking, and one has to rely on model considerations.

Contributions of the two-pion intermediate states may be consistently described by dispersion representations. The application of dispersion relations has led to the famous Gounaris-Sakurai (GS) formula [43] which takes into account ρ-meson finite width corrections due to virtual pions

$$F_\pi(s) = \frac{M_\rho^2 - B_{\rho\rho}(0)}{M_\rho^2 - s - B_{\rho\rho}(s)}. \tag{6.6}$$

The function $B_{\rho\rho}(s)$ corresponds to the two-pion loop diagram. The corresponding Feynman integral is linearly divergent, but its imaginary part is defined in a unique way. The real part is then reconstructed by a doubly-subtracted dispersion representation. The Gounaris-Sakurai prescription to fix the subtraction constants reads

$$\mathrm{Re}\; B_{\rho\rho}(s)|_{s=M_\rho^2} = 0, \qquad \frac{\mathrm{d}}{\mathrm{d}s}\mathrm{Re}\; B_{\rho\rho}(s)|_{s=M_\rho^2} = 0. \tag{6.7}$$

The phase of the form factor

$$\tan\,\delta(s) = \frac{\mathrm{Im}B_{\rho\rho}(s)}{M_\rho^2 - s - \mathrm{Re}B_{\rho\rho}(s)}. \tag{6.8}$$

for the GS prescription agrees well with the experimental data in the region $4m_\pi^2 < s < 0.9\,\mathrm{GeV}^2$. But (6.6) gives too small a value (by $\approx 15\%$) for $|F_\pi(s)|$ at s around M_ρ^2.

On the other hand, one can consider a simple VMD ansatz taking only the ρ-meson contribution into account. This should be a good approximation in the region $0.5\,\mathrm{GeV}^2 \le s \le 0.8\,\mathrm{GeV}^2$, except for the narrow interval near $s \approx M_\omega^2$ where the $\rho-\omega$ mixing effects are important [78]. The simple VMD ansatz then is very similar to (6.6), but with the numerator replaced by the $\gamma \to \rho \to \pi\pi$ transition matrix element:

$$F_\pi(s) = \frac{\frac{1}{2}g_{\rho\to\pi\pi} f_\rho\; M_\rho}{M_\rho^2 - s - B_{\rho\rho}(s)}. \tag{6.9}$$

Here $g_{\rho\pi\pi}$ and f_ρ are defined according to

$$\langle\pi(k_1)\pi(k_2)|T|\rho(\varepsilon,k)\rangle = \frac{1}{2}g_{\rho\to\pi\pi}\;\varepsilon_\mu(k_1-k_2)^\mu, \tag{6.10}$$

$$\langle 0|J_\mu|\rho^0(\varepsilon,k)\rangle = f_\rho M_\rho\,\varepsilon_\mu, \tag{6.11}$$

where ε_μ is the ρ-meson polarisation and k is the 4-momentum vector. Now $|F_\pi(s)|$ from (6.9) describes well the data for $s \approx M_\rho^2$. But extrapolating (6.9) to $s = 0$ gives $F_\pi(0) \approx 1.15$ in gross violation of the normalisation condition $F_\pi(0) = 1$.

Thus, neither (6.6) nor (6.9) can describe the form factor over the whole range $0 \le s \le 1.5\,\mathrm{GeV}^2$: namely, (6.6) leads to a too small value of $|F_\pi|$ at $s = M_\rho^2$,

whereas the form factor given by (6.9) is far above unity at $s = 0$. There were many attempts to modify the vector meson dominance or to use related approaches in order to bring the results on the pion form factor in agreement with the data (see [79,80] and references therein).

In the following we apply consistently a dispersion approach to the pion form factor in a model with $\rho\pi\pi$, ρKK, $\omega\pi\pi$, and gauge-invariant $\rho-\gamma$, $\omega-\gamma$ and $\rho-\omega$ couplings. Our approach allows a direct resummation of pion and kaon loops. Ambiguities related to subtractions in linearly divergent meson loop diagrams are absorbed in the physical meson masses and coupling constants. After taking into account the $\rho-\omega$ mixing effects the pion form factor in the range $0 \leq s \leq 1\,\mathrm{GeV}^2$ is well described both in magnitude and phase by a formula which is similar to the VMD expressions (6.6) and (6.9) but avoids their pitfalls.

6.1 The dispersion approach

Our model makes use of conventional methods of dispersion theory. First we make an ansatz for the effective couplings of the pseudoscalar mesons, vector mesons and the photon. These couplings are used in essence only to calculate the absorptive parts of the amplitudes. The complete amplitudes are then obtained by dispersion relations and a Dyson resummation. We want to make clear from the outset that our effective couplings discussed below are not to be compared directly to the effective Lagrangian of ChPT [42] and resonance theory in the framework of ChPT [81]. We shall see, however, that our model, used as explained above, respects all the known results from ChPT for the pion form factor. Thus our model can be seen as an alternative to the one of [80] where ChPT results are extended to $F_\pi(s)$ in the range $0 \leq s \leq 1.5\,\mathrm{GeV}^2$ using again a resummation scheme.

In our model pions interact with the ρ-mesons and generate in this way the finite ρ-meson width. We do not include into consideration direct four-pion couplings. Neglecting of the latter goes along the line of the resonance saturation in the ChPT [81] which states that the coupling constants of the effective chiral Lagrangian at order p^4 are essentially saturated by the meson resonance exchange. The ρ^0-meson is coupled to the conserved vector current of charged pions as follows:

$$L_{\rho\pi\pi} = \frac{i}{2} g \left(\pi^\dagger \partial_\mu \pi - \partial_\mu \pi^\dagger \pi\right) \rho^\mu, \tag{6.12}$$

where ρ^μ is the conserved vector field describing the ρ-meson. We denote in this section $g \equiv g_{\rho\to\pi\pi}$. Matching to the one-loop ChPT [42] leads to the relation

$$g_{\rho\to\pi\pi} = 2M_\rho/f_\pi. \tag{6.13}$$

The photon is coupled to the charged pion through the usual minimal coupling,

$$L_{\gamma\pi\pi} = ie(\pi^\dagger \partial_\mu \pi - \partial_\mu \pi^\dagger \pi) A^\mu. \tag{6.14}$$

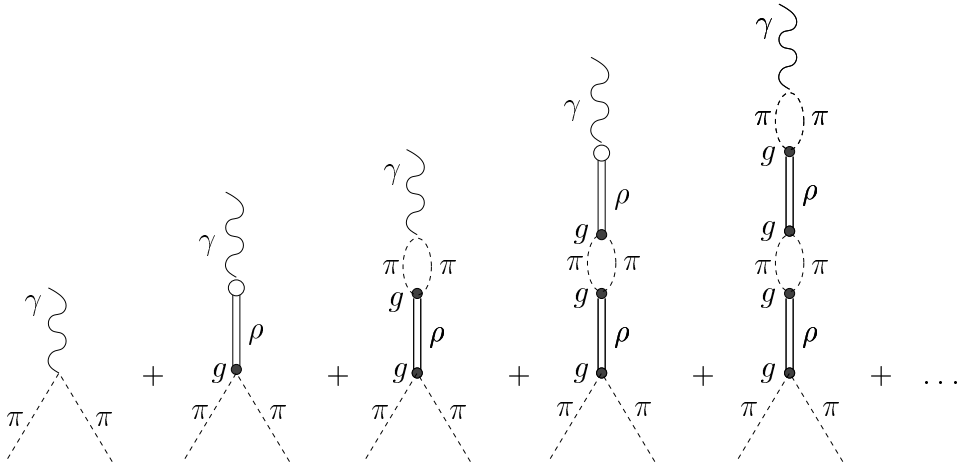

Figure 6.1: The pion form factor in the picture where pions interact via the ρ-meson exchange and generate in this way the finite ρ-meson width. The photon is coupled to the charged pions through the usual minimal coupling, and the direct gauge-invariant $\rho-\gamma$ coupling is assumed. No G-parity violating effects are included at this stage.

We also add a direct gauge-invariant $\rho - \gamma$ coupling of the form

$$L_{\rho\gamma} = -\frac{1}{4}\frac{e f_\rho}{M_\rho} F^{\mu\nu} G^{(\rho)}_{\mu\nu}, \tag{6.15}$$

where

$$F_{\mu\nu} = \partial_\mu A_\nu - \partial_\nu A_\mu, \qquad G^{(\rho)}_{\mu\nu} = \partial_\mu \rho_\nu - \partial_\nu \rho_\mu. \tag{6.16}$$

This model is similar to the model of [82]. No G-parity violating $\omega\pi\pi$ or direct $\rho - \omega$ couplings are included at this stage. As explained above, we calculate the electromagnetic form factor in our model by the sum of the diagrams of Fig. 6.1. Summing all the pion loop insertions, we obtain

$$\begin{aligned} F_\pi(s) &= 1 + \frac{\frac{f_\rho}{2M_\rho} s \cdot g + \frac{g}{2} B_{\rho\gamma}(s)}{M_\rho^2 - s - B_{\rho\rho}(s)} \\ &= \frac{M_\rho^2 - (1 - \frac{f_\rho}{2M_\rho} g)s + \left\{\frac{1}{2} g\, B_{\rho\gamma}(s) - B_{\rho\rho}(s)\right\}}{M_\rho^2 - s - B_{\rho\rho}(s)}. \end{aligned} \tag{6.17}$$

The quantities $B_{\rho\rho}(s)$ and $B_{\rho\gamma}(s)$ correspond to one-loop $\rho - \gamma$ and $\rho - \rho$ self energy diagrams generated by the pion loop. The imaginary parts of these diagrams can be calculated by setting the intermediate pions on mass shell. The full functions $B_{\rho\rho}(s)$ and $B_{\rho\gamma}(s)$ are constructed from their imaginary parts by means of the spectral representation with a suitable number of subtractions and by adding the

corresponding subtraction constants. This is the usual dispersion theory procedure which we adopt since the Feynman integral for the pion one-loop diagram leads to a divergent expression. For the $\pi\pi$ intermediate states the imaginary parts of the functions $B_{\rho\rho}(s)$ and $B_{\rho\gamma}(s)$ satisfy the relations

$$\begin{aligned} \text{Im } B_{\rho\rho}(s) &= g^2 \text{Im } B_{\pi\pi}(s), \\ \text{Im } B_{\rho\gamma}(s) &= 2g \text{ Im } B_{\pi\pi}(s), \end{aligned} \tag{6.18}$$

where

$$\text{Im } B_{\pi\pi}(s) \equiv I(s, m_\pi^2) = \frac{1}{192\pi} s \left(1 - \frac{4m_\pi^2}{s}\right)^{3/2}. \tag{6.19}$$

For a realistic description we have to take into account also contributions of K^+K^- and $K^0\bar{K}^0$ intermediate states. The coupling constant $g_{\rho\to KK}$ cannot be measured directly. We use the relation

$$2g_{\rho\to KK} = g_{\rho\to\pi\pi} = g, \tag{6.20}$$

which is valid in the SU(3) limit. Repeating the procedure described above, summing the pion and kaon loops, we find with (6.20)

$$\begin{aligned} \text{Im } B_{\rho\rho} &= g^2 \left(\text{Im } B_{\pi\pi} + \frac{1}{4}\left(\text{Im } B_{K^+K^-} + \text{Im } B_{K^0\bar{K}^0}\right)\right) \\ &= g^2 \left(\text{Im } B_{\pi\pi} + \frac{1}{2}\text{Im } B_{KK}\right), \\ \text{Im } B_{\rho\gamma} &= 2g \left(\text{Im } B_{\pi\pi} + \frac{1}{2}\text{Im } B_{K^+K^-}\right) \\ &= 2g \left(\text{Im } B_{\pi\pi} + \frac{1}{2}\text{Im } B_{KK}\right), \end{aligned} \tag{6.21}$$

and hence

$$\frac{1}{2}\, g \text{ Im } B_{\rho\gamma}(s) - \text{Im } B_{\rho\rho}(s) = 0. \tag{6.22}$$

It follows from (6.22) that the difference $\frac{1}{2}gB_{\rho\gamma}(s) - B_{\rho\rho}(s)$ is a polynomial in s determined by the subtraction conditions. Hence the numerator of the pion form factor (6.17) is also a real polynomial. Therefore, the phase of the form factor is completely determined by the denominator. The latter is the usual propagator of the ρ-meson with the finite width corrections taken into account.

Let us now consider subtraction constants. The function $B_{\rho\gamma}(s)$ describes the coupling of the pion to the conserved electromagnetic current. Therefore we must set

$$B_{\rho\gamma}(0) = 0, \tag{6.23}$$

such that the charge of the pion remains unrenormalised by higher order corrections. The function $B_{\rho\rho}(s)$ determines the behaviour of the $\pi\pi$ elastic $J^P = 1^-$ partial wave amplitude in which the ρ-meson pole is known to be present in the zero-width limit. Therefore, we require

$$\mathrm{Re}\, B_{\rho\rho}(M_\rho^2) = 0. \tag{6.24}$$

Without loss of generality the second subtraction constant may be fixed by setting

$$B_{\rho\rho}(s=0) = 0. \tag{6.25}$$

Any other condition would just lead to rescaling of the parameters in the formula for the form factor. Thus, the most general expression for the form factor incorporating subtraction ambiguities in the $\pi\pi$ and KK loop diagrams contains three[1] constants M_ρ^2, g, and f_ρ:

$$F_\pi(s) = \frac{M_\rho^2 - (1 - \frac{f_\rho}{2M_\rho} g)s}{M_\rho^2 - s - B_{\rho\rho}(s)}. \tag{6.26}$$

Here

$$\begin{aligned} B_{\rho\rho}(s) &= g^2\, s \left(R(s, m_\pi^2) - R(M_\rho^2, m_\pi^2) + \frac{R(s, m_K^2) - R(M_\rho^2, m_K^2)}{2} \right) \\ &\quad + i g^2 \left(I(s, m_\pi^2) + \frac{I(s, m_K^2)}{2} \right), \end{aligned} \tag{6.27}$$

with $I(s, m^2)$ defined by (6.19), and

$$\begin{aligned} R(s, m^2) &= \frac{1}{192\pi^2}\ \mathrm{V.P.} \int_{4m^2}^{\infty} \frac{ds'}{(s'-s)s'} \left(1 - \frac{4m^2}{s'}\right)^{3/2} \\ &= \begin{cases} \frac{1}{96\pi^2} \left(\frac{1}{3} + \xi^2 + \frac{\xi^3}{2} \log\left(\frac{1-\xi}{1+\xi}\right) \right), & \xi = \sqrt{1 - \frac{4m^2}{s}}, \quad \text{for } s \geq 4m^2, \\ \frac{1}{96\pi^2} \left(\frac{1}{3} - \xi^2 + \xi^3 \cdot \arctan\left(\frac{1}{\xi}\right) \right), & \xi = \sqrt{\frac{4m^2}{s} - 1}, \quad \text{for } s < 4m^2, \end{cases} \end{aligned} \tag{6.28}$$

where V.P. means the principle value. Let us point out that the numerator of the form factor in (6.26) is not a constant, but a linear function of s. This s-dependence appears as the direct consequence of current conservation. We can write (6.26) in the form of the modified GS formula

$$F_\pi(s) = \frac{\frac{1}{2} g_{\rho\to\pi\pi} f_\rho^{\mathrm{eff}}(s) M_\rho}{M_\rho^2 - s - B_{\rho\rho}(s)} \tag{6.29}$$

[1] Assuming more than two subtractions in the pion loop diagrams leads to more subtraction constants. This is not dictated by the convergence properties of the loop diagrams, but is still possible. We will not discuss such a case here.

with the effective s-dependent $\rho-\gamma$ coupling constant

$$f_\rho^{\rm eff}(s) = f_\rho \frac{s}{M_\rho^2} + \frac{2(M_\rho^2 - s)}{g M_\rho}. \tag{6.30}$$

One should be careful with the interpretation of this result: as is clear from (6.23), there is no direct transition of the ρ-meson to the real photon as a consequence of the gauge invariant $\rho-\gamma$ coupling. On the other hand, the effective coupling $f_\rho^{\rm eff}(s)$ is clearly nonzero at $s=0$. Therefore the pion form factor looks as if there was direct $\rho-\gamma$ coupling also for the real photon. This is just the usual vector meson dominance. The latter thus emerges as the direct consequence of our assumption that the vector meson couples to the same pion current as the photon. For further discussions of the relationship between VMD and gauge invariance we refer to [82]. If we use the ChPT relation (6.13), which agrees perfectly with the measured value of $g_{\rho\to\pi\pi}$, then (6.30) leads to an interesting relation

$$f_\rho^{\rm eff}(s=0) = f_\pi. \tag{6.31}$$

Notice that the phase of $F_\pi(s)$ in (6.29) is still given by (6.8) and is completely determined by the function $B_{\rho\rho}(s)$.

6.2 The $\rho-\omega$ mixing

In section 6.1 we discussed the ρ contribution due to the bare ρ plus the effects of the ρ-meson width due to the light-meson loops to the pion form factor. This analysis is sufficient for describing the pion form factor of the charged vector current using the CVC relation. For the electromagnetic pion form factor it is necessary to take into account the $\rho-\omega$ mixing effects. The ω is coupled to the pions and the photon similarly to the ρ^0-meson (see (6.12) and (6.15))

$$L_{\omega\pi\pi} = \frac{i}{2} g_{\omega\to\pi\pi}\left(\pi^\dagger\partial_\mu\pi - \partial_\mu\pi^\dagger\pi\right)\omega^\mu, \qquad L_{\omega\gamma} = -\frac{1}{4}\frac{e f_\omega}{M_\omega} F^{\mu\nu} G^{(\omega)}_{\mu\nu}, \tag{6.32}$$

ω_μ being a conserved vector field describing the ω-meson and $G^{(\omega)}_{\mu\nu} = \partial_\mu\omega_\nu - \partial_\nu\omega_\mu$.

It has proven useful to classify various contributions to hadronic amplitudes according to their formal order in the $1/N_c$ expansion [42], where N_c=3 is the number of colours in QCD. In the language of the $1/N_c$ expansion the analysis of the previous section corresponds to taking into account the leading order $1/N_c$ process, which corresponds to the resonance contribution in a zero-width approximation, and the subleading $\mathcal{O}(1/N_c)$ effects of the meson loops.[2] Performing a resummation of these meson loops gave our dispersion description of the form factor.

[2]Recall that pion and kaon loop diagrams are of order $1/N_c$ and of order p^4 of the momentum expansion.

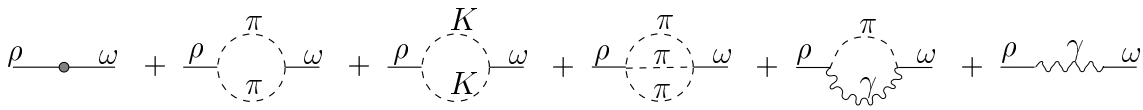

Figure 6.2: Diagrams which contribute to the $\rho - \omega$ mixing amplitude $B_{\rho\omega}$. The direct $\rho - \omega$ mixing diagram is the only diagram which emerges to leading order in $1/N_c$, meson-loop diagrams are subleading $1/N_c$ effects.

A corresponding treatment of the $\rho - \omega$ mixing effects then requires taking into account the leading and subleading $1/N_c$ effects as well. To leading order in $1/N_c$, meson loops do not contribute and therefore the only effect is the direct $\rho - \omega$ transition described in terms of the direct coupling (see Fig. 6.2).

At subleading $1/N_c$ order several meson loop diagrams shown in Fig. 6.2 emerge. We make use of spectral representations for loop diagrams, i.e. we calculate directly the imaginary parts and then reconstruct the full function by means of the spectral integral with the relevant number of subtractions. Subtraction constants then are either fixed by physical constraints or determined by the experimental data. Let us point out an important feature related to our dispersion calculation: the direct $\rho - \omega$ coupling, which is a leading $1/N_c$ process and the real part of the $\rho - \omega$ mixing loop diagrams at $q^2 = M_\rho^2$, which is a subleading $1/N_c$ process, contribute to the form factor precisely in the same way, such that only their sum has a physical meaning. We therefore account for the net effect of these two contributions by a single subtraction constant and do not consider the direct $\rho - \omega$ coupling separately.

We have analysed in section 6.1 the ρ-meson self-energy function $B_{\rho\rho}$ which determines the propagator of the interacting ρ-meson. Let us now discuss a similar self-energy function of the ω-meson $B_{\omega\omega}$ and the off-diagonal $\rho - \omega$ function $B_{\rho\omega}$ which describes the $\rho - \omega$ mixing.

The function $B_{\omega\omega}$ determines the ω propagator $D_\omega(s) = 1/(M_\omega^2 - s - B_{\omega\omega})$ in the absence of the $\rho - \omega$ mixing effects. The main contribution to Im $B_{\omega\omega}$ is given by the three-pion intermediate states. This Im $B_{\omega\omega}$ should then be inserted into a dispersion integral to obtain $B_{\omega\omega}$. However, because of the small width of the ω resonance, it is sufficient for our analysis to consider as a simple ansatz a constant $B_{\omega\omega}$

$$B_{\omega\omega} = i\Gamma_\omega^{tot} M_\omega. \tag{6.33}$$

Possible processes which contribute to the $\rho - \omega$ mixing amplitude $B_{\rho\omega} = B_{\omega\rho}$ are shown in Fig. 6.2. The coupling constants which determine the relative strength of the diagrams in Fig. 6.2 are shown in Table 6.1. One finds (see also [83]) that the main contribution to the imaginary part of the $\rho - \omega$ mixing amplitude $B_{\rho\omega}$ is given by the diagrams with two-pion and two-kaon intermediate states. To obtain the full $B_{\rho\omega}$ we write again a dispersion representation with two subtractions. The

Res.	M [MeV]	$\Gamma^{\rm tot}$ [MeV]	$\Gamma_{e^+e^-}$ [keV]	$Br(\pi^+\pi^-)$	$Br(\pi^0\gamma)$
ρ^0	769.0 ± 0.9	150.7 ± 2.9	6.77 ± 0.32	100%	$(6.8 \pm 1.7)\cdot 10^{-4}$
ω	782.57 ± 0.12	8.44 ± 0.09	0.60 ± 0.02	$(2.21 \pm 0.3)\%$	$(8.5 \pm 0.5)\cdot 10^{-2}$

Res.	f_V [MeV]	$g_{V\to 2\pi}$
ρ^0	152 ± 5	11.8 ± 0.2
ω	45.3 ± 0.9	0.4 ± 0.02

Table 6.1: Masses and rates for vector mesons from [11] and the corresponding decay constants. Recall the SU(2)-limit relations $f_\rho = 3 f_\omega$.

imaginary parts of these diagrams can be calculated in analogy to (6.18) in terms of the coupling constants $g_{V\to PP}$ with $V = \rho, \omega$, $P = \pi, K$ defined according to the relation

$$\langle P(k_1)\bar{P}(k_2)|T|V(\varepsilon,k)\rangle \;=\; \frac{1}{2} g_{V\to PP}\varepsilon_\mu^{(V)}(k_1-k_2)^\mu.$$

For instance, the imaginary part of the diagram with the $\pi\pi$ intermediate state is equal to $g_{\rho\to\pi\pi}g_{\omega\to\pi\pi}I(s,m_\pi^2)$.

The same arguments as used to show the relation (6.22) between Im $B_{\rho\gamma}$ and Im $B_{\rho\rho}$ lead to

$$g_{\rho\to\pi\pi}\text{Im } B_{\rho\omega}(s) - g_{\omega\to\pi\pi}\text{Im } B_{\rho\rho}(s) = 0. \tag{6.34}$$

Hence, the combination $g_{\omega\to\pi\pi}B_{\rho\rho} - g_{\rho\to\pi\pi}B_{\rho\omega}$ is a polynomial of first order in s. The $\rho-\omega$ mixing effects are sizeable only in the narrow vicinity of $s = M_\omega^2$, so we may set

$$g_{\rho\to\pi\pi}B_{\rho\omega} - g_{\omega\to\pi\pi}B_{\rho\rho} = s\,\Delta, \tag{6.35}$$

and the value of Δ will be found from the fit to the pion form factor. As we have explained above, the real part of the function $B_{\rho\omega}$ at $s \approx M_{\rho,\omega}^2$ includes the direct $\rho-\omega$ coupling.

6.3 The electromagnetic pion form factor with $\rho-\omega$ mixing

In the problem of the $\rho-\omega$ mixing, the constant $g_{\omega\to 2\pi}$ is a natural small parameter, and the expansion of the pion form factor in powers of this parameter can be constructed. We can safely neglect all terms of order $g_{\omega\to\pi\pi}^2$ and limit ourselves to the first order analysis. The diagrams which describe the contributions to the

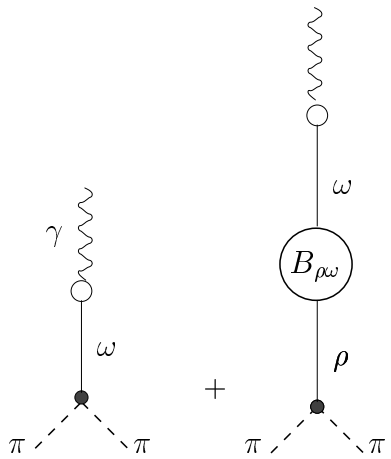

Figure 6.3: Diagrams for the pion form factor which emerge at first order of the expansion in $g_{\omega\to\pi\pi}$. In this figure the ρ and ω propagators are $D_\rho = 1/(M_\rho^2 - s - B_{\rho\rho})$ and $D_\omega = 1/(M_\omega^2 - s - B_{\omega\omega})$, respectively.

form factor of first order in $g_{\omega\to 2\pi}$ are shown in Fig. 6.3. Adding the corresponding expressions to the result (6.29) we get for the pion form factor

$$F_\pi(s) = \frac{\frac{1}{2} g_{\rho\to\pi\pi} f_\rho^{\rm eff}(s) M_\rho}{M_\rho^2 - s - B_{\rho\rho}(s)} + \frac{\frac{1}{2} g_{\omega\to\pi\pi} \frac{f_\omega s}{M_\omega}}{M_\omega^2 - s - B_{\omega\omega}(s)} \left\{ \frac{M_\rho^2 - s + \Delta \cdot s}{M_\rho^2 - s - B_{\rho\rho}(s)} \right\} + \mathcal{O}(g_{\omega\to\pi\pi}^2). \tag{6.36}$$

We use this expression for the numerical analysis of the data for the electromagnetic pion form factor in the next section.

6.4 Numerical analysis

In this section we apply the formulas obtained to the analysis of the data on the electromagnetic and charged current pion form factors and extract in this way the resonance masses and coupling constants. We include the contributions of the $\rho(770)$ and $\omega(782)$ resonances and neglect the higher vector resonances $\rho(1450)$ and $\rho(1700)$ (for a discussion of these latter see [84]). As can be seen from the analysis of [85], the influence of the latter upon the pion form factor is negligible in the region $s \leq 1$ GeV. We therefore extract the ρ and ω parameters making use of the form factor data for $s \leq 1$ GeV.

6.4.1 The electromagnetic pion form factor

We fit the available data on the phase [86] and the modulus [76, 87] of the electromagnetic pion form factor to (6.36) which includes the $\rho - \omega$ mixing effects. The

form factor turns out to be weakly sensitive to $g_{\omega\to\pi\pi}$ and f_ω for which we use the values from Table 6.1.

The resonance parameters turn out to be rather sensitive to the upper limit $\sqrt{s} \leq Q_{\rm upper}$ of the data points included into the fit procedure. The extracted masses and couplings from the best fit of the form factor, which was done separately for the phase and the modulus, are shown in Table 6.2 and 6.3, respectively. This dependence on $Q_{\rm upper}$ might signal that the errors in the extracted masses and coupling constants are in fact sizeably greater than those quoted in [11]. Obviously, the error estimates provided by the popular FUMILI [88] program should be taken with some care.

$Q_{\rm upper}$, MeV	710 (5 pts)	775 (10 pts)	850 (15 pts)	965 (20 pts)
M_{ρ^0}, MeV	772.7 ± 1.3	773.4 ± 0.8	773.0 ± 0.6	771.1 ± 0.6
$g_{\rho^0\to\pi^+\pi^-}$	12.05 ± 0.07	12.0 ± 0.05	12.0 ± 0.04	11.87 ± 0.04

Table 6.2: The upper limit of the $\sqrt{s}$-range of the data from [86] used for fitting the phase of the pion form factor and the corresponding fitted parameters M_ρ and $g_{\rho\to 2\pi}$. Error estimates as given by the FUMILI program are shown.

$Q_{\rm upper}$ [MeV]	820 (27 pts)	950 (40 pts)	1000 (45 pts)	960 (40 pts [76] + 45 pts [87])
M_{ρ^0} [MeV]	774.7 ± 0.3	776.1 ± 0.2	773.6 ± 0.2	775.5 ± 0.1
f_{ρ^0} [MeV]	147.7 ± 0.2	148.2 ± 0.1	149.0 ± 0.1	149.4 ± 0.1
$g_{\rho^0\to\pi^+\pi^-}$	11.37 ± 0.03	11.38 ± 0.01	11.7 ± 0.01	11.5 ± 0.05
M_ω [MeV]	782.5 ± 0.3	781.3 ± 0.2	781.9 ± 0.2	782.5 ± 0.2
Δ	0.180 ± 0.007	0.191 ± 0.006	0.183 ± 0.006	0.170 ± 0.007

Table 6.3: The upper limit of the Q-range of the data [76], used for fitting the modulus of the pion form factor and the corresponding fitted parameters M_ρ, f_ρ, $g_{\rho\to 2\pi}$, M_ω, and Δ. The last column shows the result of the fit to the combined data on $|F_\pi|$ from [76] and [87]. Error estimates as given by the FUMILI program are shown.

Our best estimates for the ρ and ω parameters from a combination of the fits to the phase and the modulus are presented in Table 6.5. We obtain these values as follows: the parameter values from the last columns of Tables 6.2 and 6.3 should be the most reliable ones, since they correspond to the biggest data sets. On the other hand, the errors given by the FUMILI program cannot be trusted. We took the average of the values for M_ρ^0 and $g_{\rho\to\pi\pi}$, weighting the values from the modulus fit by a factor 2/3 and those from the phase fit by 1/3. The errors in Table 6.5 are our educated guesses.

The pion elastic form factor calculated with the central values of the parameters from Table 6.5 is shown in Fig. 6.4. Both the phase and the magnitude of the form factor are well described, except for the phase at $\sqrt{s} > 0.9$ GeV.

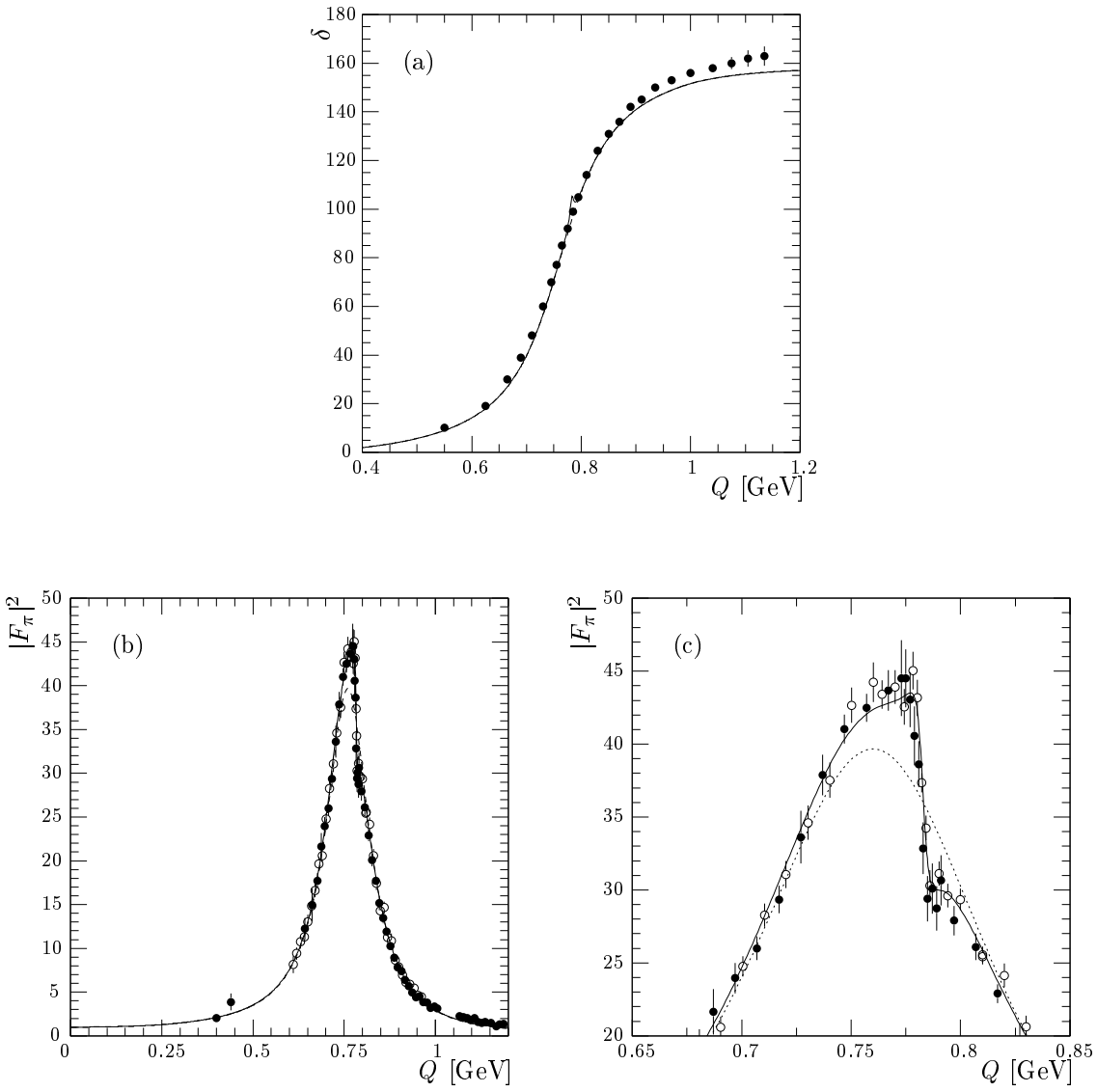

Figure 6.4: The phase (a) and the modulus (b,c) of the pion form factor from the ρ contribution (dotted line) and with $\rho - \omega$ mixing effects (solid line) compared to the data on the phase from [86] and the data on the modulus from [76] (solid circles) and [87] (empty circles). For the calculation the central values of the parameters from Table 6.5 have been used.

6.4.2 The charged current pion form factor

The amplitude of the weak transition $\tau^- \to \pi^-\pi^0\nu_\tau$ can be parametrised in terms of the two $\pi^- \to \pi^0$ transition form factors as follows

$$\langle \pi^0(p')|\bar{u}\gamma_\mu d|\pi^-(p)\rangle = \frac{1}{\sqrt{2}}F_\pi^+(q^2)(p'+p)_\mu + \frac{1}{\sqrt{2}}F_\pi^-(q^2)q_\mu. \tag{6.37}$$

In the isospin limit $F_\pi^- = 0$ and $F_\pi^+ = F_\pi$. These relations should work well for all q^2 except for the region of the ρ and ω resonances: the form factor F_π contains contributions of the ρ^0 and ω resonance, whereas the contribution analogous to ω is absent in F_π^+. Thus, the charged current form factor F_π^+ as measured in the $\tau^- \to \pi^0\pi^-\nu_\tau$ decay is given in our model by the the modified ρ dominance formula (6.29). Comparison with the ALEPH [85] and CLEO [89] data allows the extraction of the masses and coupling constants of the ρ^-. We give the corresponding numbers in Table 6.4 and plot the form factor in Fig. 6.5.

$Q_{\rm upper}$ [MeV]	760 (18 pts)	900 (23 pts)	1025 (28 pts)
M_{ρ^-} [MeV]	768.8 ± 0.3	775.1 ± 0.1	776.9 ± 0.1
f_{ρ^-} [MeV]	144.9 ± 0.3	150.3 ± 0.1	150.1 ± 0.1
$g_{\rho^-\to\pi^0\pi^-}$	11.22 ± 0.02	11.34 ± 0.01	11.80 ± 0.05

Table 6.4: Fit to the charged current pion form factor from the CLEO data [89] on the $\tau^- \to \pi^-\pi^0\nu_\tau$ decay. The upper limit $Q_{\rm upper}$ of the $\sqrt{s}$-range of the data used and the corresponding fitted parameters for the ρ^- meson. Error estimates as given by the FUMILI program are shown.

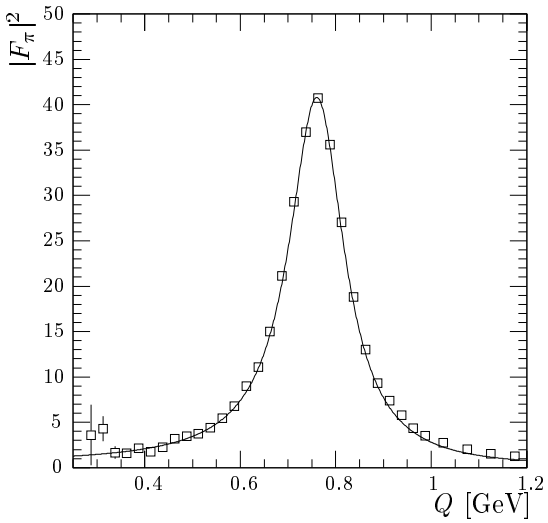

Figure 6.5: The charged current pion form factor calculated for the parameter set obtained for $Q_{\rm upper} = 900$ MeV from Table 6.4 compared to the CLEO data [89]

To conclude this chapter we summarise our final results for the ρ^0, ρ^- and ω parameters which we extracted from fits to the data on the electromagnetic [76,86,87] and charged current [85,89] pion form factors in Table 6.5. The masses, the weak decay constants and the pionic coupling constants of the neutral and charged ρ-mesons are found to be equal within the errors. Let us point out that our fitted value for $g_{\rho\to 2\pi}$ agrees perfectly with the ChPT prediction $g_{\rho\to 2\pi} = 2M_\rho/f_\pi$=11.7. We notice that our central values of the ρ masses are 2-3 MeV higher than the corresponding numbers obtained from the same reactions by [11]. A comparison of the data and the theoretical curves for the electromagnetic and charged current pion form factors is presented in Fig. 6.6. We point out that the $\rho-\omega$ mixing gives a sizeable contribution to the electromagnetic form factor in the region of the ρ and ω resonances, where it leads to an increase of $|F_\pi|^2$ by 10% at $s = M_\rho^2$ and by almost 30% at $s = M_\omega^2$.

M_{ρ^-} [MeV]	M_{ρ^0} [MeV]	M_ω [MeV]	f_ρ [MeV]	$g_{\rho\to\pi\pi}$	Δ
775 ± 2	774 ± 2	782.0 ± 0.5	149 ± 1	11.6 ± 0.3	0.17 ± 0.02

Table 6.5: The masses and decay constants of the vector mesons and the $\rho-\omega$ mixing parameter Δ (see (6.35)) as obtained by our analysis

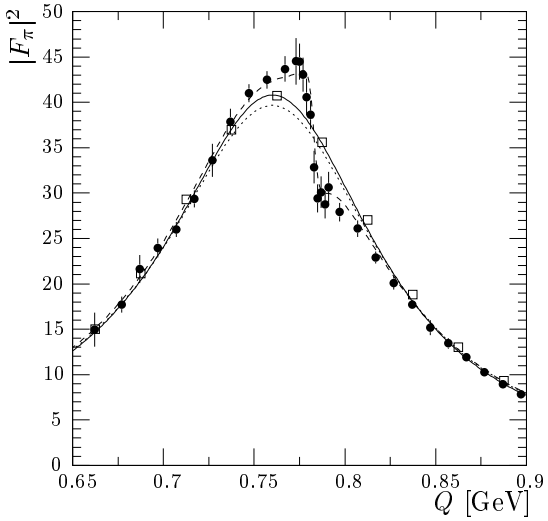

Figure 6.6: Comparison of the electromagnetic (full circles) [76,87] and the charged current form factor from the $\tau^- \to \pi^-\pi^0\nu_\tau$ decay (open squares) [89] with our fits. The fits to the electromagnetic pion form factor show the ρ^0 contribution (dotted line) and the result including $\rho-\omega$ mixing (dashed line). The fit to the charged current pion form factor is the solid line.

Chapter 7

Conclusions

In this work we examine soft high energy reactions in the framework of nonperturbative QCD. In the first part we calculate total and differential cross sections for elastic and inelastic diffractive scattering. In our model we start from a microscopic description of the scattering of quark-antiquark and quark-diquark wave packets and use functional integral methods to obtain expressions for the scattering amplitudes. The correlation functions of light-like Wegner-Wilson loops governing these amplitudes are evaluated in the framework of the model of the stochastic vacuum [23–26]. The hadron-hadron scattering amplitudes are obtained by multiplying the parton scattering amplitudes with suitable hadronic wave functions [37]. Both a matrix cumulant expansion for the correlation function of two Wegner-Wilson loops as developed in [30] and an expansion method [24, 27] are used.

The free parameters of our model are those of the model of the stochastic vacuum: G_2, a and κ, and the ones of the wave functions: S_{h_i} and z_{h_i}, determining the width of the transverse and longitudinal momentum distributions of the constituents of the hadrons, respectively. These parameters have been determined in previous work [24, 30] on elastic scattering. The extension parameters S_{h_i} are allowed to depend on the c.m. energy according to (4.1) and (4.3) respectively. In this sense different hadrons are characterised through their radii, which come out close to the corresponding electromagnetic radii of the hadrons for energies $\sqrt{s} \approx 20$ GeV. The values for z_{h_i} are obtained from a calculation of form factors in our model.

With all parameters fixed, integrated and differential cross sections for proton-proton and proton-pion scattering are calculated and compared to experimental results [58–63, 66–68]. Our model does not distinguish between pp and $p\bar{p}$ scattering or $p\pi^+$ and $p\pi^-$ scattering, respectively.

The calculated integrated elastic cross sections agree with the experimental values within the numerical and experimental errors for a wide range of c.m. energies starting at about $\sqrt{s} = 20$ GeV up to the Tevatron energy $\sqrt{s} = 1800$ GeV. The differential elastic cross sections are described reasonably well over many orders of magnitude by the matrix cumulant method, however, this method underestimates the data for small $|t|$. On the other hand the expansion method gives a good

description of the differential cross sections for $|t| \lesssim 0.2\,\mathrm{GeV}^2$ but overshoots the data for larger values of $|t|$. As a consequence of the integrated cross sections being mainly due to the contributions from small $|t|$, the expansion method gives better results here whereas the matrix cumulant method tends to underestimate the experimental data. The difference between the results obtained from both methods can be seen as a theoretical error estimate of our model, as they use different approximation schemes in the evaluation of the correlation function. In the approximation we use in this work we have $C = P = +1$ exchange only.

Furthermore the rise of the integrated cross sections in single diffractive dissociation as a function of $\sqrt{s}$ is calculated. Our calculated ratio $\sigma_{\mathrm{sd}}/(\sigma_{\mathrm{el}} + \sigma_{\mathrm{sd}})$ is in rough agreement with experiment. The experimentally observed behaviour that the diffractive dissociation part of the cross section increases more slowly with $\sqrt{s}$ than the elastic one is reproduced qualitatively in our calculation. The differential distribution can be reasonably well described by the expansion method. The difficulties we encounter in the description of $\mathrm{d}\sigma_{\mathrm{sd}}/\mathrm{d}t$ by means of the matrix cumulant method, i.e. the formation of a depression at $|t| \approx 0.3\,\mathrm{GeV}^2$, are investigated in a second approach. This approach uses two-dimensional harmonic oscillator wave functions instead of plane waves for the description of the diffractive final state and confirms the results found before, but allows us to analyse the origin of the observed depression. Again the process is mediated by $C = P = +1$ exchange only in our approximation.

Turning to double diffractive excitation $pp \to N(1535)N(1535)$ we study $C = P = -1$ exchange in the framework of our model, which arises due to the symmetries of the final state wave functions. The qualitative features of our predictions for the integrated and differential cross sections resemble the ones of the results from $C = P = +1$ exchange, the exception being a rather slow decrease of the differential distribution with increasing momentum transfer. This behaviour is also known from the helicity amplitude $A^p_{1/2}$ measured in the context of the electromagnetic $p - N(1535)$ transition form factor. However, due to restrictions of our model, in particular the simple ansatz for baryons, which are given by wave packets of a quark and a scalar diquark, we cannot calculate this helicity amplitude in our model and therefore are not able to compare to experimental data.

The last chapter in the first part of our work deals with form factors at small space-like momentum transfers, calculated in the framework of our model. Our result for the isovector Dirac form factor of the proton and the electromagnetic form factor of the pion, as well as the electromagnetic radii extracted from them, compare reasonably well to experimental data.

To summarise the first part, our model is quite well suited to describe inelastic diffractive hadronic reactions at high c.m. energies ($\sqrt{s} \gtrsim 20$ GeV) and small momentum transfer. Further progress could be made when including higher cumulant terms in (3.16) which would contribute to both $C = P = +1$ and $C = P = -1$ exchange. The hope is that these contributions could, at least partly, fill up the dips

encountered in various contributions to the differential cross sections and thus lead to an improved description of the data. Also a more refined hadron model could help avoid some shortcomings of the model as discussed in particular in the context of the spin-flip contribution to the form factor.

The upcoming experiments e.g. at RHIC will be a rich source for new experimental data for both single and double diffractive dissociation in hadronic reactions at high c.m. energies. Therefore the study of inelastic diffractive scattering will remain an interesting and instructive field of work, where effects of nonperturbative QCD can be studied.

In the second part of our work we analyse the electromagnetic and charged current pion form factors at time-like momentum transfers in a dispersion approach. Here we consider a model with $\rho\pi\pi$, ρKK, $\omega\pi\pi$, ωKK and gauge-invariant $\rho-\gamma$ and $\omega-\gamma$ couplings. The pion form factor is obtained by a resummation of pion and kaon loops leading to the finite width of the ρ-meson. The resulting expression for the pion form factor takes the form of the vector meson dominance formula with one important distinction: the effective decay constant $f_\rho^{\rm eff}$ depends linearly on the momentum transfer squared. We also take into account the $\rho-\omega$ mixing in the electromagnetic pion form factor.

The values of the ρ^0 and ω parameters are extracted from the fit to the electromagnetic pion form factor [76, 86, 87] at $0 \leq \sqrt{s} \leq 1.0\,\mathrm{GeV}$ where contributions of higher vector meson resonances are negligible. The $\rho-\omega$ mixing is found to give a sizeable contribution to the electromagnetic form factor in the region of the ρ and ω resonances, where it leads to an increase of $|F_\pi|^2$ by 10% at $s=M_\rho^2$ and by almost 30% at $s=M_\omega^2$.

The values of the ρ^- parameters are obtained by the fit to the charged current pion form factor measured in τ decay [85, 89].

Our best estimates for the ρ and ω parameters are presented in Table 6.5. The masses, the weak decay constants and the pionic coupling constants of the neutral and charged ρ-mesons are found to be equal within the errors andour fitted value for $g_{\rho\to 2\pi}$ agrees perfectly with the ChPT prediction $g_{\rho\to 2\pi}=2M_\rho/f_\pi$=11.7.

To summarise the second part of our work, we have presented a model which gives a good description the electromagnetic and charged current pion form factor in the region $0 \leq \sqrt{s} \leq 1.0\,\mathrm{GeV}$ including the effects due to $\rho-\omega$ mixing. The ρ and ω parameters which we obtain from our model are within errors in agreement to experimental data [11].

Appendix A

Conventions

Throughout this work we use natural units, in which

$$\hbar = c = 1. \tag{A.1}$$

The fine structure constant of the electromagnetic interaction is given in Heaviside-Lorentz units by

$$\alpha_{\text{e.m.}} = \frac{e^2}{4\pi} \approx \frac{1}{137}. \tag{A.2}$$

Latin indices i, j, k etc. generally run over the three spatial coordinate labels, greek indices $\mu, \nu, \rho, \ldots$ generally run over the four spacetime coordinate labels.

The spacetime metric $g_{\mu\nu}$ is diagonal with elements

$$g_{00} = 1, \quad g_{11} = g_{22} = g_{33} = -1. \tag{A.3}$$

The Dirac matrices γ^μ are defined so that

$$\gamma^\mu \gamma^\nu + \gamma^\nu \gamma^\mu = 2g^{\mu\nu}. \tag{A.4}$$

Moreover we define

$$\begin{aligned} \gamma_5 &= i\gamma^0\gamma^1\gamma^2\gamma^3, \\ \sigma^{\mu\nu} &= \frac{i}{2}(\gamma^\mu\gamma^\nu - \gamma^\nu\gamma^\mu). \end{aligned} \tag{A.5}$$

By letters in boldface we denote spatial three-vectors, e.g. $\mathbf{x}, \mathbf{p}$. A subscript T denotes that we are dealing with two-dimensional transverse vectors

$$\mathbf{x} = \begin{pmatrix} \mathbf{x}_T \\ x^3 \end{pmatrix}, \qquad \mathbf{x}_T = \begin{pmatrix} x^1 \\ x^2 \end{pmatrix}. \tag{A.6}$$

Light-cone variables are defined by

$$x_{\pm} = x^0 \pm x^3. \tag{A.7}$$

The measure of integration then is given by

$$\mathrm{d}^4x = \mathrm{d}x^0\mathrm{d}x^1\mathrm{d}x^2\mathrm{d}x^3 = \frac{1}{2}\mathrm{d}x_+\mathrm{d}x_-\mathrm{d}^2x_T. \tag{A.8}$$

Appendix B

Connectors

We define a connector $V(y, x; C_x)$ between the points x and y along the curve C_x as the non-abelian generalisation of the Schwinger string of QED

$$V(y, x; C_x) := \mathrm{P}\left\{\exp(-ig\int_{C_x} \mathrm{d}z^\mu G_\mu(z))\right\}. \tag{B.1}$$

Here P denotes path ordering. This connector has the following properties:

- The connector of the sum of two adjoined curves C_1 and C_2 is equal to the product of the connectors of the single curves:

$$V(z, x; C_1 + C_2) = V(z, y; C_2) \cdot V(y, x; C_1). \tag{B.2}$$

- If C_x is the curve connecting x and y and $\bar{C}_x$ is the same curve but with reversed orientation, i.e. running from y to x, then

$$V(y, x; C_x) \cdot V(x, y; \bar{C}_x) = \mathbb{1}. \tag{B.3}$$

- Hermitian conjugation corresponds to path reversal:

$$V^\dagger(y, x; C_x) = V(x, y; \bar{C}_x) \tag{B.4}$$

By applying connectors we can shift various quantities between two points in space-time in a gauge covariant way. E.g. we define the shifted gluon field strength tensor $\hat{G}$ which has been transported from x to y along the curve C_x by

$$\hat{G}_{\mu\nu}(y) := V(y, x; C_x) G_{\mu\nu}(x) V^{-1}(y, x; C_x). \tag{B.5}$$

Comparing to (2.25) we recognise that the connectors are in fact the eikonal phases which we have introduced in the discussion of quark-quark scattering in chapter 2.

Appendix C

Calculation of form factors in the model

Starting point for the form factor calculation is the matrix element of the third component of the isospin current at $x = 0$

$$J_3^\mu \equiv \langle h_3(P')|j_3^\mu(0)|h_1(P)\rangle \tag{C.1}$$

with

$$j_3^\mu(x) = \sum_\psi \bar{\psi}(x)\gamma^\mu \left(\frac{1}{2}\tau^3\right)\psi(x). \tag{C.2}$$

Here $\sum_\psi$ denotes the sum over quark fields u, d and τ^3 is the third Pauli isospin matrix. The hadrons h_1, h_3 are supposed to move in positive x^3-direction with $P_+ = P'_+ \to \infty$ (see (5.2)). In analogy to the description of hadron-hadron scattering we therefore denote the incoming hadron by h_1 and the outgoing hadron by h_3. The steps required to compute the form factor from this expression are completely analogous to those discussed in chapter 2 that lead to the $\mathcal{T}$-matrix element (2.49), with the difference that now there are additional contractions between the quarks and diquarks (or antiquarks in the case of mesons) of the hadrons h_1, h_3 and the quark fields of the current j_3^μ when applying the LSZ reduction formalism. By considering the isospin current we ensure that contributions which contain subdiagrams arising from contractions between the quark fields of the current drop out because they are proportional to $\operatorname{tr}\tau^3 = 0$. Now we describe the form factor calculation for the π^+ meson, modelled as $u\bar{d}$ wave packet.

Using our notation from chapter 2 we obtain J_3^μ (C.1) by first calculating the matrix element of j_3^μ between $q\bar{q}$ states and then folding with the wave functions of the wave packets.

$$\begin{aligned} J_3^\mu \;=\; & \int \mathrm{d}^2\Delta_{3T} \int_0^1 \mathrm{d}z_3 \, \frac{1}{(2\pi)^{3/2}} \frac{1}{\sqrt{2}} \, \delta_{s_3,-s_3'} \tilde{\varphi}_3^*(z_3, \boldsymbol{\Delta}_{3T}) \frac{1}{\sqrt{3}} \, \delta_{A_3 A_3'} \\ & \int \mathrm{d}^2\Delta_{1T} \int_0^1 \mathrm{d}z_1 \, \frac{1}{(2\pi)^{3/2}} \frac{1}{\sqrt{2}} \, \delta_{s_1,-s_1'} \tilde{\varphi}_1(z_1, \boldsymbol{\Delta}_{1T}) \frac{1}{\sqrt{3}} \, \delta_{A_1 A_1'} \langle u\bar{d}|j_3^\mu|u\bar{d}\rangle, \end{aligned} \tag{C.3}$$

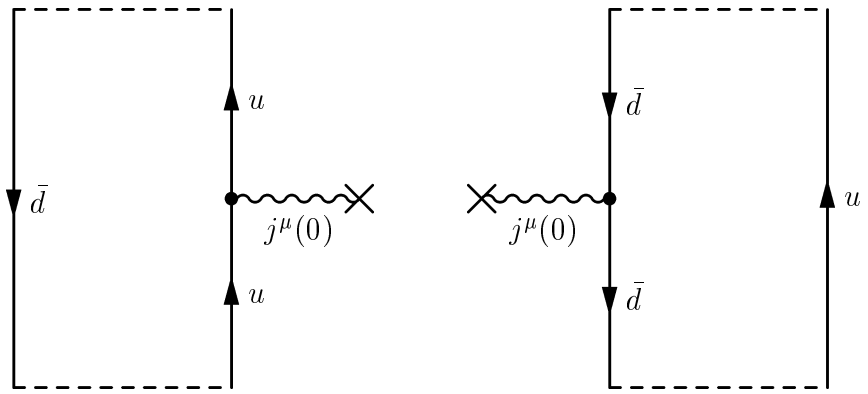

Figure C.1: The two contributions to the matrix element $\langle u\bar{d}|j_3^\mu|u\bar{d}\rangle$. The dashed lines indicate that the loops have been closed by the wave functions.

with

$$\langle u\bar{d}|j_3^\mu|u\bar{d}\rangle \equiv \langle u(p_3,s_3,A_3)\bar{d}(p_3',s_3',A_3')|j_3^\mu(0)|u(p_1,s_1,A_1)\bar{d}(p_1',s_1',A_1')\rangle, \qquad \text{(C.4)}$$

where s_i, A_i are spin and colour indices, respectively and $\tilde{\varphi}_{1,3}$ are the Fourier transforms of the wave functions (3.18)

$$\tilde{\varphi}_i(z,\boldsymbol{\Delta}_T) = \frac{1}{2\pi}\int \mathrm{d}^2x_T\, e^{-i\boldsymbol{\Delta}_T\cdot\mathbf{x}_T}\varphi_i(z,\mathbf{x}_T). \qquad \text{(C.5)}$$

Applying the LSZ reduction formalism we can express the matrix element $\langle u\bar{d}|j_3^\mu|u\bar{d}\rangle$ from (C.4) as an integral over the quark 6-point-function. We get only two terms depicted graphically in Fig. C.1 which are to be interpreted as follows. We consider a fixed gluon background. The quark and antiquark travel in this background and the current either hooks onto the quark line (Fig. C.1a) or the antiquark line (Fig. C.1b). As in chapter 2 the matrix element (C.4) is obtained by averaging over all gluon potentials with the measure given by the functional integral (2.16). In the high energy limit for u and $\bar{d}$ the scattering amplitudes in the fixed gluon background reduce to Wegner-Wilson line operators which are closed to a loop $\mathcal{W}_+$ by the meson wave functions. This is indicated by the dashed lines in Fig. C.1. Combining everything we obtain

$$\begin{aligned}\langle\pi^+(P')|j_3^\mu(0)|\pi^+(P)\rangle \;=\; & \frac{P_{1+}n_+^\mu}{2}\int_0^1 \mathrm{d}z\int \mathrm{d}^2x_T\,\varphi_3^*(z,\mathbf{x}_T)\varphi_1(z,\mathbf{x}_T)\\ & \left(e^{i(1-z)\mathbf{q}_T\cdot\mathbf{x}_T}+e^{-iz\mathbf{q}_T\cdot\mathbf{x}_T}\right)\left\langle\mathcal{W}_+(\frac{1}{2}\mathbf{x}_T,\mathbf{x}_T)\right\rangle_G . \qquad \text{(C.6)}\end{aligned}$$

A straightforward calculation in the MSV shows that the expectation value of the correlation function of one Wegner-Wilson loop is equal to 1. By a shift in the integration variable the d^2x_T integration can be reduced to a Gaussian integral over the wave functions and we find the final result for the matrix element (C.1)

$$\langle\pi^+(P')|j_3^\mu(0)|\pi^+(P)\rangle = \frac{P_{1+}n_+^\mu}{I_\pi}\int_0^1 \mathrm{d}z\, 2z(1-z)\, e^{-(z-\frac{1}{2})^2/2z_h^2}\, e^{-\frac{z^2}{2}S_h^2\mathbf{q}_T^2}. \qquad \text{(C.7)}$$

Let us turn to the proton form factors now. In our simple ansatz the proton consists of a quark and a scalar diquark, which should be favoured above the vector diquark due to dynamical reasons [48]. The spin of the proton then is carried by the quark. This together with the spin conservation on the parton level draws conclusion that, in our model, we get for the matrix element of j_3^μ between proton states an expression similar to (C.7):

$$\langle p(P',s')|j_3^\mu(0)|p(P,s)\rangle = P_+ n_+^\mu \chi_{s'}^\dagger F_{1v}(Q^2)\chi_s \qquad \text{(C.8)}$$

with $F_{1v}(Q^2)$ given in (5.6). Thus we get only a spin-non-flip and no spin-flip contribution in the matrix element (5.3), that is, our model gives $F_{2v}(Q^2)=0$. This is certainly not a very good approximation. But on the other hand the spin-flip part in (5.3) is suppressed by $|\mathbf{q}_T|/(2M_p)$ for $\mathbf{q}_T \to 0$. Thus the matrix element (5.3) is still reasonably described by the model for small enough $|\mathbf{q}_T|$.

Here some remarks on the electromagnetic $p-N(1535)$ transition form factor are due. The transition current can be written in terms of the analogues F_{1*}, F_{2*} of the Pauli and Dirac form factor, respectively, (see [90, 91])

$$\begin{aligned}&\langle N(1535)(P',s')|j^\mu(0)|p(P,s)\rangle \\ &\quad = e\,\bar{u}_{s'}(P')\left[\gamma_5\left(\gamma^\mu\frac{-Q^2}{M_*+M_P}+q^\mu\right)F_{1*}(Q^2)+i\gamma_5\sigma^{\mu\nu}q_\nu F_{2p}(Q^2)\right]u_s(P), \qquad \text{(C.9)}\end{aligned}$$

where M_* is the mass of the $N(1535)$. A similar calculation to the one presented here for the form factors of the proton shows that again F_{1*} multiplies the spin-non-flip part and F_{2*} the spin-flip part. Since we cannot obtain the spin-flip contribution in our model as shown above, we find $F_{2*}(Q^2)=0$. We have argued that it is not decisive for the description of the electromagnetic form factors of the proton at small momentum transfers that the spin-flip contribution in our model is identical to zero. However, this is different for the electromagnetic $p-N(1535)$ transition form factor. The quantities that are measured experimentally are the helicity amplitudes $A^p_{1/2}$ and $S^p_{1/2}$. Each of these amplitudes are described by linear combinations of F_{1*} and F_{2*} and in this context F_{2*} is not suppressed compared to F_{1*}. On the contrary, for $A^p_{1/2}$, which is due to transverse photons with helicity $\lambda=+1$, F_{1*} is suppressed by $|\mathbf{q}_T|^2/(M_*+M_P)$ for $\mathbf{q}_T\to 0$ (see [91]). Therefore, we cannot calculate in a sensible way a quantity which we could compare to experimental data. We only note that

the experimentally observed slow decrease of $A^p_{1/2}$ with Q^2 (see [92] and references therein) is in qualitative agreement to our calculation of the differential cross for $pp \to N(1535)N(1535)$, where we also find a relatively flat distribution in $|t|$.

To summarise, we have outlined in this appendix a calculation of isovector form factors using the same methods as for the scattering processes. The results are in essence as in [69] taking our simple ansatz for the wave functions of the hadrons into account.

Bibliography

[1] C.N. Yang, R. Mills, Phys. Rev. **96** (1954), 191

[2] H.D. Politzer, Phys. Rev. Lett. **30** (1973), 1346
D.J. Gross, F. Wilczek, Phys. Rev. Lett. **30** (1973), 1343

[3] V.N. Gribov, L. Lipatov, Sov. J. Nucl. Phys. **15** (1972), 438
G. Altarelli, G. Parisi, Nucl. Phys. **B126** (1977), 298
Y.L. Dokshitzer, Sov. Phys. JETP **46** (1977), 641

[4] K. Wilson, Phys. Rev. **D10** (1974), 2445

[5] H.J. Rothe, "Lattice Gauge Theories, an Introduction", World Scientific, Singapore (1992)

[6] T.T. Wu, C.N. Yang, Phys. Rev. **B137** (1965), 708
T.T. Chou, C.N. Yang, Phys. Rev. **B170** (1968), 1591
T.T. Chou, C.N. Yang, Phys. Rev. **D19** (1979), 3268
T.T. Chou, C.N. Yang, Phys. Lett. **B128** (1983), 457
T.T. Chou, C.N. Yang, Phys. Lett. **B244** (1990), 113
J. Dias de Deus, P. Kroll, Phys. Lett. **B60** (1976), 375
J. Dias de Deus, P. Kroll, Nuovo Cimento **A37** (1977), 67
P. Kroll, Z. Phys **C15** (1982), 67
J. Hüfner, B. Povh, Phys. Rev. **D46** (1992), 990
J. Hüfner, B. Povh, E. Wälde, Z. Phys **C63** (1994), 631

[7] R.C. Hwa, Phys. Rev. **D22** (1980), 759, 1593
R.C. Hwa, M. Sajjad Zahir, Phys. Rev. **D23** (1981), 2539
R.C. Hwa, *Central production and small angle elastic scattering in the valon model*, in: "Proc. 12th Int. Symp. Multiparticle Dynamics, Notre Dame, Ind. 1981", W.D. Shephard, V.P. Kennedy (eds.), World Scientific, Singapore (1982)

[8] G. 't Hooft, Nucl. Phys. **B72** (1974), 461
G. Veneziano, Nucl. Phys. **B74** (1974), 365
G. Veneziano, Phys. Lett. **B52** (1974), 220
G. Veneziano, Nucl. Phys. **B117** (1976), 519
M. Ciafaloni, G. Marchesini, G. Veneziano, Nucl. Phys. **B98** (1975), 472, 493

A. Capella, U. Sukhatme, Chung-I Tan, J. Tran Thanh Van, Phys. Lett. **B81** (1979), 68
A. Capella, U. Sukhatme, J. Tran Thanh Van, Z. Phys. **C3** (1980), 329
B. Andersson, G. Gustafson, G. Ingelman, T. Sjöstrand, Phys. Rep. **C97** (1983), 31
X. Artru, Phys. Rep. **C97** (1983), 147
B. Andersson, G. Gustafson, B. Nilsson-Almqvist, Nucl. Phys. **B281** (1987), 289
K. Werner, Phys. Rep. **C232** (1993), 87

[9] V.S. Fadin, E.A. Kuraev, L.N. Lipatov, Phys. Lett. **B60** (1975), 50
E.A. Kuraev, L.N. Lipatov, V.S. Fadin, Sov. Phys. JETP **44** (1976), 443
E.A. Kuraev, L.N. Lipatov, V.S. Fadin, Sov. Phys. JETP **45** (1977), 199
L.N. Lipatov, Sov. J. Nucl. Phys. **23** (1976), 338
Ya. Ya. Balitskii, L.N. Lipatov, Sov. J. Nucl. Phys. **28** (1978), 822
L.N. Lipatov, Sov. Phys. JETP **63** (1986), 904
L.N. Lipatov, *Pomeron in Quantum Chromodynamics*, in: "Perturbative Quantum Chromodynamcis", A.H. Mueller (ed.), World Scientific, Singapore (1989)
A.R. White, Int. J. Mod. Phys. **A6** (1990), 1859
A.R. White, Nucl. Phys. Proc. Suppl. **12** (1990), 190
A.R. White, Nucl. Phys. **B25** (1992), 167
J. Bartels, Z. Phys. **C60** (1993), 471

[10] H. Cheng, T.T. Wu, "Expanding Protons", MIT Press, Cambridge, Mass. (1987)

[11] K. Hagiwara *et al.* [Particle Data Group], Phys. Rev. **D66** (2002), 010001

[12] A. Donnachie, P.V. Landshoff, Phys. Lett. **B296** (1992), 227

[13] P.D.B. Collins, "An Introduction to Regge Theory", Cambridge University Press (1977)

[14] E.M. Levin, L.L. Frankfurt, JETP Lett. **2** (1965), 65
H.J. Lipkin, F. Scheck, Phys. Rev. Lett. **16** (1966), 71
H.J. Lipkin, Phys. Rev. Lett. **16** (1966), 1015
J.J.J. Kokkedee, L. Van Hove, Nuovo Cim. **42** (1966), 711

[15] A. Donnachie, P.V. Landshoff, Nucl. Phys. **B244** (1984), 322

[16] H.G. Dosch, Prog. Part. Nucl. Phys. **33** (1994), 121

[17] J.R. Forshaw, D.A. Ross, "Quantum chromodynamics and the pomeron", Cambridge University Press (1997)

[18] A. Hebecker, Phys. Rept. **331** (2000), 1

[19] K. Goulianos, Nucl. Phys. Proc. Suppl. **12** (1990), 110

[20] P.V. Landshoff, O. Nachtmann, Z. Phys. **C35** (1987), 405

[21] M.A. Shifman, A.I. Vainshtein, V.I. Zakharov, Nucl. Phys. **B147** (1979), 385, 448, 519

[22] O. Nachtmann, Ann. Phys. **209** (1991), 436

[23] A. Krämer, H.G. Dosch, Phys. Lett. **B252** (1990), 669
A. Krämer, H.G. Dosch, Phys. Lett. **B272** (1991), 114
H.G. Dosch, E. Ferreira, A. Krämer, Phys. Lett. **B289** (1992), 153

[24] H.G. Dosch, E. Ferreira, A. Krämer, Phys. Rev. **D50** (1994), 1992

[25] H.G. Dosch, Phys. Lett. **B190** (1987), 177
H.G. Dosch, Yu.A. Simonov, Phys. Lett. **B205** (1988), 339
Yu.A. Simonov, Nucl. Phys. **B307** (1988), 512

[26] H.G. Dosch, *Nonperturbative Methods in QCD*, in: "Hadron Physics 96", E. Ferreira *et al.* (ed.), Singapore (1997), 169

[27] H.G. Dosch, T. Gousset, G. Kulzinger, H.J. Pirner, Phys. Rev. **D55** (1997), 2602

[28] H.G. Dosch, T. Gousset, H.J. Pirner, Phys. Rev. **D57** (1998), 1666

[29] G. Kulzinger, H.G. Dosch, H.J. Pirner, Eur. Phys. J. **C7** (1999), 73

[30] E.R. Berger, O. Nachtmann, Eur. Phys. J. **C7** (1999), 459

[31] E.R. Berger, A. Donnachie, H.G. Dosch, W. Kilian, O. Nachtmann, M. Rüter, Eur. Phys. J. **C9** (1999), 491

[32] E.R. Berger, A. Donnachie, H.G. Dosch, O. Nachtmann, Eur. Phys. J. **C14** (2000), 673

[33] O. Nachtmann, *High Energy Collisions and Nonperturbative QCD*, in: "Perturbative and Nonperturbative Aspects of Quantum Field Theory", H. Latal, W. Schweiger (eds.), Springer Verlag, Berlin/Heidelberg (1997), 49

[34] H.G. Dosch, E. Ferreira, Phys. Lett. **B318** (1993), 197
E. Ferreira, F. Pereira, Phys. Rev. **D55** (1997), 130
E. Ferreira, F. Pereira, Phys. Rev. **D56** (1997), 179
M. Rüter, H.G. Dosch, Phys. Rev. **D57** (1998), 4097

[35] M. Rüter, H.G. Dosch, Phys. Lett. **B380** (1996), 177

[36] M. Rüter, H.G. Dosch, O. Nachtmann, Phys. Rev. **D59** (1999), 014018

[37] M. Wirbel, B. Stech, M. Bauer, Z. Phys. **C29** (1985), 637

[38] H.G. Dosch, O. Nachtmann, T. Paulus, S. Weinstock, Eur. Phys. J. **C21** (2001), 339

[39] V.V. Anisovich, D.I. Melikhov, V.A. Nikonov, Phys. Rev. **D52** (1995), 5295
V.V. Anisovich, D.I. Melikhov, V.A. Nikonov, Phys. Rev. **D55** (1997), 2918

[40] F. Cardarelli, E. Pace, G. Salme, S. Simula, Phys. Lett. **B357** (1995), 267
D. Melikhov, Phys. Rev. **D53** (1996), 2460

[41] J.J. Sakurai, Ann. Phys. **11** (1960), 1
M. Gell-Mann, F. Zakhariasen, Phys. Rev. **124** (1961), 953

[42] J. Gasser, H. Leutwyler, Nucl. Phys. **B250** (1985), 465

[43] G.J. Gounaris, J.J. Sakurai, Phys. Rev. Lett. **21** (1968), 244

[44] D.I. Melikhov, O. Nachtmann, T. Paulus, arXiv:hep-ph/0209151

[45] G.K. Savvidy, Phys. Lett. **B71** (1977), 133

[46] A. DiGiacomo, H. Panagopoulos, Phys. Lett. **B285** (1992), 133
A. DiGiacomo, E. Meggiolaro, H. Panagopoulos, Nucl. Phys. **B483** (1997), 371

[47] E. Meggiolaro, Phys. Lett. **B451** (1999), 414

[48] T. Schäfer, E.V. Shuryak, J.J.M. Verbaarschot, Nucl. Phys. **B412** (1994), 143

[49] C. Cohen-Tannoudji, B. Diu, F. Laloë, "Quantum Mechanics", Wiley (1977)

[50] S.J. Brodsky, J. Rathsman, C. Merino, Phys. Lett. **B461** (1999) 114

[51] M. Rüter, Ph.D. thesis, University of Heidelberg (1997)

[52] E.R. Berger, Ph.D. thesis, University of Heidelberg (1999)

[53] A.I. Shoshi, F.D. Steffen, H.J. Pirner, Nucl. Phys. **A709** (2002), 131

[54] J.R. Forshaw, G. Kerley, G. Shaw, Phys. Rev. **D60** (1999), 074012

[55] A. Donnachie, H.G. Dosch, Phys. Rev. **D65** (2002), 014019

[56] G.P. Lepage, Jour. Comp. Phys. **27** (1978), 192

[57] S. Weinstock, *private communication*

[58] E. Nagy *et al.*, Nucl. Phys. **B150** (1979), 221
U. Amaldi, K.R. Schubert, Nucl. Phys. **B166** (1980), 301

[59] M.G. Albrow *et al.* [CHLM Collaboration], Nucl. Phys. **B108** (1976), 1

[60] J.C.M. Armitage *et al.*, Nucl. Phys. **B194** (1982), 365

[61] M. Bozzo *et al.* [UA4 Collaboration], Phys. Lett. **B136** (1984), 217
D. Bernard *et al.* [UA4 Collaboration], Phys. Lett. **B186** (1987), 227

[62] F. Abe *et al.* [CDF Collaboration], Phys. Rev. **D50** (1994), 5535

[63] N.A. Amos *et al.* [E710 Collaboration], Phys. Lett. **B301** (1993), 313

[64] A. Donnachie, *private communication*

[65] V.N. Gribov, Sov. J. Nucl. Phys. **5** (1967), 138
D.R.O. Morrison, Phys. Rev. **165** (1968), 1699

[66] M. Adamus *et al.*, Phys. Lett. **B186** (1987), 223

[67] C.W. Akerlof *et al.*, Phys. Rev. **D14** (1976), 2864
R. Rubinstein *et al.*, Phys. Rev. **D30** (1984), 1413

[68] M. Adamus *et al.*, Z. Phys. **C39** (1988), 301

[69] S.D. Drell, T.-M. Yan, Phys. Rev. Lett. **24** (1970), 181

[70] F. Borkowski *et al.*, Nucl. Phys. **A222** (1974), 269
F. Borkowski *et al.*, Nucl. Phys. **B93** (1975), 461

[71] P.E. Bosted *et al.*, Phys. Rev. Lett. **68** (1992), 3841
R.C. Walker *et al.*, Phys. Rev. **D49** (1994), 5671

[72] C. Herberg *et al.*, Eur. Phys. J. **A5** (1999), 131

[73] H. Leeb, C. Teichtmeister, Phys. Rev. **C48** (1993), 1719

[74] Th. Udem *et al.*, Phys Rev. Lett. **79** (1997), 2646

[75] O. Nachtmann, *The QCD vacuum structure and its manifestations*, in: "Confinement physics", S.D. Bass, P.A.M. Guichon (eds.), Editions Frontières (1996), 27

[76] C. Bebek *et al.*, Phys. Rev. **D17** (1978), 1693
S.R. Amendolia *et al.* [NA7 Collaboration], Nucl. Phys. **B277** (1986), 168

[77] A.V. Efremov, A.V. Radyushkin, JETP Lett., **25** (1977), 210
S. Brodsky, G.P. Lepage, Phys. Lett. **B87** (1979), 359

[78] J. Lefrancois, *Results of the Orsay storage ring A.C.O.*, in: "Proceedings of the 1971 Internatinal Symposium on electron and photon interactions at high energies", Cornell University, Ithaca, New York (1971)

[79] M. Benayoun, H.B. O'Connell, and A.G. Williams, Phys. Rev. **D59** (2001), 074020

[80] A. Pich, J. Portoles, Phys. Rev. **D63** (2001), 093005
J.J. Sanz-Cillero, A. Pich, arXiv:hep-ph/0208199

[81] G. Ecker, J. Gasser, A. Pich, E. de Rafael, Nucl. Phys. **B321** (1989), 311

[82] N.M. Kroll, T.D. Lee, B. Zumino, Phys. Rev. **157** (1967), 1376

[83] M. Gourdin, in: "Hadronic interactions of electrons and photons", J. Cumming, H. Osborn, (eds.), Academic Press, London (1971)

[84] A. Donnachie, H. Mirzaie, Z. Phys. **C33** (1987), 407
G. Kulzinger, H.G. Dosch, H.J. Pirner, Eur. Phys. J. **C7** (1999), 73

[85] R. Barate *et al.* [ALEPH Collaboration], Z. Phys. **C76** (1997), 15

[86] S.D. Protopopescu *et al.*, Phys. Rev. **D7** (1973), 1279
P. Estabrooks, A.D. Martin, Nucl. Phys. **B79** (1974), 301

[87] R.R. Akhmetshin *et al.* [CMD-2 Collaboration], arXiv:hep-ex/9904027

[88] CERN Program Library, **D510**, FUMILI

[89] S. Anderson *et al.* [CLEO Collaboration], Phys. Rev. **D61** (2000), 112002

[90] R.C.E. Devenish, T.S. Eisenschitz, J.G. Körner, Phys. Rev. **D14** (1976), 3063

[91] W. Konen, H.J. Weber, Phys. Rev. **D41** (1990), 2201

[92] R. Thompson *et al.* [CLAS Collaboration], Phys. Rev. Lett. **86** (2001), 1702

Danksagung

Sehr herzlich danke ich Herrn Prof. O. Nachtmann für die engagierte Betreuung dieser Arbeit und die freundliche Unterstützung.

Herrn Prof. K. Meier möchte ich für die Übernahme des Zweit-Gutachtens danken.

Des weiteren danke ich Herrn Prof. H.G. Dosch für die freundliche Zusammenarbeit und die Zweit-Betreuung der Arbeit.

Ebenfalls zu Dank verpflichtet bin ich A. Donnachie, D.I. Melikhov und S. Weinstock für die kollegiale Zusammenarbeit.

Dank gebührt fernerhin T. Baier, E. Berger, E. Bick, C. Ewerz, T. Gasenzer, A. Hebecker, G. Kulzinger, A. Rauscher, M. Rüter, V. Schatz, C. Schwanenberger und F. Steffen für zahlreiche Diskussionen sowie den vielen hier nicht namentlich aufgeführten Institutsmitgliedern, die ebenfalls zur guten Arbeitsatmosphäre beigetragen haben.

Besonders danken möchte ich meinen Eltern, die mir mein Studium ermöglichten und Christiane für ihre Zuwendung.

Schließlich danke ich dem Graduiertenkolleg "Physikalische Systeme mit vielen Freiheitsgraden" für die finanzielle Unterstützung.